

# **Theory of Electron Transport in Molecular Structures**

Maryam Alshahrani

PhD. Thesis in Nanoelectronics

Department of physics, Lancaster University, UK



This thesis is submitted in partial fulfilment of the requirements

for the degree of Doctor of Philosophy

2022

## **Declaration**

Except where stated otherwise, this thesis results from the author's original work. It has not been submitted in substantially the same form for the award of a higher degree elsewhere. Other sources of information have been used; they have been acknowledged. These thesis documents work carried out between October 2019 and July 2022 at Lancaster University, UK, under the supervision of Prof. Colin J. Lambert and Dr. Ali K. Ismael and funded by the Ministry of Higher Education Saudi Arabia and University of Bisha, KSA.

*Maryam Alshahrani*

*May 2022*

## **Acknowledgement**

I would like to express my gratitude to Prof. Colin John Lambert for the excellent supervision and direction. Without his guidance and support, my thesis would never have been done.

I would also like to thank my supporter, the Ministry of Education in Saudi Arabia, and the University of Bisha for this excellent opportunity to study PhD in the United Kingdom.

I would like to thank the co-supervisors, Dr Michael, Dr Iain, and all my friends and colleagues in Colin's group, for their help in improving my skills during my studying.

Finally, I would also like to offer my sincere thanks and gratitude to my father, my mother, my brothers and sisters, and my little family: my husband Mohammed, my daughter Kadi and my son Salman for their support and understanding during my pursuit of a PhD degree that made the completion of thesis possible.

*Maryam*

## Abstract

In developing future nano-scale applications in the molecular electronics field, studies of electron transport through single molecules are of fundamental interest. Since single or multiple molecules are considered essential building blocks to design and construct these molecular electronics devices, understanding their electronic and transport properties is required. Enormous theoretical and experimental studies were carried out to make the molecular junctions and explore their electrical performance. Within this framework, this thesis addresses some of the fundamental aspects of transport theory, involving the theoretical and mathematical approaches to investigate the electron transport via junctions, including a scattering region formed from a single molecule connected to metal electrodes. The methods used in this research are based on a combination of density functional theory and its realisation within the SIESTA code, and non-equilibrium Green's function embodied in the GOLLUM code to study electrical conductance on a molecular scale. In this thesis, I focus on various N-Heterocyclic carbenes (NHC) complexes of double NHC-anchored single-molecule junctions and investigate the mechanism of charge transport through their molecular junctions. I also study their electronic structure properties, such as the wave function plot and their binding energetics to electrodes. Experimental measurements and my DFT simulations revealed a high electrical conductance of monomer and dimer NHC molecular junctions. Consequently, my simulations provide a novel strategy for designing high conductance molecular devices using NHCs and are a step along with the roadmap toward future integration of molecular electronic devices.

## List of Publications

Zhixin Chen, Marvam Alshahrani, Yaorong Chen, Lina Chen, James O. Thomas, Zhiyu Zhu, Haiping, Xia, Colin Lambert and Wenjing. Hong Highly Conductive Single-molecule Junctions with Double N-Heterocyclic Carbene Anchors. *Submitted*.

## Contents

Chapter 1 .....	19
Molecular Electronics .....	19
1.1 Introduction .....	19
1.2 Thesis Outline.....	23
1.3 Bibliography .....	24
Chapter 2.....	27
Density Functional Theory .....	27
2.1 Introduction .....	27
2.2 Many-body problem .....	29
2.3 Born-Oppenheimer approximation.....	30
2.4 Density Functional theory .....	31
2.4.1 The Hohenberg-Kohen theorems .....	31
2.4.2 Kohn-Sham equation.....	34
2.4.3 Exchange-correlation functional .....	37
2.5 SIESTA implementation of DFT.....	37
2.5.1 Pseudopotential approximation .....	38
2.5.2 Basis Sets.....	38
2.5.3 Calculating binding energy using the counterpoise method.....	40
2.6 Conclusion.....	41

2.7	Bibliography .....	42
	Chapter 3.....	45
	Theory of single-particle transport.....	45
3.1	Introduction .....	45
3.2	Tight-Binding Model.....	47
3.3	The two-level system.....	48
3.4	Infinite chain in one dimension .....	50
3.5	Periodic chain in one dimension.....	52
3.6	Bond current .....	55
3.7	Scattering theory of transport in one-dimension .....	59
3.8	A single impurity in one dimension. ....	59
3.9	Scattering matrix .....	61
3.9	Landauer Formula .....	64
3.10	Transmission coefficient of an arbitrary scatterer .....	68
3.11	Generic features of the Transmission curve.....	72
3.11.1	Breit–Wigner formula (BWF).....	73
3.11.2	Anti-resonance .....	74
3.12	Green’s Functions.....	76
3.12.1	Green’s function of a doubly infinite linear chain .....	77
3.13	Conclusion.....	80

3.14 Bibliography .....	81
Chapter 4 .....	83
Electronic structure investigation of Double N-Heterocyclic Carbene Anchors .....	83
4.1 Motivation .....	84
4.2 Introduction .....	85
4.3 Studied Molecules .....	86
4.4 Frontier orbitals of the molecules .....	89
1. R-biNHC .....	90
2. biNHC .....	91
3. N2F .....	92
4. o-S2F .....	93
5. p-S2F .....	94
6. 2Ag-2biNHC .....	95
7. 2Au-2biNHC .....	96
4.5 Binding energy on a gold substrate .....	97
4.5.1 3-D binding energy simulations .....	98
4.5.2 1-D binding energy simulations .....	103
4.6 Conclusion .....	107
4.7 Bibliography .....	108
Chapter 5 .....	111

## Highly Conductive Single-molecule Junctions with Double N-Heterocyclic Carbene

Anchors.....	111
5.1 Introduction .....	111
5.2 Transmission coefficient $T(E)$ .....	112
5.2.1 Transport calculations of monomers .....	113
5.2.2 Transport according to the three scenarios .....	115
Scenario A:.....	115
Scenario B:.....	118
Scenario C:.....	121
5.2.3 Spin polarisation.....	123
5.2.4 Transport calculations of dimer molecules.....	125
5.2.5 Spin-dependent transport calculations of dimer molecules.....	126
5.2.6 Fluctuations of OTf <sup>-</sup> counterion .....	128
5.2.7 Comparison of transmission functions of monomers and dimers .....	131
5.3 Broadened molecular orbital of monomers and dimers .....	133
5.3.1 Broadened molecular orbital of monomers .....	136
5.3.2 Broadened molecular orbital of dimers .....	137
5.4 Theory versus experiment .....	139
5.5 Conclusion.....	141
5.6 Bibliography .....	143

Chapter 6.....	146
Conclusion and Future Work.....	146
6.1 Conclusion.....	146
6.2 Future work.....	148
6.3 Bibliography.....	149

## List of Figures

<b>Figure 2.1.</b> A Schematic illustration of the DFT self-consistent cycle .....	36
<b>Figure 3.1.</b> A representation of a two-level system. ....	49
<b>Figure 3.2.</b> Tight-binding representation of one-dimensional infinite chain with on-site energies $\varepsilon_0$ and couplings $-\gamma$ . ....	50
<b>Figure 3.3.</b> The dispersion relation of a linear chain. ....	52
<b>Figure 3.4.</b> Tight-binding representation of one-dimensional chain with periodic boundary conditions of on-site energies $\varepsilon_0$ and couplings $-\gamma$ . ....	52
<b>Figure 3.5.</b> Wavefunctions of the periodic chain of six sites are obtained numerically, with their energies. ....	55
<b>Figure 3.6.</b> Tight-binding representation of one-dimensional chain in which all site energies $\varepsilon_j$ and all bonds $-\gamma_j$ are arbitrary. ....	56
<b>Figure 3.7.</b> Tight-binding representation of a doubly infinite chain containing a single impurity at site $j = 0$ . ....	59
<b>Figure 3.8.</b> A scattering region (molecule) placed between two leads connecting two reservoirs with different chemical potentials $\mu_L$ and $\mu_R$ . When an incident wave strikes $I$ with the scatterer from the left, the wave will be transmitted to the right with probability $T = t^2$ and then reflected with probability $R = r^2$ . Therefore, the incident electrons essential be either reflected or transmitted for the probability conservation is $T + R = 1$ as Eq. 3.45. ....	64
<b>Figure 3.9.</b> Tight-binding model of one-dimensional double-infinite chain with an arbitrary scattering region. ....	68

**Figure 3.10.** The transmission coefficients  $T(E)$  of three levels system demonstrate a Breit–Wigner resonance: where the level broadening due to  $\Gamma_L + \Gamma_R$  and the shift in the resonances due to  $(\sigma)$ . When  $E = E_n - \Gamma_L + \Gamma_R$ ,  $T(E) = \frac{T_{max}}{2}$ . Therefore, the half-width of resonance is  $\Gamma_L + \Gamma_R$ . For symmetrical system,  $\Gamma_L = \Gamma_R$ ,  $T_{max} = 1$ ..... 74

**Figure 3.11.** The transmission coefficients  $T(E)$  of the ring system demonstrate an anti-resonance: leading to steep slopes, where the appearance of two peaks rather than six peaks corresponding to six atoms are the degeneracies concerning their energy eigenvalues. The position of the anti-resonance is determined by the connectivity sites of the scattering region to the leads. .... 76

**Figure 3.12.** Tight-binding model of one-dimensional infinite chain with on-site energies  $\epsilon_0$  and couplings  $-\gamma$ ..... 77

**Figure 4.1.** Fully relaxed isolated molecules. **Top panel.** Monomer molecules including **R-biNHC**, **biNHC** and **N2F** with pristine pyridyl anchor groups (2Py). **Lower panel.** Monomer molecules including **o-S2F** and **p-S2F** with pristine thioether anchor group (2SMe). Key: C = dark grey, H = white, N = blue, S = light yellow..... 88

**Figure 4.2.** Fully relaxed isolated molecules. Dimer molecules including **2Ag-2biNHC** and **2Au-2biNHC** with bridging atoms such as Ag and Au respectively Key: C = dark grey, H = white, Ag = light grey and Au = dark yellow..... 89

**Figure 4.3.** Wave function plot of **R-biNHC**. **Top panel:** Fully optimised geometry of **R-biNHC**. **Lower panel:** HOMO, LUMO, HOMO-1 and LUMO+1 plots of **R-biNHC** molecule along with their energies (monomer case). .... 90

**Figure 4.4.** Wave function plot of **biNHC**. **Top panel:** Fully optimised geometry of **biNHC**. **Lower panel:** HOMO, LUMO, HOMO-1 and LUMO+1 plots of **biNHC** molecule along with their energies (monomer case). ..... 91

**Figure 4.5.** Wave function plot of **N2F**. **Top panel:** Fully optimised geometry of **N2F**. **Lower panel:** HOMO, LUMO, HOMO-1 and LUMO+1 plots of **N2F** molecule along with their energies (monomer case). ..... 92

**Figure 4.6.** Wave function plot of **o-S2F**. **Top panel:** Fully optimised geometry of **o-S2F**. **Lower panel:** HOMO, LUMO, HOMO-1 and LUMO+1 plots of **o-S2F** molecule along with their energies (monomer case). ..... 93

**Figure 4.7.** Wave function plot of **p-S2F**. **Top panel:** Fully optimised geometry of **p-S2F**. **Lower panel:** HOMO, LUMO, HOMO-1 and LUMO+1 plots of **p-S2F** molecule along with their energies (monomer case). ..... 94

**Figure 4.8.** Wave function plot of **2Ag-2biNHC**. **Top panel:** Fully optimised geometry of **2Ag-2biNHC**. **Lower panel:** HOMO, LUMO, HOMO-1 and LUMO+1 plot of **2Ag-2biNHC** molecule along with their energies (dimer case). ..... 95

**Figure 4.9.** Wave function plot of **2Au-2biNHC**. **Top panel:** Fully optimised geometry of **2Au-2biNHC**. **Lower panel:** HOMO, LUMO, HOMO-1 and LUMO+1 plots of **2Au-2biNHC** molecule along with their energies (dimer case). ..... 96

**Figure 4.10.** Sampling of the Au tip position around the molecular backbone searching for the strongest binding locations, (an example). ..... 98

**Figure 4.11.** **Top panel:** Compound **2** (**biNHC** molecule) configuration at the Au-tip interface for three different positions: Au-C and Au-five-membered ring. **Lower panel:** 3-D binding energy plot as a function of Au-tip at 350 positions. 80 and 90 sites possess the stronger binding energy of Au-

C bond, at approximately 1.6 eV. The 250 site possesses weaker binding energy of Au-five-membered ring bond, at approximately 0.2 eV..... 100

**Figure 4.12. Top panel:** Compound **5** (**p-S2F** molecule) configuration at the Au-tip interface for three different positions: Au-SMe and Au-five-membered ring. **Lower panel:** 3-D binding energy plots as a function of Au-tip at 350 positions. 125 and 225 sites possess stronger binding energy of Au-SMe bond, at approximately 0.3 eV. The 310 site possess weaker binding energy of Au-five-membered ring bond, at approximately 0.2 eV..... 101

**Figure 4.13. Top panel:** Compound **3** (**N2F** molecule) configuration at the Au-tip interface for three different positions: Au-N and Au-five-membered ring. **Lower panel:** 3-D binding energy plots as a function of Au-tip at 300 positions. The 50 and 190 sites possess stronger binding energy of Au-N bond, at approximately 0.5 eV. The 270 site possesses weaker binding energy of Au-five-membered ring bond, at approximately 0.2 eV..... 102

**Figure 4.14. Right panel:** Molecule configuration at the Au lead interface, compound **2** (**biNHC** molecule), a carbon atom linked to Au electrode. **Left panel:** An example of binding energy plot as a function of distance **d**. This distance is found to 2.3 Å, at approximately 1.6 eV. .... 104

**Figure 4.15. Right panel:** Molecule configuration at the Au lead interface, compound **5** (**p-S2F** molecule), a sulphide (SMe) linked to Au electrode. **Left panel:** An example of binding energy plot as a function of distance **d**. This distance is found to 2.7 Å, at approximately 0.3 eV. .... 104

**Figure 4.16. Right panel:** Molecule configuration at the Au lead interface, compound **3** (**N2F** molecule), a Py linked to Au electrode. **Left panel:** An example of binding energy plot as a function of distance **d**. This distance is found to 2.2 Å, at approximately 0.5 eV. .... 105

**Figure 4.17. Right panel:** Molecule configuration at the Au lead interface, compound **5** (**p-S2F** molecule), a five-membered ring linked to Au electrode. **Left panel:** An example of binding

energy plot as a function of distance  $d$ . This distance is found to 3.6 Å, at approximately 0.2 eV.

..... 105

**Figure 5.1.** Schematic illustrations of the monomer molecules in Au junctions for Scenario A, in which the Au tips connect to the molecules as follows: compounds **1** and **2** (**R-biNHC** and **biNHC**) connect via Au-C bonds, compound **3** (**N2F**) connects via Au-N bonds, compounds **4** and **5** (**o-S2F** and **p-S2F**) connect via Au-SMe bonds..... 116

**Figure 5.2.** Transmission coefficients as a function of energy of the studied molecules in Au junctions for Scenario A. Zero bias transmission coefficients  $T(E)$  of compounds **1**, **2**, **3**, **4** and **5** (**R-biNHC**, **biNHC**, **N2F**, **o-S2F** and **p-S2F**) against electron energy  $E$ . The yellow rectangular box shows that a range of energy within the HOMO–LUMO gap..... 118

**Figure 5.3.** Schematic illustrations of the monomer molecules in Au junctions for Scenario B. It illustrates that the top contact is always to the five-membered ring for all molecules whereas the bottom contact as follows for compounds **1** and **2** (**R-biNHC** and **biNHC**): between the two lower rings pointing towards the two Carbon atoms (Au-C), compound **3** (**N2F**): between the two lower rings pointing towards the two pyridyl atoms (Au-N), compounds **4** and **5** (**o-S2F** and **p-S2F**): between the two lower rings pointing towards the two thioether atoms (Au-SMe). ..... 119

**Figure 5.4.** Transmission coefficients as a function of energy of the studied molecules in Au junctions for Scenario B. Zero bias transmission coefficients  $T(E)$  of as compounds **1**, **2**, **3**, **4** and **5** (**biNHC**, **R-biNHC**, **N2F**, **o-S2F** and **p-S2F**) against electron energy  $E$  in Au metallic junctions. The yellow rectangular box shows that a range of energy within the HOMO–LUMO gap..... 120

**Figure 5.5.** Schematic illustrations of the monomer molecules in Au junctions for Scenario C. It illustrates Au contact points to the anchor groups where is approximately 90 degrees between the

two contact points and as follows for compounds **1** and **2** (**R-biNHC** and **biNHC**): Au-N, compound **3** (**N2F**): Au-C, compounds **4** and **5** (**o-S2F** and **p-S2F**):(Au-C). ..... 121

**Figure 5.6.** Transmission coefficients as a function of energy of the studied molecules in Au junctions for **Scenario C**. Zero bias transmission coefficients  $T(E)$  of compounds **1**, **2**, **3**, **4** and **5** (**R-biNHC**, **biNHC**, **N2F**, **o-S2F** and **p-S2F**) against electron energy  $E$  in Au metallic junctions. The yellow rectangular box shows that a range of energy within the HOMO–LUMO gap. .... 122

**Figure 5.7.** Examples of molecular geometries for the dimer. **Left panel:** an isolated dimer molecule compound **7** (**2Au-2biNHC**). **Right panel:** shows a counterion (i.e., OTf<sup>-</sup>). ..... 125

**Figure 5.8.** Spin-polarised transmission coefficients, spin-up  $T_{up}(E)$ , spin-down  $T_{down}(E)$  and  $\frac{T_{up}(E)+T_{down}(E)}{2}$  for the binding configuration of compound **7** (**2Au-2biNHC**) with the OTf<sup>-</sup> counterion. Three curves represent the spin-up, spin-down and the average of them: blue, red, and orange curves respectively. .... 127

**Figure 5.9.** Spin-polarised transmission coefficients spin-up  $T_{up}(E)$ , spin-down  $T_{down}(E)$  and  $\frac{T_{up}(E)+T_{down}(E)}{2}$ , for the binding configuration of compound **6** (**2Ag-2biNHC**) with the OTf<sup>-</sup> counterion. Three curves represent the spin-up, spin-down and the average of them: blue, red, and orange curves respectively. .... 128

**Figure 5.10.** Sampling the OTf<sup>-</sup> counterion position around the dimer. (For clarity the electrodes are not shown and only 6 positions are shown). ..... 129

**Figure 5.11.** Orange curves show the average spin-polarised transmission coefficient  $T(E)$  as a function of energy for a selection of the 12 possible configurations of OTf<sup>-</sup> counterion bound to compound **7** (**2Au-2biNHC** dimer). ..... 130

**Figure 5.12.** Orange curves show the average spin-polarised transmission coefficient  $T(E)$  as a function of energy for a selection of the 12 possible configurations of OTf<sup>-</sup> counterion bound to compound **6** (**2Ag-2biNHC** dimer). ..... 131

**Figure 5.13.** Transmission coefficients of the studied molecules in Au junctions. Zero bias transmission coefficients  $T(E)$  of compounds **1**, **2**, **3**, **4** and **5** (**biNHC**, **R-biNHC**, **N2F**, **o-S2F** and **p-S2F**) (as monomers), and compounds **6** and **7** (**2Ag-2biNHC** and **2Au-2biNHC**) (as dimers), against electron energy  $E$  in Au metallic junctions (scenario **A**). ..... 132

**Figure 5.14.** Example of broadened molecular orbital  $\Gamma$  value of compound **3** (**N2F**) against electron energy  $E$  in Au metallic junctions with respect to the DFT-predicted Fermi energy ( $E - E_F^{DFT} = 0$  eV). ..... 134

**Figure 5.15.** Broadened molecular orbital  $\Gamma$  values of compounds **1**, **2**, **3**, **4** and **5** (**R-biNHC**, **biNHC**, **N2F**, **o-S2F** and **p-S2F**) against electron energy  $E$  in Au metallic junctions (scenario **A**). ..... 136

**Figure 5.16.** Broadened molecular orbital  $\Gamma$  values of compounds **6** and **7** (**2Ag-2biNHC** and **2Au-2biNHC**) against electron energy  $E$  in Au metallic junctions. ..... 137

**Figure 5.17.** Comparison between experimental and theoretical conductance (red-circles and brown-circles respectively) of the studied molecules: compounds **1**, **2**, **3**, **4** and **5** (**R-biNHC**, **biNHC**, **N2F**, **o-S2F** and **p-S2F**) (as monomers), and compounds **6** and **7** (**2Ag-2biNHC** and **2Au-2biNHC**) (as dimers) obtained at the DFT-predicted Fermi level ( $E - E_F^{DFT} = 0$  eV). Note: (The conductance of compound **5** (**p-S2F**) was undetectable experimentally). ..... 140

**Table 4.1.** Summarises the optimum separation distance  $d$  and the binding energy ( $B.E$ ) of 3-D/1-D scanning simulation of the studied molecules. .... 106

**Table 5.1.** Summarises the three scenarios **A**, **B**, and **C** and the bond nature based on the three strongest binding energies for compounds **1**, **2**, **3**, **4** and **5** (**R-biNHC**, **biNHC**, **N2F**, **o-S2F** and **p-S2F**) and describe their symmetric/ asymmetric structures..... 114

**Table 5.2.** Summarises the theoretical results for broadened molecular orbital values of coupling strength  $\Gamma$  due to the electrodes and level position  $E_n$  for the monomer (scenario **A**) and dimer junctions that shown in Figures 5.15 and 5.16..... 138

**Table 5.3.** A comparison Table of theoretical and experimental broadened molecular orbital  $\Gamma_{Theo}$  and  $\Gamma_{Exp}$  of monomer molecules. Note: (The broadened molecular orbital  $\Gamma$  of the compounds **2**, **3** and **4** (**biNHC**, **N2F** and **o-S2F**) was only measured experimentally). .... 141

## List of abbreviations

DFT	Density Functional Theory
LDA	Local Density Approximation
GGA	Generalized Gradient Approximation
SCF	Self-Consistent Field
vdW	Van der Waals
DZ	Double- $\xi$ basis set
DZP	Double- $\xi$ polarized basis set
SIESTA	Spanish Initiative for Electronic Simulations with Thousands of Atoms
LCAOB	Linear Combination of Atomic Orbital Basis
T(E)	Transmission coefficient
LCAO	Linear Combination of Atomic Orbital
STM	Scanning Tunnelling Microscopy
SAM	Self-Assembled Monolayer
G	Electrical conductivity
AFM	Atomic Force Microscope
HOMO	Highest Occupied Molecular Orbital
LUMO	Lowest Occupied Molecular Orbital
$E_F^{\text{DFT}}$	DFT-predicted Fermi energy

## Chapter 1

### Molecular Electronics

#### 1.1 Introduction

Molecular electronics is a subfield of nanoscience<sup>1</sup> that refers to using individual or multiple molecules as building blocks to design and construct electrical components or molecular electronics devices such as transistors<sup>2,3</sup>, sensors<sup>4,5</sup>, memories<sup>6</sup>, current rectifiers<sup>7,8</sup>, and photovoltaics.<sup>9</sup> The molecular electronics field aims to study the electronic structures and thermal transport properties of the circuits that use single molecules as the essential building blocks<sup>10</sup>. Molecular electronics is a tremendously appealing subject because of its promise for sub-10nm electronic switches and rectifiers and its ability to provide sensitive platforms for single-molecule sensing.<sup>1</sup> For example, molecular electronics allows researchers to use molecules as electronically active components for various applications from a technical and practical perspective.<sup>11,12</sup> In addition, molecular recognition can create precisely crafted molecules with adjustable transport and desirable electronic characteristics. Moreover, microelectronics component, including SAMs (self-assembled monolayers)<sup>13,14</sup> single-molecule devices or carbon nanotube junctions<sup>15,16</sup>, hold the ability to probe room-temperature quantum properties, for instance, quantum interference and thermoelectricity at molecular scales or on the lowest scales possible.<sup>17-19</sup>

The first breakthrough came in 1974 by the Aviram and Ratner molecular current rectifier<sup>20</sup>, while Polymeropoulos and Sagiv researched the molecular-based tunnel junction (resistors) 30 years

ago.<sup>21</sup> As a standard example, Aviram and Ratner put a single molecule with electron donors and acceptor compartments between two metal electrodes. They demonstrated that a molecule coupled to the electrodes either functions as an electrical current conduit or controls the electrodes' charge transport properties in electronics devices.<sup>22</sup> In the 1980s, the innovation of scanning tunnelling microscopes (STM)<sup>13,23</sup> and atomic force microscopes (AFM)<sup>24</sup> by Gerd Binnig and Heinrich Rohrer led to increased attention and significantly expanded this field of molecular electronics. Due to developments in nanofabrication methods and the quantum theory of electronic transport during the last decades, it became possible to investigate and understand the fundamental features of electrical circuits in which molecules are utilised as essential building blocks to study their electronic transport properties.<sup>2,25,26</sup>

From a technological point of view, although molecules have several disadvantages, including instability at high temperatures and fabricating effective molecular junctions, which is challenging and costly, there are also practical reasons for investigating the use of molecules as the heart of electrical circuitry in various applications. Consequently, molecular electronics might provide the following main advantages<sup>1</sup>:

- The reduced size of small molecules, between 1 and 100 nm, could lead to a higher packing density of devices with the subsequent advantages in cost and more efficiency.
- Nanoscale self-assembly can make use of unique intermolecular interactions to produce structures. On the single-molecule scale, molecular recognition may change electrical behaviour, allowing for switching and sensing.
- The transport, binding, optical, and structural characteristics can be significantly altered by changing their composition and shape and synthetic molecular mechanisms have advanced considerably.

A key challenge in molecular electronics is the development of device platforms and understanding mechanisms of molecular charge transport throughout them.<sup>26</sup> The molecules sandwiched between two electrodes are the most common platform, the prototype molecular electronics device, and widely used construction to visualise the molecule and investigate molecular electronics characteristics.<sup>27-29</sup> Theoretical approaches have developed in tandem with experimental ones.<sup>30</sup> Researchers can now deal with more complex molecules and closely match their calculations to reality because of advancements in the methodologies used to calculate molecular electrical characteristics. Density Functional Theory (DFT) is now one of the most reliable and extensively used theoretical methods for determining the electronic structure of atomic structures and calculating charge transport in many-body structures. In addition, tight-binding models (TBMs) are one of the simplest ways of quantum transport modelling small systems.<sup>17,18,31</sup> These models allow one to comprehend essential molecule properties and investigate their potential usage as active components for nano applications. These technologies will enable researcher to understand basic molecule properties and analyse their possible use as functional components for nano applications. Combining DFT, implemented in the SIESTA<sup>32</sup> code and TBMs, with the Green's function formalism of electron transport implemented in the Gollum code later allowed researchers to practice critical concepts in the quantum transport theory needed to describe fundamental aspects of molecular junctions in the nanoscale.<sup>33</sup>

Charge transport mechanisms from one electrode to another via a single molecule are a significant challenge in developing molecular electrical devices.<sup>34-36</sup> The meaningful design of molecules as efficient components is required to approach a commercially practicable state for such devices, which involves size reduction and efficiency. This thesis investigates the essential features of enhancing the charge transport properties of molecular junctions. It will investigate the use of

chemical modification to improve the electrical conductivity of single molecules because the measured conductance depends on the electrode-molecule contact geometry, and will integrate the knowledge connections between the theory and the experiment to create and simulate (STM) devices.<sup>11</sup> In general, the subject of molecular electronics is still quite active and prospering despite four decades of intense advancement. The open quantum system's transport problem is unique and complex, opening a bright future for fundamental research and devices application expansion.

## 1.2 Thesis Outline

This thesis aims to study the theoretical methodologies for treating electron transport in two-terminal molecular junctions, using gold electrodes that form gold |molecule| gold structures. Density functional theory (DFT), implemented mainly in the SIESTA code<sup>32</sup>, is one of the main theoretical techniques that has been used in this thesis, as described in chapter two to study and understand the electronic properties of the single-molecule junctions. The second method that has been used in the single-particle transport theory is described in chapter three and is encoded in the quantum transport code GOLLUM<sup>37</sup>, which is a program that computes the transport and thermal properties based on the theoretical basis of Green's function scattering formalism and the transmission coefficient equations. In addition, chapter three briefly describes some basic subjects related to single-particle transport theory involving the Schrödinger equation and the Landauer formula for different transport regimes using several examples for different cases of the one-dimension systems. After introducing the basic chapters about nanoscale methods, which could be applied to model nano and molecular-scale devices, I will present the theoretical investigations of the research subject about a series of N-Heterocyclic carbenes molecules in the fourth and fifth chapters. Chapter 4 focuses on their electronic properties study to probe and understand charge transport through the NHC molecules. Chapter 5 analyses the charge transport mechanism in NHC-anchored molecular junctions. Finally, chapter 6 presents conclusions and future works.

### 1.3 Bibliography

1. Scheer, E., and Cuevas, J. C. (2010). *Molecular Electronics: An Introduction To Theory And Experiment: An Introduction to Theory and Experiment*. World Scientific Publishing Company.
2. Gonzalez, G. (2009). *Electron transport in single molecule magnet transistors and optical transitions in the 15nitrogen-vacancy-center in diamond*. University of Central Florida.
3. Li, Y., Mol, J. A., Benjamin, S. C., and Briggs, G. A. D. (2016). Interference-based molecular transistors. *Scientific Reports*, 6(1), 1-8.
4. Leary, E., Höbenreich, H., Higgins, S. J., Van Zalinge, H., Haiss, W., Nichols, R. J., ... and Smerdon, J. (2009). Single-molecule solvation-shell sensing. *Physical review letters*, 102(8), 086801.
5. Algharagholy, L., Pope, T., Al-Galiby, Q., Sadeghi, H., Bailey, S. W., and Lambert, C. J. (2015). Sensing single molecules with carbon–boron-nitride nanotubes. *Journal of Materials Chemistry C*, 3(39), 10273-10276.
6. Wang, C., Hu, Y., Lieber, C. M., and Sun, S. (2008). Ultrathin Au nanowires and their transport properties. *Journal of the American Chemical Society*, 130(28), 8902-8903.
7. Martin, A. S., Sables, J. R., and Ashwell, G. J. (1993). Molecular rectifier. *Physical Review Letters*, 70(2), 218–221.
8. DeHon, A. (2003). Array-based architecture for FET-based, nanoscale electronics. *IEEE Transactions On Nanotechnology*, 2(1), 23–32.
9. Kolmakov, A., and Moskovits, M. (2004). Chemical sensing and catalysis by one-dimensional metal-oxide nanostructures. *Annual Review of Materials Research*, 34(1), 151-180.
10. Wilkinson, L. A., Bennett, T. L. R., Grace, I. M., Hamill, J., Wang, X., Au-Yong, S., Ismael, A., Jarvis, S. P., Hou, S., Albrecht, T., Cohen, L. F., Lambert, C., Robinson, B. J., and Long, N. J. (2022). Assembly, structure and thermoelectric properties of 1,1'-dialkynylferrocene ‘hinges’. *Chemical Science*, 13(28), 8380–8387.
11. Famili, M. (2018). *Theory of molecular scale thermoelectricity*. Lancaster University (United Kingdom).
12. Ismael, A., Al-Jobory, A., Wang, X., Alshehab, A., Almutlg, A., Alshammari, M., Grace, I., Benett, T. L. R., Wilkinson, L. A., Robinson, B. J., Long, N. J., and Lambert, C. (2020). Molecular-scale thermoelectricity: As simple as ‘ABC’. *Nanoscale Advances*, 2(11), 5329–5334.
13. Ulman, A. (1996). *Formation and Structure of Self-Assembled Monolayers*. *Chemical Reviews*, 96(4), 1533–1554.

14. Bennett, T. L. R., Alshammari, M., Au-Yong, S., Almutlg, A., Wang, X., Wilkinson, L. A., Albrecht, T., Jarvis, S. P., Cohen, L. F., Ismael, A., Lambert, C. J., Robinson, B. J., and Long, N. J. (2022). Multi-component self-assembled molecular-electronic films: Towards new high-performance thermoelectric systems. *Chemical Science*, 13(18), 5176–5185.
15. Yzambart, G., Rincón-García, L., Al-Jobory, A. A., Ismael, A. K., Rubio-Bollinger, G., Lambert, C. J., Agraït, N., and Bryce, M. R. (2018). Thermoelectric Properties of 2,7-Dipyridylfluorene Derivatives in Single-Molecule Junctions. *The Journal of Physical Chemistry C*, 122(48), 27198–27204.
16. Sanvito, S., Kwon, Y.-K., Tománek, D., and Lambert, C. J. (2000). Fractional Quantum Conductance in Carbon Nanotubes. *Physical Review Letters*, 84(9), 1974–1977.
17. Lambert, C. J. (2021). *Quantum Transport in Nanostructures and Molecules: An introduction to molecular electronics*. IOP Publishing.
18. Sadeghi, H. (2016). *Theory of electron and phonon transport in nano and molecular quantum devices: design strategies for molecular electronics and thermoelectricity*. Lancaster University (United Kingdom).
19. Ismael, A. K., Rincón-García, L., Evangeli, C., Dallas, P., Alotaibi, T., Al-Jobory, A. A., Rubio-Bollinger, G., Porfyrakis, K., Agraït, N., and Lambert, C. J. (2022). Exploring seebeck-coefficient fluctuations in endohedral-fullerene, single-molecule junctions. *Nanoscale Horizons*, 7(6), 616–625.
20. Joachim, C., and Ratner, M. A. (2005). Molecular Electronics: Some Views on Transport Junctions and beyond. *Proceedings of the National Academy of Sciences of the United States of America*, 102(25), 8801–8808.
21. Bovensiepen, U., Biermann, S., and Perfetti, L. (2012). The electronic structure of solids. *Dynamics at Solid State Surfaces and Interfaces*, 2, 1-25.
22. Jayamurugan, G., Gowri, V., Hernández, D., Martin, S., González-Orive, A., Dengiz, C., Dumele, O., Pérez-Murano, F., Gisselbrecht, J.-P., Boudon, C., Schweizer, W. B., Breiten, B., Finke, A. D., Jeschke, G., Bernet, B., Ruhlmann, L., Cea, P., and Diederich, F. (2016). Design and Synthesis of Aviram-Ratner-Type Dyads and Rectification Studies in Langmuir-Blodgett (LB) Films. *Chemistry - A European Journal*, 22(30), 10539–10547.
23. Huffman, E. (2010). *Scanning Tunneling Microscopy and Low Energy Electron Microscopy of Ir and Ag adsorbed on Ge(110) and Ge(111) Surfaces*.
24. Wold, D. J., and Frisbie, C. D. (2000). Formation of Metal–Molecule–Metal Tunnel Junctions: Microcontacts to Alkanethiol Monolayers with a Conducting AFM Tip. *Journal of the American Chemical Society*, 122(12), 2970–2971.
25. Wang, X., Ismael, A., Ning, S., Althobaiti, H., Al-Jobory, A., Girovsky, J., ... and Ford, C. J. (2022). Electrostatic Fermi level tuning in large-scale self-assembled monolayers of oligo (phenylene–ethynylene) derivatives. *Nanoscale Horizons*, 7(10), 1201-1209.

26. Afsari, S., Li, Z., and Borguet, E. (2014). Orientation-Controlled Single-Molecule Junctions. *Angewandte Chemie International Edition*, 53(37), 9771–9774.
27. Heath, J. R. (2009). Molecular Electronics. *Annual Review of Materials Research*, 39(1), 1–23.
28. Ismael, A. K., Grace, I., and Lambert, C. J. (2015). Increasing the thermopower of crown-ether-bridged anthraquinones. *Nanoscale*, 7(41), 17338–17342.
29. Su, T. A., Neupane, M., Steigerwald, M. L., Venkataraman, L., and Nuckolls, C. (2016). Chemical principles of single-molecule electronics. *Nature Reviews Materials*, 1(3), 16002.
30. Xue, Y., and Ratner, M. A. (2005). Theoretical principles of single-molecule electronics: A chemical and mesoscopic view. *International Journal of Quantum Chemistry*, 102(5), 911–924.
31. Thoss, M., and Evers, F. (2018). Perspective: Theory of quantum transport in molecular junctions. *The Journal of Chemical Physics*, 148(3), 030901.
32. Artacho, E., Anglada, E., Diéguez, O., Gale, J. D., García, A., Junquera, J., Martin, R. M., Ordejón, P., Pruneda, J. M., Sánchez-Portal, D., and Soler, J. M. (2008). The SIESTA method; developments and applicability. *Journal of Physics: Condensed Matter*, 20(6), 064208.
33. Al-Khaykanee, M. K., Ismael, A. K., Grace, I., and Lambert, C. J. (2018). Oscillating Seebeck coefficients in  $\pi$ -stacked molecular junctions. *RSC Advances*, 8(44), 24711–24715.
34. Lambert, C. J. (2012). Basic concepts of quantum interference and electron transport and in single-molecule electronics. *Chemical Society Reviews*, 18.
35. Wang, X., Bennett, T. L. R., Ismael, A., Wilkinson, L. A., Hamill, J., White, A. J. P., Grace, I. M., Kolosov, O. V., Albrecht, T., Robinson, B. J., Long, N. J., Cohen, L. F., and Lambert, C. J. (2020). Scale-Up of Room-Temperature Constructive Quantum Interference from Single Molecules to Self-Assembled Molecular-Electronic Films. *Journal of the American Chemical Society*, 142(19), 8555–8560.
36. Ismael, A. K., and Lambert, C. J. (2020). Molecular-scale thermoelectricity: A worst-case scenario. *Nanoscale Horizons*, 5(7), 1073–1080.
37. Ferrer, J., Lambert, C. J., García-Suárez, V. M., Manrique, D. Z., Visontai, D., Oroszlany, L., Rodríguez-Ferradás, R., Grace, I., Bailey, S. W. D., Gillemot, K., Sadeghi, H., and Algharagholy, L. A. (2014). GOLLUM: A next-generation simulation tool for electron, thermal and spin transport. *New Journal of Physics*, 16(9), 093029.

## **Chapter 2**

### **Density Functional Theory**

This chapter introduces a brief overview of the Density Functional Theory (DFT) and SIESTA (Spanish Initiative for Electronic Simulations with Thousands of Atoms) code involving the general concepts and numerical applications of the SIESTA DFT code as described below. This theoretical method is considered the primary tool applied in this research work to study the electronic structure properties of all studied systems, including the Hamiltonian of the isolated molecules, wave functions, geometry structure optimisation, binding energies (bond length), and the transport of electrons through nanoscale scatter or single molecules connected to electrodes or semi-infinite leads. In order to obtain the structural and electronic information, I shall extract the Hamiltonian, which can be an output of DFT calculations, of the desired system and then employ them to investigate the transport properties of the molecular junctions, where the latter part will discuss in detail in chapter 3.

#### **2.1 Introduction**

Theoretical condensed matter physics aims to formulate the fundamental building components of materials, electrons, and nuclei to explain their electronic properties. The interactions between electrons and nuclei give rise to a broad spectrum of features in molecules, solids, polymers, and

other objects. Electronic transport has been a remarkably successful section of condensed matter that has gotten much attention. However, the enormity of these interactions and the computational limit of our time make the condensed theoretical matter a very challenging field. In the last 50 years, physicists have devised various methodologies with varying degrees of accuracy, impact, and size. Molecular Dynamics (MD), Density Functional Theory (DFT), and Tight Binding Theory (TB) are some of these methodologies.<sup>1,2</sup>

Investigating the behaviour of electrons in the wires can explain the electrical properties of molecular wires as a simple example. However, it requires a reliable technique to determine the structural and electrical behaviour to understand molecular electronics devices' behaviour or nano-scale simulations, which density function theory (DFT) provides. DFT has proven to be one of the foremost efficient and prospective theories for predicting the electronic structure of the ground state of several systems, such as atoms, molecules, and crystals, in physics, materials, and chemistry. The term "density functional theory" refers to the usage of electron density functionals.<sup>3</sup> This technique investigate the behaviour of electrons on relatively large-scale calculations of many-body Schrödinger equation, which are based on the Hamiltonian, which describes the system.<sup>4</sup> DFT is commonly used to solve the many-body problem simplified to find Hamiltonian, eigenvalues, eigenfunctions, and anther properties of the complex systems.

## 2.2 Many-body problem

In theoretical solid-state physics and the quantum mechanical behaviour of a physical or chemical system, involves studying the observable properties of large systems comprising of many atoms, which could achieve by finding the solution of the Schrödinger wave equation. The stationary many-body Schrödinger equation is <sup>5</sup> :

$$\begin{aligned} \hat{H}\psi_i(\vec{r}_1, \vec{r}_2, \dots, \vec{r}_N, \vec{R}_1, \vec{R}_2, \dots, \vec{R}_M) \\ = E_i\psi_i(\vec{r}_1, \vec{r}_2, \dots, \vec{r}_N, \vec{R}_1, \vec{R}_2, \dots, \vec{R}_M) \end{aligned} \quad (2.1)$$

where  $\hat{H}$  is the Hamiltonian operator consisting of  $M$  nuclei and  $N$  electrons, which include a complete description of the electronic structure of the system such as the energies and electron densities, and  $\psi_n$  is the wavefunction of electronic  $r$ , and nuclear  $R$ . The full Hamiltonian operator of a general approach as the sum of the kinetic energies of the electrons and nuclei ( $\hat{T}$ ) and the Coulomb interactions between them ( $\hat{V}$ ) as follows:

$$\begin{aligned} \hat{H} = \underbrace{\sum_{i=1}^N \left(-\frac{\hbar^2}{2m_i} \nabla_i^2\right)}_{\hat{T}_e} + \underbrace{\sum_{i=1}^N \sum_{i \neq j}^N \left(\frac{e^2}{|r_i - r_j|}\right)}_{\hat{V}_{e-e}} + \underbrace{\sum_{\alpha=1}^I \left(-\frac{\hbar^2}{2m_\alpha} \nabla_\alpha^2\right)}_{\hat{T}_n} \\ + \underbrace{\sum_{I=1}^M \sum_{I \neq J}^M \left(\frac{Z_I Z_J e^2}{|R_I - R_J|}\right)}_{\hat{V}_n} - \underbrace{\sum_{i=1}^N \sum_{I=1}^M \left(\frac{Z_I e^2}{|r_i - R_I|}\right)}_{\hat{V}_{e-n}} \end{aligned} \quad (2.2)$$

This equation of many-body quantum mechanics interacting particles, which contains at the first line the kinetic energy and the mutual Coulomb interaction of the electrons, and the second part are the related terms for the nuclei. The last line describes the Coulomb interaction between the electrons and the nuclei, which depends on electrons  $r_i$  and nuclei  $R_I$  <sup>6</sup>, where  $i$  and  $j$  denote the

$N$ -electrons. In addition,  $m_\alpha$ ,  $R_I$ , and  $Z_I e^2$  are the mass, coordinates, and the charge of the  $I^{th}$  nucleus. Similarly,  $m_i$ ,  $r_i$  and  $-e$  are the mass, coordinates, and the charge of the  $i^{th}$  electron.

In general, for any system with more than a few electrons and nuclei, finding the eigenstates and eigenvalues of the Schrödinger equation becomes impractical. Therefore, to reduce the size of this problem, an approximation is needed, which is the Born-Oppenheimer approximation.<sup>5</sup>

### 2.3 Born-Oppenheimer approximation

The Schrödinger equation for a many-atom molecule can be separated into two equations using a method known as the Born-Oppenheimer approximation<sup>6</sup>: an electronic Schrödinger equation and a nuclear Schrödinger equation Eq. 2.2 is as follows:

$$\begin{aligned}\hat{H}_e \psi_e(r_n, R_M) &= E_e \psi_e(r_n, R_M) \\ \hat{H}_N \psi_N(R_M) &= E_N \psi_N(R_M)\end{aligned}\tag{2.3}$$

$E_e(R_M)$  is the ground state energy of the electrons for a given set of nuclei coordinates. The effect of nuclear kinetic energy on electrons is ignored in this assumption, and this is because nuclear masses are substantially greater than electron masses. The Born Oppenheimer approximation<sup>7</sup> corresponds to ignoring the nuclear kinetic energy. The electron degrees of freedom are considered in this solution of the Schrödinger equation. Therefore, the Hamiltonian from Eq. 2.3 to be written for the electrons as

$$\hat{H}_e = \hat{T}_e + \hat{V}_{e-e} + V_{ext}\tag{2.4}$$

where  $V_{ext}$  represents an external potential acting on the electrons due to the frozen nuclei. On other side, some approximations, such as DFT, are required to solve the Schrödinger equation for

this system. Density functional theory has the advantage of expressing physical quantities in terms of ground-state density.

## **2.4 Density Functional theory**

One primary theoretical description of nano-scale simulations of electronic structure properties of atoms and molecules is Density Functional Theory (DFT). It is a first-principles technique to predict a material's properties with as few approximations as appropriate. It can be applied to find highly accurate results on smaller systems.<sup>8</sup>

Hohenberg and Kohn introduced<sup>3</sup> in 1964 the physical theories that underpin DFT's fundamental assertion by showing that the ground state energy of a system of interacting electrons is a unique function of the electronic charge density.<sup>7,9</sup> In 1965 Kohan and Sham provided a method to relate the ground states with interacting particles to a non-interacting particles system through their charge density. These methods are described in the following two sections.

### **2.4.1 The Hohenberg-Kohn theorems**

The Hohenberg-Kohn (HK) theorem<sup>3</sup> is the cornerstone of density functional theory (DFT). The critical point of this theorem is that any system of a fully interacting N-electron or travelling in a potential field is determined by its ground-state energy, which its electron density  $\rho(r)$  defines the ground state energy of this system. The HK theorem evolved dramatically because two simple theorems proposed the electron density  $\rho(r)$  as the fundamental variable. The first theorem can be considered that the Coulomb potential arising from the frozen nuclei of the many-body

Hamiltonian as a constant external potential ( $V_{ext}(r)$ ) has unique correspondence with the corresponding ground state electronic density.<sup>5</sup> In other words, the external potential is a unique functional of the electronic density. To prove this, it starts with the assumption that includes those two potentials  $V_{ext}(r)$  and  $V'_{ext}(r)$ , which differ by more than a constant, give rise to the same ground-state density  $\rho(r)$ . It leads to two different Hamiltonians of two different Schrödinger equations are denoted  $\hat{H}$  and  $\hat{H}'$ .

According to the variational principle to find approximations to the ground state, the energy is minimal with respect to a wave function variation and represents an upper bound on the ground state energy  $E_0$ . By assume the total energy from one of the Schrödinger equations matches the ground state as follow:

$$E_0 = \langle \psi_0 | \hat{H} | \psi_0 \rangle < \langle \psi'_0 | \hat{H} | \psi'_0 \rangle \quad (2.5)$$

This is due to the distinction between the two Hamiltonians,

$$\langle \psi_0 | \hat{H} | \psi_0 \rangle = \langle \psi_0 | \hat{H}' | \psi_0 \rangle + \langle \psi'_0 | V_{ext}(r) - V'_{ext}(r) | \psi'_0 \rangle \quad (2.6)$$

Hence

$$E_0 < E'_0 + \langle \psi_0 | V_{ext}(r) - V'_{ext}(r) | \psi_0 \rangle \quad (2.7)$$

The difference between the two potentials is a direct result of the difference, Hence

$$E'_0 < E_0 + \langle \psi_0 | V_{ext}(r) - V'_{ext}(r) | \psi_0 \rangle \quad (2.8)$$

By combining the two inequalities mentioned previously, then

$$\begin{aligned} E'_0 + E_0 < E_0 + E'_0 + \langle \psi_0 | V_{ext}(r) - V'_{ext}(r) | \psi_0 \rangle \\ - \langle \psi_0 | V_{ext}(r) - V'_{ext}(r) | \psi_0 \rangle \end{aligned} \quad (2.9)$$

The two terms on the right-hand side add up to zero since and then the two potentials have the same corresponding electron densities  $\rho(r)$ .

$$\int dr \rho(r)(V_{ext}(r) - V'_{ext}(r)) - \int dr \rho(r)(V_{ext}(r) - V'_{ext}(r)) = 0 \quad (2.10)$$

Substitute Eq. 2.10. into Eq. 2.11 to obtain

$$E'_0 + E_0 < E_0 + E'_0 \quad (2.11)$$

As a result, two different external potentials cannot yield the same ground-state density, as demonstrated by this equation. This conclusion allows us to write the total energy as a function of the electron density,

$$E(\rho(r)) = \int V_{ext}(r)\rho(r) dr + F[\rho(r)] \quad (2.12)$$

or equivalently

$$E(\rho(r)) = \int V_{ext}(r) \rho(r) dr + \langle \psi_0 | \hat{T} + \hat{V} | \psi_0 \rangle \quad (2.13)$$

where  $F[\rho(r)]$  is a unique and universal functional of the electron density for the energy  $E(\rho(r))$ , which does not depend on the external potential. The exact ground state is the global minimum value of the functional  $F[\rho(r)]$ , and that states the second theorem of the HK.<sup>10</sup>

$$E(\rho(r)) = \langle \psi | \hat{H} | \psi \rangle > E_0 \rho(r) \quad (2.14)$$

All ground-state properties of a many-body system may be determined from  $E(\rho(r))$ , and the ground-state energy  $E(\rho(r))$  is at its minimum only if  $\rho(r)$  is the ground state charge density. Consequently, the solution of the HK theorem is based on the minimisation of the ground-state energy concerning density.<sup>11</sup> On the other hand, the HK theorem does not provide guidance on how to approach the ground-state energy functional; it simply confirms its presence.<sup>12</sup>

### 2.4.2 Kohn-Sham equation

This enables accurate handling of molecular systems in many circumstances that are impossible with more typical quantum mechanical methods.<sup>13</sup> As mentioned in the previous section, obtaining the ground-state density leads to calculating the ground-state energy. However, the exact form of the functional  $F[\rho(r)]$  shown in Eq. 2.12 is not known, which the kinetic energy term, as well as the internal energy of the interacting particles, cannot be represented as a function of density  $\rho(r)$ . Therefore, Kohn and Sham's equation proposed the solution.<sup>12</sup> It proposed a method for extracting

the most significant terms of the ground state energy, namely the kinetic energy and the classical Coulomb (Hartree) energy and treating them exactly using the HK theorem to construct an effective single-particle system that reproduces the density of the original, fully interacting system.

The Kohn-Sham method characterises an interacting system of electrons by utilising a non-interacting auxiliary system in an effective potential  $V_{eff}(r)$  by replacing the original Hamiltonian of the system with an effective Hamiltonian at the same ground-state charge density  $\rho(r)$  as the original system. The effective potential is as follows,

$$V_{eff}(r) = \int dr' \frac{\rho(r')}{|r-r'|} + V_{ext}(r) + V_{xc}(r) \quad (2.15)$$

where the first part is the electrostatic energy from the electron charge density distribution (also known as Hartree energy),  $V_{ext}(r)$  is the external potential due to the presence of stationary nuclei, and  $V_{xc}(r)$  is the exchange-correlation potential, which is the derivative of exchange energy and describes the remaining contribution of interacting electrons to the exact energy of the system.

$$V_{xc}(r) = \frac{\delta E_{xc}(\rho(r))}{\delta \rho(r)} \quad (2.16)$$

As a result, the Hamiltonian of Kohn-Sham yields:

$$\hat{H}^{KS} \psi_i(r) = \left[ \frac{-\hbar^2}{2m_e} \nabla^2 + V_{eff}(r) \right] \psi_i(r) = E_i \psi_i(r) \quad (2.17)$$

Eq. 2.17 is the Kohn-Sham equation, where  $\hat{H}^{KS}$  is the kinetic energy of individual particles that interact with an effective potential, and  $E_i$  is the system's eigenvalues. The Kohn-Sham wavefunctions  $\psi_i(r)$  explain the motion of the  $i^{th}$  particle in an effective potential  $V_{eff}(r)$ . The

Kohn-Sham approach is self-consistent cycle <sup>14</sup>, since  $V_{eff}(r)$  is dependent on the ground state density  $\rho(r)$  and the energy  $E_i$  according to the general scheme illustrated in Figure 2.1.<sup>15</sup>

The self-consistent calculation starts by calculating the Hartree potential and the exchange correlation potential. The Kohn-Sham equations are then solved, yielding a new density. This self-consistent iterations are repeated many times until requisite convergence terms are satisfied. Finally, once the initial electronic structure of a system has been determined, the forces on the nuclei be calculated and new atomic configuration to minimize these forces obtained. The ground state electronic properties of the system, such as total energy, binding energies, and forces, could be computed using the obtained ground state geometry.

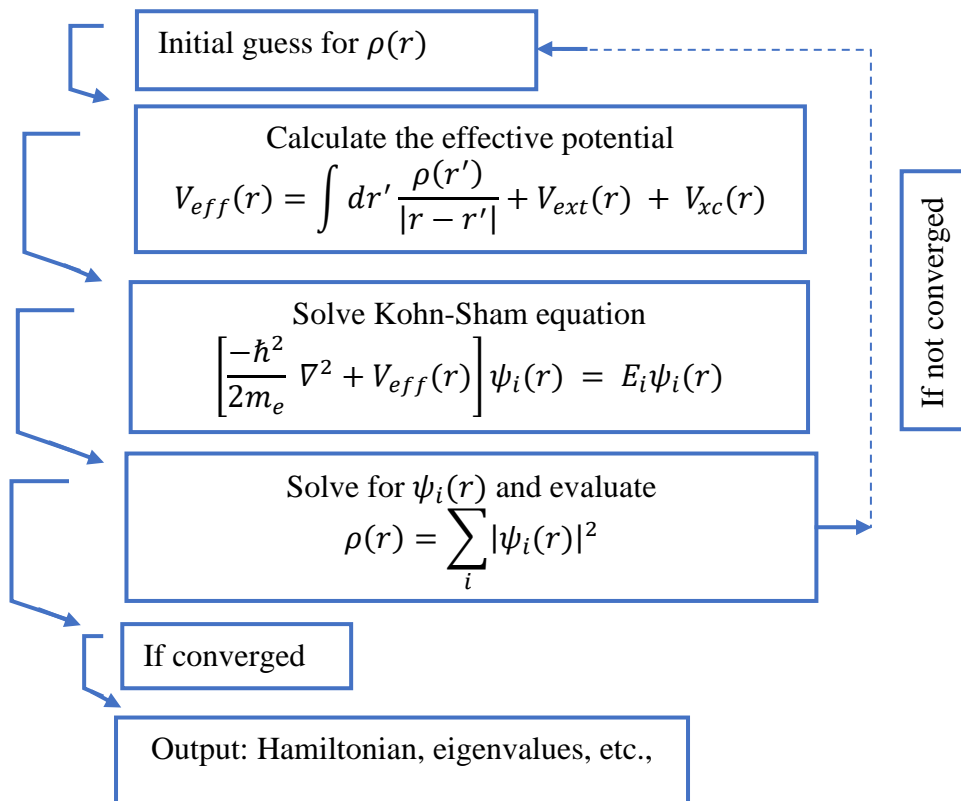


**Figure 2.1.** A Schematic illustration of the DFT self-consistent cycle

### 2.4.3 Exchange-correlation functional

According to the Kohn- Sham approach, the exchange-correlation potential  $V_{xc}(r)$  can be defined as a functional derivative of the exchange-correlation energy  $E_{xc}$ .<sup>16</sup> Since, there is no exact form to evaluate the exchange-correlation energy, approximation methods and their quality determine the accuracy of a DFT computation.<sup>17</sup> The simplest approximation, is the Local Density Approximation (LDA), assumes that the density can be treated as a uniform electron gas, which derives the  $E_{xc}$  from the local electron density.

The Local Density Approximation (LDA) is accurate for slowly varying electron densities.<sup>9</sup> The LDA functional can be improved by including the density gradient ( $\nabla\rho$ ) by an alternate approximation, which is Generalised Gradient Approximation (GGA). There are a variety of approximations in addition to LDA and GGA, such as the (VDW) approximation, which uses the Van der Waals energy functional. Although the precision of these approximations varies, they all produce acceptable results with some systems.<sup>12</sup>

## 2.5 SIESTA implementation of DFT

The Spanish Initiative for Electronic Simulations with Thousands of Atoms (SIESTA)<sup>18</sup> code is a well-known implementation of the DFT. It is a computer program implementation method to perform electronic structure calculations and molecular dynamics simulations of molecules and solids. SIESTA employs a variety of approximation approaches to solve the Kohn-Sham equations, which are explained in the following two sections.

### 2.5.1 Pseudopotential approximation

The Kohn-Sham approach has been shown to solve many-body problems, as previously mentioned. However, solving an eigenvalue problem for a system with many atoms, such as a molecule, requires a long time on a computer. One method to solve the computational problem is to reduce the number of electrons by introducing the pseudopotential approximation, in which norm-conserving pseudopotentials represent the interactions between the electrons and the ionic cores in SIESTA according to the Troullier-Martins parametrisation.<sup>19</sup> This concept's premise is that the electrons in an atom are divided into two types: core and valence. Core electrons are found in filled atomic shells, whereas valence electrons are found in partially filled shells. Because core electrons are spatially restricted around the nucleus, only valence electron states overlap when atoms are brought together. Hence valence electrons contribute to the formation of molecular orbitals in most systems. This estimate is since an atom's core electrons do not participate in chemical bonding and are relatively unaffected by the atom's chemical surroundings.<sup>20</sup>

As a result, this drastically reduces the number of electrons in a system, lowering the time and memory requirements for calculating the properties of molecules with many electrons.

### 2.5.2 Basis Sets

In order to represent the Kohn-Sham wavefunction  $\psi_i = \sum_{j=1}^L C_{ji} \varphi_j$  into an algebraic equation suitable for efficient implementation on a computer for the SIESTA code, it can be considered that numerical atomic orbitals (NAO) are localised basis sets in which the valance electronic states are

Linear Combination of Atomic Orbitals (LCAO) that are constructed from the orbitals of the atoms.<sup>21,22</sup>

Furthermore, the variational parameters of the construction of these orbitals of the atoms are the size (number of atomic orbitals per atom), range (spatial extension of the orbitals or the cut-off radius), and shape (of the radial part). These atom-centred orbitals (such as  $\varphi_j$  is the  $j^{\text{th}}$  atom centred orbital) are denoted by:

$$\varphi_{Ilnm}(r) = R_{In}(|r_I|)Y_{lm}(\hat{r}_I) \quad (2.18)$$

Each basis set is a product of a radial wavefunction  $R_{nl}(r)$  and  $Y_{lm}$  which is a spherical harmonic. where  $I$  is the index of the atom,  $l$  is the orbital angular momentum is,  $m$  is the magnetic quantum number, and  $n$  indicates that the same angular momentum numbers might have many orbitals.

The size of the basis set can be chosen based on available time, computing power, and the level of accuracy necessary. A single- $\zeta$  basis is the minimal basis set which has one radial function per angular momentum. Multiple- $\zeta$  have multiple orbitals ( $n$ ) corresponding to the same angular momentum with different radial parts. Further accuracy using multiple- $\zeta$  polarised basis sets have shells with varied atomic symmetry allowing for angular flexibility if applying a small electric field to the orbital. These are obtained by including wave functions with different angular momenta corresponding to orbitals unoccupied in the atom.<sup>23-25</sup>

### 2.5.3 Calculating binding energy using the counterpoise method

Using the DFT calculations to compute the ground state geometry of different system configurations allows one to calculate the distance between two different system parts, which refers to the binding energy of two configurations. However, due to localised basis sets focused on the nucleus, these calculations are prone to inaccuracies. When atoms are shifted, the basis set changes, and any error caused by the incompleteness of the basis set will also change. For example, the artificial strengthening of atomic interaction (such as the overlapping basis sets of closed-shell atoms) will give inaccurate total energy to the system. In general, the solution to this type of error has been demonstrated by the basis set superposition error correction (BSSE)<sup>26</sup> or the counterpoise correction.<sup>27</sup> If two molecular systems, denoted  $A$  and  $B$ , the binding energy of the interaction may be expressed as:

$$\Delta E(AB) = E^{AB} - (E^A + E^B) \quad (2.19)$$

where  $E^{AB}$  is the total energy of the dimer systems  $A$  and  $B$ , while the total energy of the two isolated systems is  $E^A$  and  $E^B$ . At this point, the superscript denotes the basis set used in each calculation such as  $A$  is just the basis set of system  $A$  is the basis set of  $B$  and  $AB$  is the combined basis set of both  $A$  and  $B$ .

To perform these corrections that remove the numerical errors in SIESTA calculations, the energy calculations are carried in the same total basis set  $AB$  by employing ghost states (basis set functions which have no electrons or nuclear charge).<sup>28</sup> Hence, the total energy of the systems  $A$  and  $B$  in the dimer basis is formulated by the following equation,

$$\Delta E(AB) = E_{AB}^{AB} - (E_A^{AB} + E_B^{AB}) \quad (2.20)$$

Where  $E_A^{AB}$  and  $E_B^{AB}$  are the energy of the system  $A$  and  $B$  evaluated on the basis sets of the dimer<sup>29</sup>, This crucial notion has been effectively used in various systems to produce reliable and realistic outcomes in this thesis.

## 2.6 Conclusion

This chapter has reviewed some main general concepts of DFT and the SIESTA code for solving the many-body Schrödinger equation in terms of the ground-state density such as the Hohenberg-Kohn theorems, the Kohn-Sham equation. As a solution to the many-body problem of finding the eigenvalues and eigenstates of the Hamiltonian operator of a system consisting of nuclei and electrons, some approximations are required, such as the Born-Oppenheimer approximation. Since the exact form of the exchange-correlation functional (the difference in energy between the non-interacting and interacting systems) of Kohn-Sham method cannot be determined, approximation is inevitable. The two most widely used exchange and correlation energies approximations are the Local Density Approximation (LDA) and the Generalized Gradient Approximation (GGA). Eventually, the SIESTA DFT code was presented with a few technical aspects such as pseudopotential approximation and the basis sets as approaches to perform all the electronic structure calculations, including binding energy simulations.

## 2.7 Bibliography

1. Kim, G.-H., Shao, L., Zhang, K., and Pipe, K. P. (2013). Engineered doping of organic semiconductors for enhanced thermoelectric efficiency. *Nature Materials*, 12(8), 719–723.
2. Atkins, P. W., and Friedman, R. S. (2011). *Molecular quantum mechanics*. Oxford university press.
3. Görling, A. (1999). Density-functional theory beyond the Hohenberg-Kohn theorem. *Physical Review A*, 59(5), 3359–3374.
4. Soler, J. M., Artacho, E., Gale, J. D., García, A., Junquera, J., Ordejón, P., and Sánchez-Portal, D. (2002). The SIESTA method for ab initio order- N materials simulation. *Journal of Physics: Condensed Matter*, 14(11), 2745–2779.
5. Lee, T. D., and Yang, C. N. (1959). Many-Body Problem in Quantum Statistical Mechanics. I. General Formulation. *Physical Review*, 113(5), 1165–1177.
6. Born, M., Oppenheimer, J. R., and Physik, A. (1927). On the Quantum Theory of Molecules. 32.
7. Kolesov, G., Kaxiras, E., and Manousakis, E. (2018). Density functional theory beyond the Born-Oppenheimer approximation: Accurate treatment of the ionic zero-point motion. *Physical Review B*, 98(19), 195112.
8. Stanton, J. F. (2001). *A Chemist’s Guide to Density Functional Theory* By Wolfram Koch (German Chemical Society, Frankfurt am Main) and Max C. Holthausen (Humbolt University). *Journal of the American Chemical Society*, 123(11), 2701–2701.
9. Eschrig, H. (2003). *The fundamentals of density functional theory (Vol. 2)*. Leipzig: Edition am Gutenbergplatz.
10. Levy, M. (1979). Universal variational functionals of electron densities, first-order density matrices, and natural spin-orbitals and solution of the v-representability problem. *Proceedings of the National Academy of Sciences*, 76(12), 6062–6065.
11. Hohenberg, P., and Kohn, W. (1964). Inhomogeneous Electron Gas. *Physical Review*, 136(3B), B864–B871.
12. Kohn, W. (1999). Nobel Lecture: Electronic structure of matter—wave functions and density functionals. *Reviews of Modern Physics*, 71(5), 1253–1266.
13. Brockherde, F., Vogt, L., Li, L., Tuckerman, M. E., Burke, K., and Müller, K.-R. (2017). Bypassing the Kohn-Sham equations with machine learning. *Nature Communications*, 8(1), 872.
14. Kohn, W., and Sham, L. J. (1965). Self-Consistent Equations Including Exchange and Correlation Effects. *Physical Review*, 140(4A), A1133–A1138.

15. Shan, N., Zhou, M., Hanchett, M. K., Chen, J., and Liu, B. (2017). Practical principles of density functional theory for catalytic reaction simulations on metal surfaces – from theory to applications. *Molecular Simulation*, 43(10–11), 861–885.
16. Zhao, Y., Schultz, N. E., and Truhlar, D. G. (2005). Exchange-correlation functional with broad accuracy for metallic and nonmetallic compounds, kinetics, and noncovalent interactions. *The Journal of Chemical Physics*, 123(16), 161103.
17. Burke, K. (2012). Perspective on density functional theory. *The Journal of chemical physics*, 136(15), 150901.
18. Artacho, E., Anglada, E., Diéguez, O., Gale, J. D., García, A., Junquera, J., Martin, R. M., Ordejón, P., Pruneda, J. M., Sánchez-Portal, D., and Soler, J. M. (2008). The SIESTA method; developments and applicability. *Journal of Physics: Condensed Matter*, 20(6), 064208.
19. Troullier, N., and Martins, J. L. (1991). Efficient pseudopotentials for plane-wave calculations. II. Operators for fast iterative diagonalization. *Physical Review B*, 43(11), 8861–8869.
20. Kleinman, L., and Bylander, D. M. (1982). Efficacious Form for Model Pseudopotentials. *Physical Review Letters*, 48(20), 1425–1428.
21. Perdew, J. P., and Zunger, A. (1981). Self-interaction correction to density-functional approximations for many-electron systems. *Physical Review B*, 23(10), 5048–5079.
22. Fernandez-Seivane, L., Oliveira, M. A., Sanvito, S., and Ferrer, J. (2007). On-site approximation for spin-orbit coupling in LCAO density functional methods. *Journal of Physics: Condensed Matter*, 19(48), 489001.
23. Cuadrado, R., Pruneda, M., García, A., and Ordejón, P. (2018). Implementation of non-collinear spin-constrained DFT calculations in SIESTA with a fully relativistic Hamiltonian. *Journal of Physics: Materials*, 1(1), 015010.
24. Famili, M. (2018). Theory of molecular scale thermoelectricity. Lancaster University (United Kingdom).
25. Ismael, A. (2017). Towards molecular-scale sensing and thermoelectric energy harvesting (Doctoral dissertation, Lancaster University).
26. Kobko, N., and Dannenberg, J. J. (2001). Effect of Basis Set Superposition Error (BSSE) upon ab Initio Calculations of Organic Transition States. *The Journal of Physical Chemistry A*, 105(10), 1944–1950.
27. Sherrill, C. D. (2010). Counterpoise correction and basis set superposition error. School of Chemistry and Biochemistry, Georgia Institute of Technology.

28. Sinnokrot, M. O., Valeev, E. F., and Sherrill, C. D. (2002). Estimates of the Ab Initio Limit for  $\pi$ - $\pi$  Interactions: The Benzene Dimer. *Journal of the American Chemical Society*, 124(36), 10887–10893.
29. van Duijneveldt, F. B., van Duijneveldt-van de Rijdt, J. G. C. M., and van Lenthe, J. H. (1994). State of the Art in Counterpoise Theory. *Chemical Reviews*, 94(7), 1873–1885.

## Chapter 3

### Theory of single-particle transport

As discussed, previous, Density functional calculations have evolved as a required simulation tool hand in hand with experimental studies, permitting researchers to build a measurable vision of transport mechanisms in nanoscale junctions and create projections to direct future practical investigations. In addition, to the structural and electronic information that DFT provides, involving all the electronic properties derivable from the Hamiltonian of such as DFT code SIESTA, electron transport theory used within the scattering calculations also enables the building of a simple tight-binding Hamiltonian using Hückel parameters that can be applied to some simple structures as described below in this chapter. Hence, the theory of quantum transport was applied to one-dimensional crystalline models connected to electrodes to understand some fundamental concepts of electron transport and illustrate the generic features for estimating the conductance properties as in the following sections.

#### 3.1 Introduction

The purpose of molecular electronics is to understand the electrical properties of molecular junctions when a molecule (or suitably small structure) is bound to bulk electrodes, such that ballistic transport can occur through its energy levels. The composite structure of a nanoscale device generated by inserting a molecule or other phase-coherent structure between electrodes and allowing the electrodes to conduct a current into or out of the device is called an open system.<sup>1</sup>

The coupling strength between the leads and the molecule is typically weak compared to intra-electrode or intra-molecule bond strengths, resulting in scattering from the electrode to the molecule and from the molecule to the electrode. As a result, understanding and calculating the scattering processes between the electrodes attached to a molecule requires a broad approach.

The modern transport theory used to describe single-molecule junctions is based on scattering theory and the Landauer formula. The electronic properties of junctions can be studied in various ways. However, this thesis concentrates primarily on Green's function formalism. Analytical and numerical methods contribute to investigating the electronic transport properties of single molecules. One of the simplest methods of quantum transport modelling of small systems utilizes tight-binding models (TBM), which represent the wave function as a linear combination of atomic orbitals (LCAO). TBM is useful because it allows one to develop critical concepts of quantum transport, which are common to more materials-specific models on density functional theory (DFT).<sup>2,3</sup>

The first purpose of this chapter is to introduce these theoretical approaches to solving some problems for different structures systems. The solutions are based on the illustration of fundamental concepts such as the Schrödinger wave equation and its common property to calculate the eigenfunction and eigenvalue of the Hamiltonian matrix, which involves various types of one-dimension crystalline chains such as an infinite linear chain, a finite linear chain, and a periodic chain of atoms or ring. The second purpose is to provide an overview of the scattering theory and how it relates to transport properties and Green's function for different transport regimes and exciting features based on the Landauer formalism for estimating the electrical conductance properties of materials.

### 3.2 Tight-Binding Model

A tight-binding model (TBM) <sup>4</sup> is an analytical method describing a structure based on the wave function of an electron as a linear combination of atomic orbitals (LCAO) of localized states. It investigates electronic transport properties through the Hamiltonian of a finite set of atomic orbitals. This approach assumes that tightly bound electrons in a molecule form to allow interaction with nearest neighbouring atoms only. Finding the exact solution to the Schrödinger wave equation by the eigenstates and eigenvalues for a system with a small number of electrons such as the hydrogen atom becomes possible by one of the simplest methods of quantum transport modelling utilizes tight-binding models (TBM). When expanding the wavefunction over a finite set of atomic orbitals, the Hamiltonian of the system can be represented in a tight-binding model by using the general solution of the the time-dependent Schrödnger equation as a linear superposition of the form <sup>5</sup>:

$$\Psi(r) = \sum_j \psi_j \phi_j(r) \quad (3.1)$$

where  $\phi_j(r)$  is the eigenfunction on a particular site  $j$ , the wavefunction  $\Psi(r)$  can be represented by a column vector  $|\psi_j\rangle$  consisting of the expansion coefficient  $\psi_j$  and the probability of finding an electron on site  $j$  is  $|\psi_j|^2$ . Hence, the time independent Schrödnger equation can be represented as a square matrix and consist of matrix elements that couple the components of the system together as follow:

$$[H]|\psi\rangle = E[S]|\psi\rangle \quad (3.2)$$

where  $S_{ij} = \langle \phi_j | \phi_i \rangle = \int dr \phi_j^*(r) \phi_i(r)$  and  $\hat{H}_{ij} = \langle \phi_j | \hat{H} | \phi_i \rangle = \int dr \phi_j^*(r) \hat{H} \phi_i(r)$ .

When  $[H]$  and  $[S]$  are acquired by evaluating these integrals, the most time-consuming step can obtain the eigenvalues  $E_j$  and  $\psi_j$  eigenvector are simple to calculate for satisfying  $H|\psi_j\rangle = E_j|\psi_j\rangle$ .

In what follows, I describe models of different structures consisting of the number of atoms, and each atom can possess only a single orbital referring as  $j$  site. This is a simple way to illustrate the general concepts and study the quantum properties of linear chains and ring system. For further simplicity, I shall also assume that atoms interact with nearest neighbour atoms only by considering that all terms  $\langle \phi_j | \hat{H} | \phi_i \rangle$  with  $|i - j| > 1$  are small and can be neglected. Therefore, the time dependent Schrödinger equation for a linear atomic chain within this tight-binding model at site  $j$  is given by:

$$i\hbar \frac{\partial \psi_j}{\partial t} = \varepsilon_j \psi_j - \gamma_j \psi_{j+1} - \gamma_j^* \psi_{j-1} \quad (3.3)$$

where  $\varepsilon_j = H_{jj}$  is the on-site energy of atomic orbital  $j$ , and  $H_{j,j+1} = -\gamma_j$  is the coupling between sites  $j$  and  $j + 1$ .<sup>1,4</sup>

### 3.3 The two-level system

In order to find the eigenvalues and the eigenvectors of a two-level system of the time independent Schrödinger equation (eigenvalue problem)  $H|\psi_j\rangle = E_j|\psi_j\rangle$ , consider a structure consisting of two atoms, and each atom possesses a single atomic orbital. The energy of an electron located on both

atomic orbitals is  $\varepsilon_1, \varepsilon_2$ , respectively. The coupling between the two atoms is denoted  $\Delta$ . Figure 1.3 show the interaction between the two atoms. The Hamiltonian, in this case, is a 2x2 square matrix of the form:

$$H = \begin{pmatrix} \varepsilon & \Delta \\ \Delta^* & -\varepsilon \end{pmatrix} \quad (3.4)$$

where the two on-site atomic energy for each atom could be written as ( $\varepsilon = \frac{\varepsilon_1 - \varepsilon_2}{2}$ ) and the eigenvalues are given by:

$$E = \pm \sqrt{\varepsilon^2 + |\Delta|^2} \quad (3.5)$$

And then the eigenvectors are column vectors with the condition

$$|\psi_1\rangle = \begin{pmatrix} \psi_1^1 \\ \psi_1^2 \end{pmatrix}, |\psi_2\rangle = \begin{pmatrix} \psi_2^1 \\ \psi_2^2 \end{pmatrix}, \frac{\psi_1^1 \psi_1^2}{\psi_2^1 \psi_2^2} = \frac{\Delta}{\pm E - \varepsilon} = \frac{\pm E + \varepsilon}{\Delta^*} \quad (3.6)$$

Figure 3.1 shows the amplitude of the eigenvector obtained numerically by the MATLAB program, and each atom as two circles by a different colour based on the sign and then the radius of the circles represents the magnitude. Two red circles could represent it by  $|\psi_1\rangle = \begin{pmatrix} -0.7 \\ -0.7 \end{pmatrix}$ , and the blue and red circles by  $|\psi_2\rangle = \begin{pmatrix} -0.7 \\ 0.7 \end{pmatrix}$ . These are called the bonding state (symmetric) and the anti-bonding state (antisymmetric), respectively.<sup>1</sup>

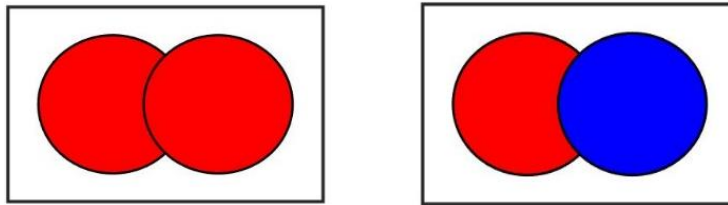


**Figure 3.1.** A representation of a two-level system.

### 3.4 Infinite chain in one dimension

Consider a periodic system of a doubly infinite chain of atoms with one orbital for each atom as shown in Figure 3.2, in which  $\varepsilon_0$  is a single energy level and  $-\gamma$  is the nearest neighbour coupling between each site.

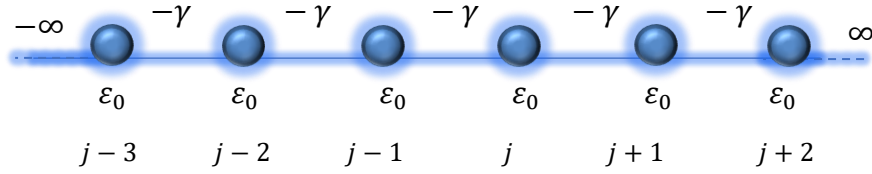


**Figure 3.2.** Tight-binding representation of one-dimensional infinite chain with on-site energies  $\varepsilon_0$  and couplings  $-\gamma$ .

First, the Hamiltonian that takes the form of an infinite matrix, is given by:

$$\begin{pmatrix} -\infty & \cdot \\ \cdot & \cdot \\ \cdot & \cdot & \varepsilon_0 & -\gamma & 0 & 0 & 0 & \cdot & \cdot & \cdot \\ \cdot & \cdot & -\gamma & \varepsilon_0 & -\gamma & 0 & 0 & \cdot & \cdot & \cdot \\ \cdot & \cdot & 0 & -\gamma & \varepsilon_0 & -\gamma & 0 & \cdot & \cdot & \cdot \\ \cdot & \cdot & 0 & 0 & -\gamma & \varepsilon_0 & -\gamma & \cdot & \cdot & \cdot \\ \cdot & \cdot & 0 & 0 & 0 & -\gamma & \varepsilon_0 & \cdot & \cdot & \cdot \\ \cdot & \cdot \\ \cdot & +\infty \end{pmatrix} \begin{pmatrix} \cdot \\ \cdot \\ \psi_{j-1} \\ \psi_j \\ \psi_{j+1} \\ \cdot \\ \cdot \\ \cdot \end{pmatrix} = E \begin{pmatrix} \cdot \\ \cdot \\ \psi_{j-1} \\ \psi_j \\ \psi_{j+1} \\ \cdot \\ \cdot \\ \cdot \end{pmatrix} \quad (3.7)$$

Equivalently,

$$\sum_{l=-\infty}^{\infty} H_{jl} \psi_l = E \psi_j \quad (3.8)$$

According to the time independent Schrödinger equation, the most general formula of the infinite chain is given by:

$$\varepsilon_0 \psi_j - \gamma \psi_{j-1} - \gamma \psi_{j+1} = E \psi_j \quad (3.9)$$

Applying a plane state <sup>6</sup> on Eq. 3.9 to calculate the dispersion relation <sup>7</sup> or (band structure) of this system for the continuous eigenvalues spectrum by substituting  $\psi_j = e^{ikj}$  into equation Eq. 3.9.

Therefore, the eigenvalues  $E(k)$  as a function of  $k$  is:

$$E(k) = \varepsilon_0 - 2\gamma \cos k \quad (3.10)$$

This  $E - k$  relation (dispersion relation) is shown in Figure 3.3 when plotted as a function of  $k$ , and  $k$  is a continuous variable in the range  $-\pi \leq k \leq +\pi$ . The eigenvalues of  $H$  form a continuous band of  $E(k)$  in this range, and the width energy band is proportional to the hopping integral could be written as:

$$E_{min} \leq E \leq E_{max} \quad \text{and} \quad W = E_{min} - E_{max} = 4\gamma \quad (3.11)$$

The linear chain of Figure 3.2 has a single energy band because each unit cell in Figure 3.3 contains only a single atomic orbital.

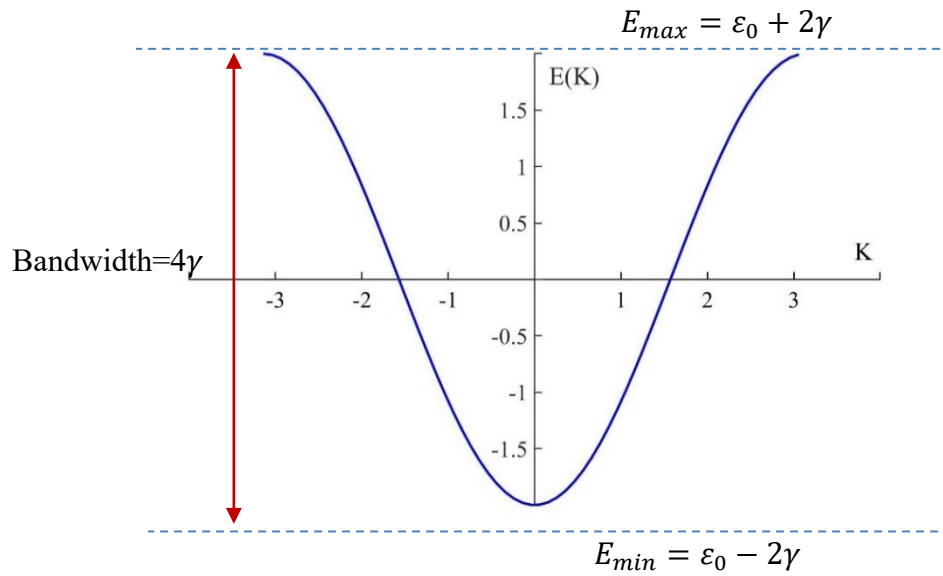


**Figure 3.3.** The dispersion relation of a linear chain.

### 3.5 Periodic chain in one dimension

This system forms a ring where each site or atom has a single atomic orbital, and hopping integrals are  $\epsilon_0$  and  $-\gamma$ , respectively. Figure 3.4 shows that this system possesses periodic boundary conditions when atom  $N$  is the nearest neighbour of atom 1.

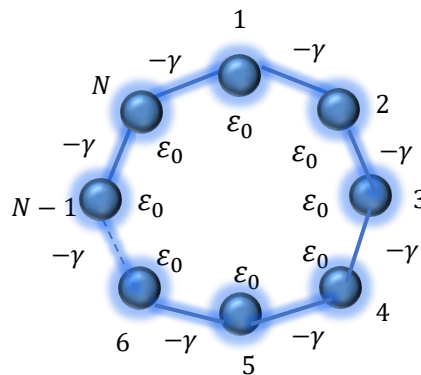


**Figure 3.4.** Tight-binding representation of one-dimensional chain with periodic boundary conditions of on-site energies  $\epsilon_0$  and couplings  $-\gamma$ .

First, the Hamiltonian matrix that takes the form of one-dimensional chain with periodic boundary conditions shown in Figure 3.4, is given by:

$$\begin{pmatrix} \varepsilon_0 & -\gamma & \cdot & -\gamma \\ \cdot & \cdot \\ \cdot & \cdot & \varepsilon_0 & -\gamma & 0 & 0 & 0 & \cdot & \cdot & \cdot \\ \cdot & \cdot & -\gamma & \varepsilon_0 & -\gamma & 0 & 0 & \cdot & \cdot & \cdot \\ \cdot & \cdot & 0 & -\gamma & \varepsilon_0 & -\gamma & 0 & \cdot & \cdot & \cdot \\ \cdot & \cdot & 0 & 0 & -\gamma & \varepsilon_0 & -\gamma & \cdot & \cdot & \cdot \\ \cdot & \cdot & 0 & 0 & 0 & -\gamma & \varepsilon_0 & \cdot & \cdot & \cdot \\ \cdot & \cdot \\ -\gamma & \cdot & \cdot & \cdot & \cdot & \cdot & \cdot & -\gamma & \varepsilon_0 & \cdot \end{pmatrix} \begin{pmatrix} \psi_1 \\ \cdot \\ \cdot \\ \psi_{j-1} \\ \psi_j \\ \psi_{j+1} \\ \cdot \\ \cdot \\ \psi_N \end{pmatrix} = E \begin{pmatrix} \psi_1 \\ \cdot \\ \cdot \\ \psi_{j-1} \\ \psi_j \\ \psi_{j+1} \\ \cdot \\ \cdot \\ \psi_N \end{pmatrix} \quad (3.12)$$

Equivalently,

$$\sum_{l=1}^N H_{jl} \psi_l = E \psi_j \quad (3.13)$$

The tight-binding Hamiltonian is the same as in the linear chain system except that atom 1 become the nearest neighbours of atom  $N$  and can be obtained in the form of these equations:

$$\varepsilon_0 \psi_1 - \gamma \psi_2 - \gamma \psi_N = E \psi_1 \quad (3.14)$$

$$\varepsilon_0 \psi_j - \gamma \psi_{j-1} - \gamma \psi_{j+1} = E \psi_j \quad (3.15)$$

$$\varepsilon_0 \psi_N - \gamma \psi_{N-1} - \gamma \psi_1 = E \psi_N \quad (3.16)$$

This system has the same band structure of the linear chain as in Eq. 3.10 except for the allowed values of  $k$  and still take discrete values. Therefore, the eigenvalue spectrum in a finite system is separate, and, in this case, degeneracies appear (this means the two eigenvectors have the same eigenvalues). The amplitudes of eigenvectors could be calculated in an number of ways (because of the degeneracy in the levels energy system) and the allowed values of  $k$  for each solution. Examples of these solutions are given by <sup>1,5</sup>:

$$\psi_j^n = \frac{1}{\sqrt{N}} e^{i k_n j},$$

$$\text{where } k_n = \frac{2n\pi}{N}, \quad n = 0, 1, 2, 3, \dots, N-1 \quad (3.17)$$

Alternatively, if real states are preferred one can write

$$\psi_j^n = \frac{1}{\sqrt{N}} \cos k_n j \quad \text{where } n = 0, 1, 2, \dots, N \quad (3.18)$$

$$\psi_j^n = \sqrt{\frac{2}{N}} \sin k_n j, \quad \text{where } n = 1, 2, \dots, N-1 \quad (3.19)$$

Figure 3.5 represents a ring system consisting of six atoms, then six eigenvectors and eigenvalues correspond for each atom. Each box shows six values of the amplitude of eigenvectors obtained numerically by the MATLAB program, and each magnitude represents a circle. The blue and red circles are positive and negative amplitude, respectively, where the radius of the ring is proportional to the magnitude of eigenvectors.<sup>1,8,9</sup> As mentioned above, the crucial difference for the ring system compared to the linear chain is that the eigenvalues are degenerate, and therefore there are two degeneracies in this example: between wavefunctions 2 and 3, and between 4 and 5.

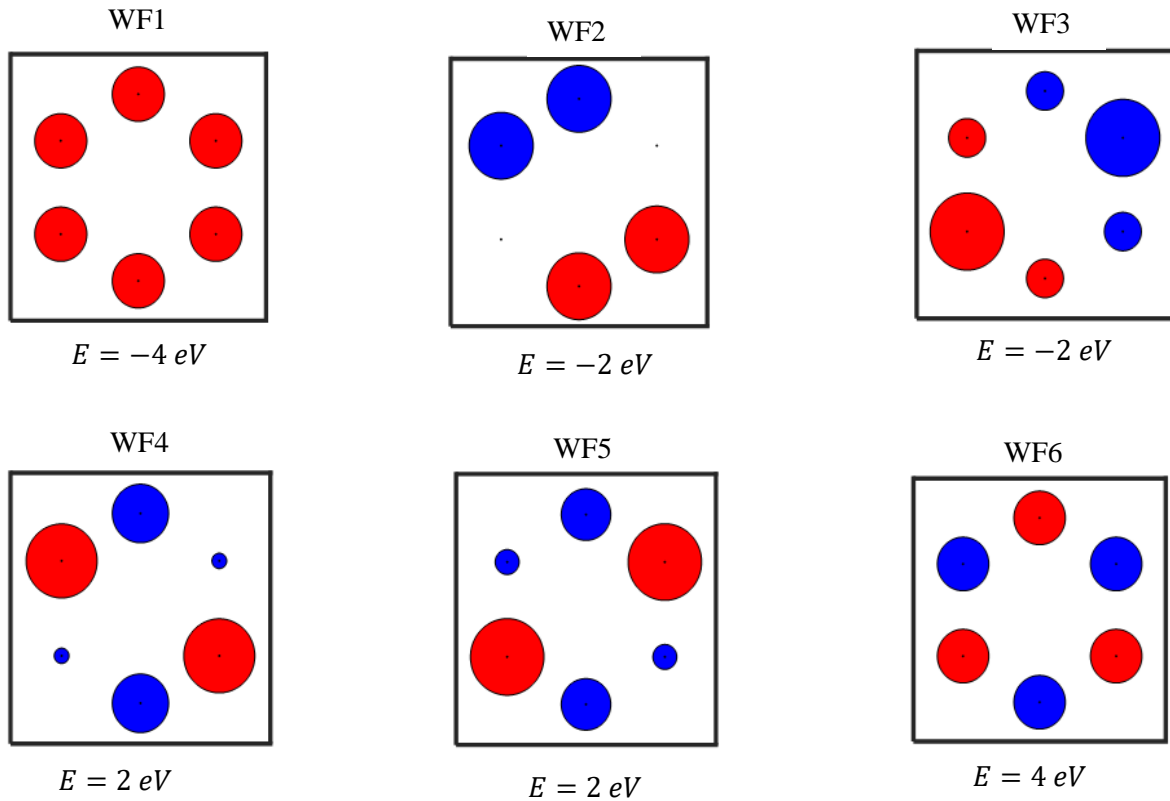


**Figure 3.5.** Wavefunctions of the periodic chain of six sites are obtained numerically, with their energies.

### 3.6 Bond current

In order to obtain the definition of the bond current between different sites using the time dependent Schrödinger equation and introduce tight binding description of a quantum system, consider the one-dimensional infinite chain as shown in Figure 3.6, in which all site energies  $\varepsilon_j$  and all bonds  $-\gamma_j$  are arbitrary. The time dependent Schrödinger equation for this system is:

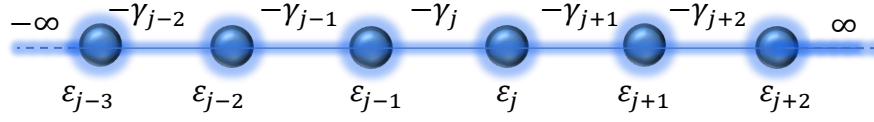


**Figure 3.6.** Tight-binding representation of one-dimensional chain in which all site energies  $\varepsilon_j$  and all bonds  $-\gamma_j$  are arbitrary.

$$i\hbar \frac{\partial}{\partial t} |\psi(t)\rangle = H|\psi(t)\rangle \quad (3.20)$$

or equivalently in terms of Hamiltonian matrix elements,  $\varepsilon_j = H_{jj}$  and  $H_{j,j+1} = -\gamma_j$

$$i\hbar \frac{\partial}{\partial t} \psi(t) = \varepsilon_j \psi_j(t) + H_{j,j-1} \psi_{j-1}(t) + H_{j,j+1} \psi_{j+1}(t) \quad (3.21)$$

By choosing a particular site  $j$  at time  $t$ , the probability for finding an electron on this site is

$$P_j(t) = |\psi_j(t)|^2 = \psi_j(t) \psi_j^*(t) \quad (3.22)$$

Where  $P_j$  is the average number of electrons on site  $j$ . To obtain an expression for the change in occupation probability on-site  $j$  with  $t$  as:

$$i\hbar \frac{\partial}{\partial t} P_j(t) = i\hbar [\psi_j(t) \frac{\partial}{\partial t} \psi_j^*(t) + \psi_j^*(t) \frac{\partial}{\partial t} \psi_j(t)] \quad (3.23)$$

After applying the complex conjugate of the Eq.3.17, which is

$$i\hbar \frac{\partial}{\partial t} \psi_j^*(t) = -[\varepsilon_j \psi_j^*(t) + H_{j,j-1}^* \psi_{j-1}^*(t) + H_{j,j+1}^* \psi_{j+1}^*(t)] \quad (3.24)$$

Hence, the change in  $P_j(t)$  is equal the different between the current into site  $j$  and the current out of site  $j$  as:

$$\frac{\partial}{\partial t} P_j(t) = \frac{i}{\hbar} \left\{ \underbrace{\left[ H_{j,j-1}^* \psi_j(t) \psi_{j-1}^*(t) - H_{j,j-1} \psi_j^*(t) \psi_{j-1}(t) \right]}_{I_{j-1 \rightarrow j}} - \underbrace{\left[ H_{j,j+1} \psi_j^*(t) \psi_{j+1}(t) - H_{j,j+1}^* \psi_j(t) \psi_{j+1}^*(t) \right]}_{I_{j \rightarrow j+1}} \right\} \quad (3.25)$$

or equivalently

$$\frac{\partial}{\partial t} P_j(t) = I_{j-1 \rightarrow j} - I_{j \rightarrow j+1} \quad (3.26)$$

where  $I_{j-1 \rightarrow j}$  is the bond current from site  $j - 1$  to site  $j$ , and  $I_{j \rightarrow j+1}$  is the bond current from site  $j$  to site  $j + 1$ , and therefore  $P_j(t)$  cannot be destroyed; it can flow from one site to its neighbours (law of conservation of probability). Where the current passing through the bond  $I_{j-1 \rightarrow j}$  at the case  $H_{j,j-1}^* = H_{j-1,j}$  can be written:

$$I_{j-1 \rightarrow j} = \frac{i}{\hbar} \left[ H_{j-1,j} \psi_j(t) \psi_{j-1}^*(t) - H_{j-1,j}^* \psi_j^*(t) \psi_{j-1}(t) \right] \quad (3.27)$$

And the current passing through the bond  $I_{j \rightarrow j+1}$  at the case  $H_{j,j+1} = -\gamma_j$ :

$$I_{j \rightarrow j+1} = \frac{i}{\hbar} \left[ -\gamma_j \psi_j^*(t) \psi_{j+1}(t) - \gamma_j^* \psi_j(t) \psi_{j+1}^*(t) \right] \quad (3.28)$$

Hence,

$$I_{j \rightarrow j+1} = \frac{2\gamma_j}{\hbar} \text{Im}[\psi_j(t) \psi_{j+1}^*(t)] \quad (3.29)$$

Therefore, if  $\psi_j(t)$  is an eigenstate of Hamiltonian of the one-dimensional chain shown in Figure 3.2 where for all  $j$ ,  $\varepsilon_j = \varepsilon_0$  and  $-\gamma_j = -\gamma$ , the plane wave of the system is  $\psi_j = Ae^{ikj}$ . In this case,  $\psi_j^*(t)\psi_{j+1} = |A|^2e^{ik}$  and then  $Im[\psi_j\psi_{j+1}^*] = |A|^2\sin k$ . That means that all bond currents carried by this plane wave are equal and the current entering any site is equal to the current leaving the site,  $\frac{\partial}{\partial t}P_j(t) = 0$ . Hence from Eq.3.29, the bond current that is carried by this plane wave of amplitude  $A$  is:

$$I_{j \rightarrow j+1} = \frac{2\gamma\sin k}{\hbar} |A|^2 = v_k |A|^2, \quad (3.30)$$

$$v_k = \frac{1}{\hbar} \frac{\partial E}{\partial k}, \quad E(k) = \varepsilon_0 - 2\gamma\cos k$$

where  $v_k$  is the group velocity of the plane wave  $e^{ikj}$ , and  $E(k)$  is the dispersion relation shown in Figure 3.3. Hence, the plane wave  $e^{ikj}$  is often normalized with its current flux  $\frac{1}{\sqrt{v_k}}$  to obtain a unit current, and therefore this state can be written as <sup>1,4,8</sup>

$$\psi_j = \frac{e^{ikj}}{\sqrt{v_k}} \quad (3.31)$$

### 3.7 Scattering theory of transport in one-dimension

One of the definitions of scattering theory results from the electrons flow process passing through the scattering region from one electrode to the other, which are modelled as semi-infinite crystalline leads. A significant scattering occurs inside the scattering region containing the molecule and nearby surfaces of the electrodes or through nano and molecular scale junctions. In contrast, the electrodes configure and convey electrons by perfect waveguides without any scattering. This process could be understood by introducing the Schrödinger equation for the simplest problem of a single impurity placed between two semi-infinite one-dimensional crystals. This will introduce the idea of a scattering matrix and an approach for predicting the electrical conductance by the Landauer formalism.<sup>8,10,11</sup>

### 3.8 A single impurity in one dimension.

Consider where the perturbation to the doubly infinite chain is just a single impurity  $f_0$  at site  $j = 0$  with energy  $\varepsilon_1$  with the coupling between each two neighbouring atoms is  $(-\gamma)$  as shown in Figure 3.7.

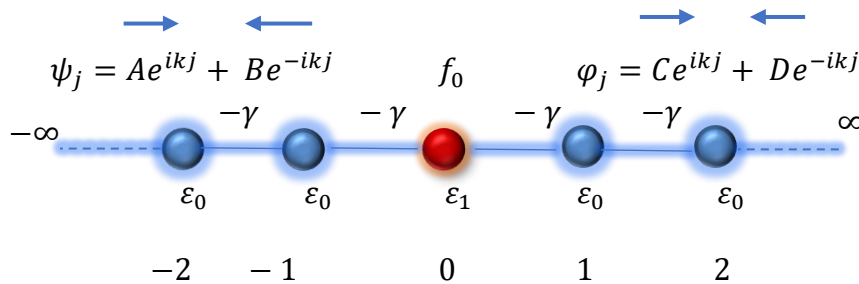


**Figure 3.7.** Tight-binding representation of a doubly infinite chain containing a single impurity at site  $j = 0$ .

Assuming the two amplitude of the plane waves, which one of them is travelling from left to right, towards the impurity  $f_0$  while the other is moving outwards from the impurity  $f_0$  are  $\psi_j = Ae^{ikj} + Be^{-ikj}$  and  $\varphi_j = Ce^{ikj} + De^{-ikj}$ , respectively, where  $A, B, C, D$  are constants.

Therefore, the solution to the tight-binding Hamiltonian of the left of the impurity  $f_0$  at ( $j < -1$ ) is  $\psi_j = Ae^{ikj} + Be^{-ikj}$  where the right of the impurity  $f_0$  is  $\varphi_j = Ce^{ikj} + De^{-ikj}$  at ( $j > 1$ ).

Then the tight-binding Hamiltonian at ( $j < -1$ ) could be written for  $j = -1$  as:

$$\varepsilon_0\psi_{-1} - \gamma\psi_{-2} - \gamma\psi_0 = E\psi_{-1} \quad (3.32)$$

Comparing Eq.3.32 with Eq.3.33

$$\varepsilon_0\psi_{-1} - \gamma\psi_{-2} - \gamma f_0 = E\psi_{-1} \quad (3.33)$$

Hence,  $f_0 = \psi_0 = A + B$ , and similarly for the amplitude of the plane wave  $\varphi_j$  for  $j = 1$ :

$$\varepsilon_0\psi_{-1} - \gamma\psi_{-2} - \gamma\psi_0 = E\psi_{-1} \quad (3.34)$$

Comparing Eq.3.34 with Eq.3.35

$$\varepsilon_0 \varphi_1 - \gamma f_0 - \gamma \varphi_2 = E \varphi_1 \quad (3.35)$$

And yield,  $f_0 = \psi_0 = C + D$ .

Since ( $A + B = C + D$ ), this allows us to write the solution as:

$$\begin{aligned} \varepsilon_1\psi_0 - \gamma\psi_{-1} - \gamma\varphi_1 &= E\psi_0 \\ \varepsilon_0\psi_0 - \gamma\psi_{-1} - \gamma\psi_1 &= E\psi_0 \end{aligned} \quad (3.36)$$

$$\varphi_1 = \frac{(\varepsilon_1 - \varepsilon_0)}{\gamma} \psi_0 + \psi_1$$

This system has the same band structure of the Infinite linear chain as in equation  $E(k) = \varepsilon_0 - 2\gamma \cos k$ .

In what follow, it is helpful to introduce the idea of a scattering matrix using the general solution (the linear superposition of two plane waves) to the Schrödinger equation of a single impurity problem. Hence, this solution contains most two arbitrary constants. Thus, if any two constants,  $A, B, C$  and  $D$ , are known, then the other two constants are determined.

### 3.9 Scattering matrix

Assuming the current in the left lead is  $I_{Left} = |A|^2 - |B|^2$  and the current in the right lead is  $I_{Right} = |C|^2 - |D|^2$ . Conservation of probability requires such an eigenstate  $|A|^2 - |B|^2 = |C|^2 - |D|^2$  as shown in Figure 3.7.

Equivalently  $I_{Left} = I_{Right}$ , the incoming current from both leads is  $|A|^2 + |D|^2$  and the outgoing current into both leads is  $|B|^2 + |C|^2$  and therefore,  $|A|^2 + |D|^2 = |B|^2 + |C|^2$ . Since the plane wave is normalized to unit current as Eq. 3.31, it can be written as a solution of the time independent Schrödinger equation for the electron behaving from the left lead by

$$\psi_j = A \frac{e^{ik_l j}}{\sqrt{v_l}} + B \frac{e^{-ik_l j}}{\sqrt{v_l}} \quad \text{where } I_{Left} = |A|^2 - |B|^2 \quad (3.37)$$

And for the electron behave from the right lead by

$$\varphi_j = C \frac{e^{ik_R j}}{\sqrt{v_R}} + D \frac{e^{-ik_R j}}{\sqrt{v_R}} \quad \text{where } I_{Right} = |C|^2 - |D|^2 \quad (3.38)$$

Therefore, the scattering region can be described as a matrix based on the relationship between these constants  $A, B, C, D$  as:

$$\begin{pmatrix} B^* & C^* \end{pmatrix} \begin{pmatrix} B \\ C \end{pmatrix} = \begin{pmatrix} A^* & D^* \end{pmatrix} \begin{pmatrix} A \\ D \end{pmatrix} \quad (3.39)$$

Hence, the scattering matrix for the system is defined to satisfy:  $\begin{pmatrix} B \\ C \end{pmatrix} S = \begin{pmatrix} A \\ D \end{pmatrix}$  and by applying the Hermitian conjugate yields  $\begin{pmatrix} B^* & C^* \end{pmatrix} = \begin{pmatrix} A^* & D^* \end{pmatrix} S^\dagger$ . Hence, substituting these into Eq.3.39 yields <sup>1,12</sup>:

$$\begin{pmatrix} A^* & D^* \end{pmatrix} S^\dagger S \begin{pmatrix} A \\ D \end{pmatrix} = \begin{pmatrix} A^* & D^* \end{pmatrix} \begin{pmatrix} A \\ D \end{pmatrix} \quad (3.40)$$

Therefore, the  $S$  matrix is a major concept of scattering theory and conservation of charge, which implies the scattering matrix to be unitary as  $SS^\dagger = 1$  <sup>13</sup>. Hence, the scattering matrix elements are:

$$\begin{pmatrix} B \\ C \end{pmatrix} \begin{pmatrix} S_{11} & S_{12} \\ S_{21} & S_{22} \end{pmatrix} = \begin{pmatrix} A \\ D \end{pmatrix} \quad (3.41)$$

$$S = \begin{pmatrix} S_{11} & S_{12} \\ S_{21} & S_{22} \end{pmatrix} = \begin{pmatrix} r & t' \\ t & r' \end{pmatrix} \quad (3.42)$$

Hence, the physical meaning of  $S_{11} = r$ , is that the reflection amplitude associated with an incoming plane wave from the left and similarly,  $S_{21} = t$ , is the corresponding transmission amplitude from the left. In addition,  $S_{22} = r'$ , is that the reflection amplitude associated with an incoming plane wave from the right and  $S_{12} = t'$ , is the corresponding amplitude of transmission wave from right to left lead. As consequences of unitarity of the scattering matrix  $SS^\dagger = 1$ .<sup>14</sup>

Hence

$$\begin{pmatrix} 1 & 0 \\ 0 & 1 \end{pmatrix} = SS^\dagger = \begin{pmatrix} r^* & t^* \\ t'^* & r'^* \end{pmatrix} \begin{pmatrix} r & t \\ t' & r' \end{pmatrix} \quad (3.43)$$

By multiplication of the matrix, Hence  $r^*r' + t^*t = 1$ , and then  $r^*r = r'^*r'$  and  $t^*t = t'^*t'$ . Hence, the reflection and transmission coefficients due to an incoming plane wave from the right and the left, respectively, are

$$R(E) = r^*r \text{ and } T(E) = t^*t \quad (3.44)$$

$$R'(E) = r'^*r' \text{ and } T'(E) = t'^*t'$$

$$R(E) = R'(E) \text{ and } T'(E) = T(E)$$

From the result  $r^*r' + t^*t = 1$ , Hence

$$R(E) + T(E) = 1 \quad (3.45)$$

The transmission coefficient  $T(E)$  is the transmitted current in the right lead, per unit incident current in the left lead and  $R(E)$  is the reflected current in the right lead, per unit incident current in the left lead.<sup>1,11</sup>

A study scattering theory in nano and molecular scale junctions helps calculate the transmission probability  $T(E)$  of the electron energy when passing from the left lead to the right lead. It allows predicting through the electron's transport property the electrical conductance of a scattered connected to two leads via the Landauer formula as the following section.

### 3.9 Landauer Formula

Landauer Formula is the classic theoretical model for describing phase-coherent, ballistic transport regime.<sup>15</sup> This is the most widely used formula to describe coherent transport in nanoscale devices. The fundamental assumption behind this method is used the scattering theory of transport as a conceptual framework to define the electrical conductance and wrote conductance is transmission.<sup>4</sup> As a result, this system transport can be described as a quantum mechanical scattering problem consisting of a scatterer connected to reservoirs via perfect quantum wires or electrodes that act as waveguides for electrons flow.<sup>16</sup> The following section gives an overview of this theory.

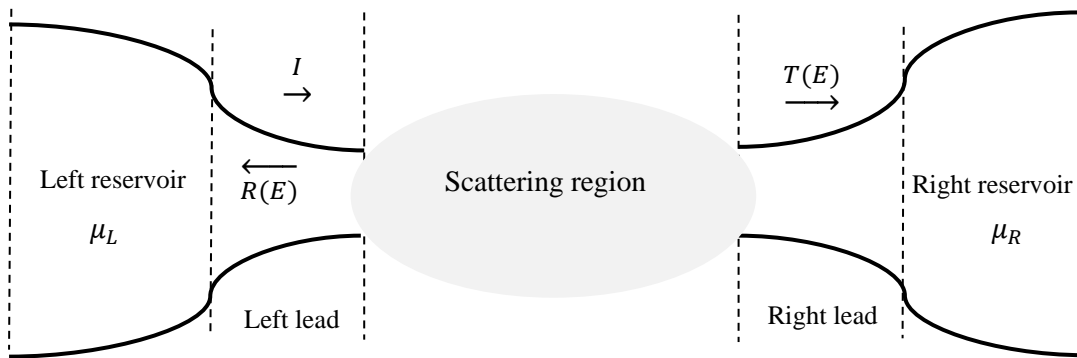


**Figure 3.8.** A scattering region (molecule) placed between two leads connecting two reservoirs with different chemical potentials  $\mu_L$  and  $\mu_R$ . When an incident wave strikes  $I$  with the scatterer from the left, the wave will be transmitted to the right with probability  $T = |\vec{t}|^2$  and then reflected with probability  $R = |\vec{r}|^2$ . Therefore, the incident electrons essential be either reflected or transmitted for the probability conservation is  $T + R = 1$  as Eq. 3.45.

Figure 3.8 shows a scatterer is attached to two leads as coherent system in which electrons in the leads are transmitted in a ballistic way, and therefore no energy is lost in this area. Then, the leads are connected to two reservoirs with different chemical potentials,  $\mu_L$  and  $\mu_R$ , to drive electrons from the left lead to the right lead. The two reservoirs are connected to a source and drain through contact points, and a small voltage is applied, resulting in  $eV = \mu_L - \mu_R$ , which is the difference between the two Fermi levels. Then the conductance of this system can be written as <sup>16-18</sup>:

$$G = \frac{I}{V} = \frac{eI}{\mu_L - \mu_R} \quad (3.46)$$

In what follows, I derive the Landauer formula, which allows us to calculate the current in Eq.3.46. A derivation of the Landauer formula for a structure connected to one-dimensional leads is based on the idea of a perfect reservoir, which can be used to deliver electrons to a scattering region. To define a perfect reservoir, consider the one-dimensional ring of  $N$  sites with periodic boundary conditions when atom  $N$  is the nearest neighbour of atom 1, as shown in Figure 3.4. The eigenstate for this model is  $\psi_j^n = \frac{1}{\sqrt{N}} e^{ik_n j}$  in the energy interval  $E + \Delta E$ , where  $k_n = \frac{2n\pi}{N}$ , then  $\Delta n = \frac{N}{hv_k} \Delta E$  where  $hv_k = \frac{\partial E}{\partial k}$ , therefore, the number of states with positive group velocity per unit energy is.<sup>1,19</sup>

$$\frac{\Delta n}{\Delta E} = \frac{N}{hv_k} \quad (3.47)$$

Therefore, the current passing through an arbitrary site in the energy interval  $\Delta E$  per one electron is  $\Delta I = \frac{1}{h} \Delta E$ , while each state that contains two electrons of opposite spin is

$$\Delta I = \frac{2}{h} \Delta E \quad (3.48)$$

By finding the two ideal reservoirs on the left and right of a scatterer, they fill all right-moving states and left-moving states with an occupancy determined by the Fermi function  $f_{Left}(E)$  of the left lead the Fermi function  $f_{Right}(E)$  of the right lead.

The number of electrons sent from the left and right reservoirs is  $\Delta I^{Left} = \frac{2}{h} f_{Left}(E)\Delta E$  and  $\Delta I^{Right} = \frac{2}{h} f_{Right}(E)\Delta E$  respectively. As shown in Figure 3.8, the current from the left reservoir can transmit into the right lead through the scattering region and the current from the right reservoir can reflect into the right lead. Hence, the net electron current in the right lead is <sup>1,8,20</sup>:

$$\Delta I = T(E)\Delta I^{Left} - (1 - R(E))\Delta I^{Right} = \frac{2}{h} [f_{Left}(E)\Delta E - f_{Right}(E)\Delta E] \quad (3.49)$$

In the case of  $R(E) + T(E) = 1$ , Hence

$$\Delta I = \frac{2}{h} T(E)\Delta E [f_{Left}(E) - f_{Right}(E)] \quad (3.50)$$

where  $T(E)$  is transmission function of the electron energy is a property of the whole system, which involves the isolated molecule, leads and the contact between the leads and the molecule which have Fermi distribution  $f(E)$  at the chemical potentials  $\mu_L$  and  $\mu_R$  entering the left (right) gold lead from the left (right) reservoir as:

$$f_{Left}(E) = \frac{1}{(1 + e^{(E-E_F^{Left})/k_B T})}, \quad (3.51)$$

$$f_{Right}(E) = \frac{1}{(1 + e^{(E-E_F^{Right})/k_B T})}$$

where  $k_B$  is Boltzmann constant,  $T$  is the temperature and  $E_F^{Left} = \mu_{L(R)}$  and  $E_F^{Right} = \mu_{R(L)}$ , which are the chemical potential of the left (right) or of the right (left) reservoir, respectively. After integrating overall energies. Hence

$$I = \frac{2e}{h} \int_{-\infty}^{+\infty} dE T(E) [f_{Left}(E) - f_{Right}(E)] \quad (3.52)$$

Where  $e = -|e|$  is the electronic charge value. When setting the voltage difference  $V$  between the left and right reservoirs to be  $E_F^{Left} = E_F + \frac{eV}{2}$  and  $E_F^{Right} = E_F - \frac{eV}{2}$ , this means at  $T = 0K$  and finite voltage, the current in Landauer description.

$$I = \frac{2e}{h} \int_{E_F - \frac{eV}{2}}^{E_F + \frac{eV}{2}} dE T(E) \quad (3.53)$$

Consequently, the conductance with finite temperature limit and the zero voltage is

$$G = \frac{I}{V} = G_0 \int_{-\infty}^{+\infty} dE T(E) \left( \frac{-\partial f(E)}{\partial E} \right)_{\mu=E_F} \quad (3.54)$$

Therefore the Landauer formula constitutes the conductance  $G$  proportional to the transmission coefficient evaluated at the Fermi energy in units of  $\frac{2e^2}{h}$  as:

$$G(E_F) = G_0 T(E_F) \quad (3.55)$$

where  $G_0$  is a conductance quantum unit and given by  $\frac{2e^2}{h} = 77 \mu Siemens$ , where  $e$  is the electron charge and  $h$  is the Planck constant.<sup>1,21</sup>

### 3.10 Transmission coefficient of an arbitrary scatterer

In order to find the most general equation to calculate the transmission coefficient for any arbitrary scatterer region connected to one-dimensional different leads. Consider electron transport through a double infinite chain has an arbitrary scattering region which involves finite chain containing  $N$  sites, whose wave function consists of an incoming wave of unit current from the left by  $V_L$  and  $V_R$ , which are the group velocities in the left and right lead, respectively.<sup>22</sup> Hence, the reflected and transmitted waves which is given as Figure 3.9.

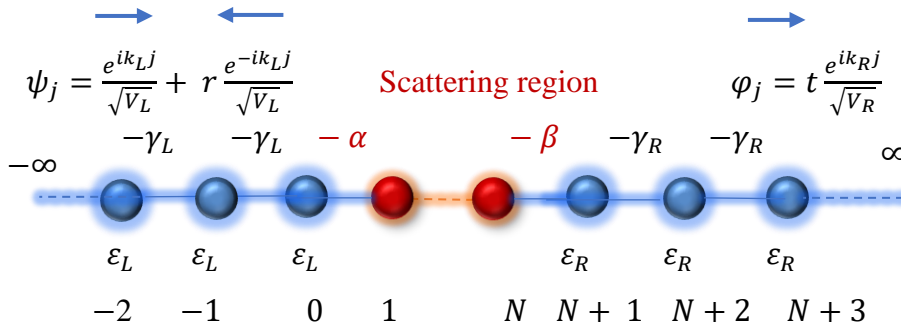


**Figure 3.9.** Tight-binding model of one-dimensional double-infinite chain with an arbitrary scattering region.

Then the wavefunctions in the left and right lead are:  $\psi_j = \frac{e^{ik_L j}}{\sqrt{V_L}} + r \frac{e^{-ik_L j}}{\sqrt{V_L}}$  and  $\varphi_j = t \frac{e^{ik_R j}}{\sqrt{V_R}}$  respectively and the wave function in the scattering region will be denoted  $f_j$  where  $-\alpha$  and  $-\beta$  are the hopping elements connected between the scattering region to site 1 of the left and site  $N$  of the right lead. Therefore, the Schrödinger equation for this structure is

$$j \leq -1 \quad \varepsilon_l \psi_j - \gamma_l \psi_{j-1} - \gamma_l \psi_{j+1} = E \psi_j \quad (3.56)$$

$$j = 0 \quad \varepsilon_l \psi_0 - \gamma_l \psi_{-1} - \alpha f_1 = E \psi_0 \quad (3.57)$$

For the scattering region:

$$j = 1 \quad \sum_{l=1}^N H_{1l} f_l - \alpha \psi_0 = E f_1 \quad (3.58)$$

$$2 \leq j \leq N - 1 \quad \sum_{l=1}^N H_{jl} f_l = E f_j \quad (3.59)$$

$$j = N \quad \sum_{l=1}^N H_{Nl} f_l - \beta \varphi_{N+1} = E f_N \quad (3.60)$$

$$j = N + 1 \quad \varepsilon_l \varphi_{N+1} - \beta f_N - \gamma_R \varphi_{N+2} = E \varphi_{N+1} \quad (3.61)$$

$$j \geq N + 2 \quad \varepsilon_l \varphi_j - \gamma_R \varphi_{j-1} - \gamma_R \varphi_{j+1} = E \varphi_j \quad (3.62)$$

Substituting  $\psi_j = \frac{e^{ik_L j}}{\sqrt{V_L}} + r \frac{e^{-ik_L j}}{\sqrt{V_L}}$  into Eq. 3.57 yields

$$\gamma_L \psi_1 = \alpha f_1 \quad (3.63)$$

And substituting  $\varphi_j = t \frac{e^{ik_R j}}{\sqrt{V_R}}$  into Eq. 3.60 yields

$$\gamma_R \varphi_N = \beta f_N \quad (3.64)$$

Therefore, these two Eq.3.60 and Eq.3.64 relate the wave function on the inside of the scatterer to the wave function on the outside.<sup>1</sup> Then based on Eq.3.58 and 3.60 can be written as

$$(E - h) \begin{pmatrix} f_1 \\ \vdots \\ f_N \end{pmatrix} = \begin{pmatrix} -\alpha \psi_0 \\ \vdots \\ -\beta \varphi_{N+1} \end{pmatrix} \quad (3.65)$$

Multiplying both sides of Eq.3.65 by the inverse matrix  $(E - h)^{-1}$  yields

$$\begin{pmatrix} f_1 \\ \vdots \\ f_N \end{pmatrix} = g \begin{pmatrix} -\alpha\psi_0 \\ \vdots \\ -\beta\varphi_{N+1} \end{pmatrix} \quad (3.66)$$

where  $g = (E - h)^{-1} = \begin{pmatrix} g_{11} & \cdots & g_{1N} \\ \vdots & \ddots & \vdots \\ g_{N1} & \cdots & g_{NN} \end{pmatrix}$  and can be written  $\hat{g}$  as the  $2 \times 2$  sub-matrix, which

is called the Green's function of the isolated scattered region <sup>1,23</sup>, then  $\hat{g} = \begin{pmatrix} g_{11} & g_{1N} \\ g_{N1} & g_{NN} \end{pmatrix}$ , and this

yields

$$\begin{pmatrix} -\alpha\psi_0 \\ -\beta\varphi_{N+1} \end{pmatrix} = \hat{g}^{-1} \begin{pmatrix} f_1 \\ f_N \end{pmatrix} \quad (3.67)$$

By solving  $d = \det \hat{g} = g_{11} g_{NN} - g_{1N} g_{N1}$  based on Eq.3.67 using the most general solution for the system  $\psi_j = \frac{e^{ik_L j}}{\sqrt{V_L}} + r \frac{e^{-ik_L j}}{\sqrt{V_L}}$  and  $\varphi_j = t \frac{e^{ik_R j}}{\sqrt{V_R}}$  and making many measurements to obtain the formula for the transmission coefficient of an arbitrary scatterer connected to one-dimensional leads <sup>1</sup> in terms of the Green's function as:

$$T(E) = |t|^2 = 4 \left[ \left( \frac{\alpha^2}{\gamma_L} \sin(k_L) \right) \left( \frac{\beta^2}{\gamma_R} \sin(k_R) \right) \right] \left| \frac{g_{1N}}{\Delta} \right|^2 \quad (3.68)$$

$\Delta$  is given by ( $\Delta = 1 + x$ ), and  $x$  is given by

$$\begin{aligned} x = & \left( \frac{\alpha^2}{\gamma_L} e^{ik_L} g_{11} \right) + \left( \frac{\beta^2}{\gamma_R} e^{ik_R} g_{NN} \right) \\ & + \left( \frac{\alpha^2 \beta^2}{\gamma_L \gamma_R} e^{i(k_L + k_R)} (g_{11} g_{NN} - g_{1N} g_{N1}) \right) \end{aligned} \quad (3.69)$$

Where the wave vectors  $k_L$  and  $k_R$  of the left and right lead which be obtained as:

$$k_L(E) = \cos^{-1}\left(\frac{\varepsilon_0 - E}{2\gamma_L}\right) \quad \text{and} \quad k_R(E) = \cos^{-1}\left(\frac{\varepsilon_0 - E}{2\gamma_R}\right) \quad (3.70)$$

$g_{11}, g_{NN}, g_{1N}, g_{N1}$  are the elements of the sub-matrix of  $g_{ij}(E)$  and is called the Green's function of the isolated scattered region. The Green's function of a close system defines as the inverse of the Schrödinger equation  $[(E - H) g_{ij}(E) = I]$  and could be written in the form of  $G(E) = (E - H)^{-1}$ . From the time-independent Schrödinger equation, the eigenstates  $|\psi_n\rangle$  satisfy the completeness condition  $\sum_{n=1}^N |\psi_n\rangle\langle\psi_n| = I$ ; therefore, the Green's function becomes

$$G(E) = \sum_{n=1}^N (E - H)^{-1} |\psi_n\rangle\langle\psi_n| \quad (3.71)$$

Consequently, the Hamiltonian operator acting on an eigenvector gives the same wave function of the corresponding eigenvalue  $E_n$ . Hence the components of  $G(E)$  satisfy

$$g_{ij}(E) = \sum_{n=1}^N \frac{|\psi_i^n\rangle\langle\psi_j^n|}{(E - E_n)} \quad (3.72)$$

where  $(\psi_i^n)$  and  $(\psi_j^n)$  are the amplitudes of the eigenstates of the isolated scatterer on sites  $i$  and  $j$  respectively, corresponding to eigenvalue  $E_n$ . Therefore, Eq. 3.72 leads to a reasonable approximation to describe the Green's function<sup>1</sup> of a close system. When  $E$  is close to an eigenvalue  $E_n$ , then the terms  $x$  in Eq.3.68 becomes very large, even in the weak coupling limit (where the coupling of the isolated scatterer to the leads  $\alpha$  and  $\beta$  are small), because  $g_{11}, g_{NN}, g_{1N}, g_{N1}$  diverge. As a result, the transmission coefficient  $T(E)$  is proportional to the element  $\left|\frac{g_{1N}}{\Delta}\right|^2$  in Eq.3.68 of the Green's function of a close system, then  $T(E)$  will possess a series of peaks (resonant transport) located at energies close to  $E_n$  levels, and the transmission is a maximum. In addition, the width of each resonance can be determined by the imaginary part of the self-energy

( $\Gamma$ ) while the peaks shifted slightly by the real part ( $\sigma$ ) as in Eq. 3.73, in the case of the left side, by the form:

$$\begin{aligned}\Sigma_L &= -\frac{\alpha^2}{\gamma_L} e^{ik_L} g_{11} & (3.73) \\ &= \left( -\frac{\alpha^2}{\gamma_L} g_{11} \cos(k_L) \right) - i \left( -\frac{\alpha^2}{\gamma_L} g_{11} \sin(k_L) \right)\end{aligned}$$

or equivalently:

$$\Sigma_L = \sigma_L - i \Gamma_L \quad (3.74)$$

Consequently, the various properties of the formula of the transmission coefficient of an arbitrary scatterer connected to one-dimensional leads in terms of the Green's function as described in Eq.3.72 demonstrate how it leads to the on-resonant transport described by the Breit–Wigner formula and different aspects of quantum interference in coupled structures.<sup>1</sup>

### 3.11 Generic features of the Transmission curve

Interest in molecular-scale transport has prompted many studies on the quantum interference phenomena and its effects on transport and thermoelectric properties. These quantum interference effects are exhibited as on-resonance (Breit–Wigner resonance) and anti-resonances in transport curves. Thus, For a broad understanding of these critical features, the following section will introduce a brief study based on the formula for the transmission coefficient of an arbitrary scatterer connected to one-dimensional leads.<sup>1,8</sup>

### 3.11.1 Breit–Wigner formula (BWF)

Breit-Wigner formula describes the transmission coefficient  $T(E)$  through a system simplified to a single peak form when the energy  $E$  of the electron is close to an eigenenergy  $E_n$  of the isolated scatterer. This resonant condition ( $E$  close to  $E_n$ ) is a consequence of quantum interference, which could be determined as the two simplest descriptions of constructive and destructive interference. By substituting Eq. 3.72 of the Green's function into Eq.3.68 to express the Breit-Wigner formula (BWF) as:

$$T(E) = \frac{4\Gamma_L \Gamma_R}{(E - \tilde{E}_n)^2 + (\Gamma_L + \Gamma_R)^2} \quad (3.75)$$

where  $\tilde{E}_n = (E_n - \sigma)$  and  $\sigma = \sigma_L + \sigma_R$ . If  $E = \tilde{E}_n$ , the transmission coefficient reaches a maximum value  $T(E)$  and transport is said to be on resonance. In addition, the coupling of the isolated scatterer to the leads is ( $\Gamma_L = \Gamma_R$ ), the transmission coefficient is a maximum ( $T_{max} = 1$ ) in the case of the non-degenerate closed system or identical leads. On the other hand, in the case ( $\Gamma_L \neq \Gamma_R$ ), the maximum value of the transmission coefficient is less than unity and given by  $\frac{4\Gamma_R}{\Gamma_L} \ll 1$ . It is worth noting that the energetic location of the resonance is not equal to the eigenenergy  $E_n$  of the isolated scatterer. Instead, it is shifted slightly by  $\sigma$  (the real part of the self-energy), in which the imaginary part of the self-energy ( $\Gamma_L + \Gamma_R$ ) control the width of the peak as Eq.3.74. As resulting in Breit-Wigner resonances, the transmission coefficient of asymmetric junctions is lower than that of symmetric junctions.

An example of a three-level system is shown in Figure 3.10. Some features are shown in the middle peak such as narrow resonance arising in the scatterer which is weakly coupled to the leads.<sup>1,24</sup>

Consequently, each resonance could be well described by such a Breit–Wigner formula as a phenomenon of constructive quantum interference (CQI).

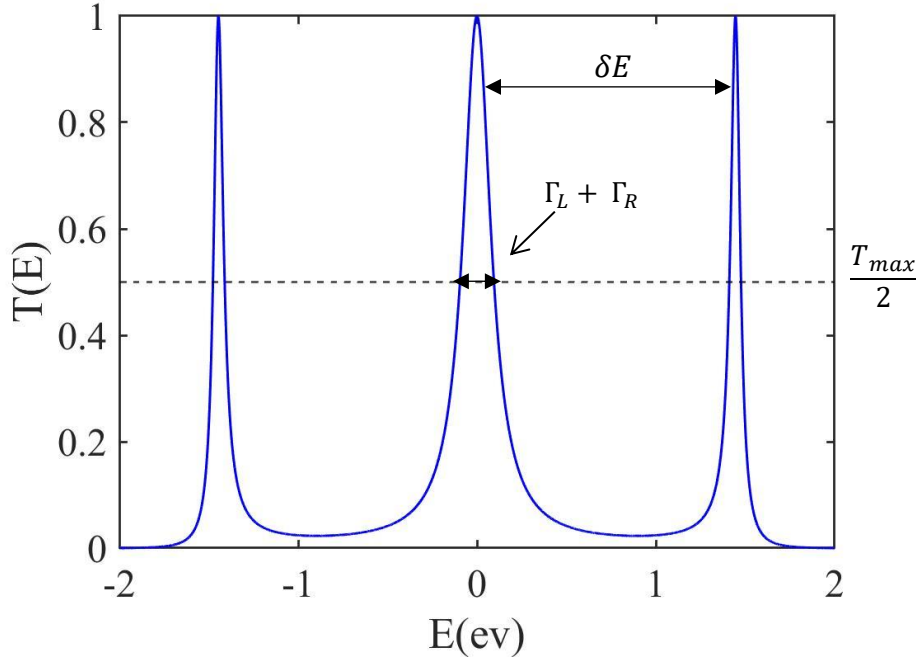


**Figure 3.10.** The transmission coefficients  $T(E)$  of three levels system demonstrate a Breit–Wigner resonance: where the level broadening due to ( $\Gamma$ ) and the shift in the resonances due to ( $\sigma$ ). When  $E = E_n + \sigma_L + \sigma_R + \Gamma_L + \Gamma_R$ ,  $T(E) = \frac{T_{max}}{2}$ . Therefore, the half-width of resonance is  $\Gamma_L + \Gamma_R$ . Where  $\delta E$  shows the energy level which is much larger than the resonance width. For symmetrical system,  $\Gamma_L = \Gamma_R$ ,  $T_{max} = 1$ .

### 3.11.2 Anti-resonance

Quantum interference between multiple paths can lead to on-resonances (peaks) or anti-resonances (dips) in the transmission function  $T(E)$  controlling charge transport. Although the resonant

condition ( $E$  close to  $E_n$ ) described by the Breit–Wigner formula is a consequence of constructive interference, it is worth noting that the formula also contains information about destructive interference. Therefore, in the case of destructive quantum interference, an anti-resonance in the transmission coefficients appears and then  $T(E)$  is destroyed when  $\Gamma_L$  and  $\Gamma_R$  are proportional to  $(\psi_i^n)^2$  and  $(\psi_j^n)^2$ , respectively. Where  $(\psi_i^n)^2$  and  $(\psi_j^n)^2$  are the amplitudes of the wavefunctions (i.e., molecular orbital) and therefore Eq. 3.72 could be written  $\Gamma_L$  as:

$$\Gamma_L = \frac{\alpha^2}{\gamma_L} \sin(k_L) (\psi_i^n)^2 \quad (3.76)$$

Hence,  $\Gamma_L$  and  $\Gamma_R$  will vanish if either  $(\psi_i^n)^2$  and  $(\psi_j^n)^2$  coincide with nodes (the two paths of the amplitudes of the wavefunction are out of phase) due to the result of Eq. 3.72, which describe the Green's function of the whole combined structure when a wave propagates from nodal atom  $i$  to nodal atom  $j$ .<sup>25</sup>

An example of the transmission coefficient  $T(E)$  for a ring consisting of six atoms coupling weakly to the leads is shown in Figure 3.11. it represents the phenomenon of destructive quantum interference (DQI), which arises when anti-resonances or a sharp dip occurs in the transmission probability.

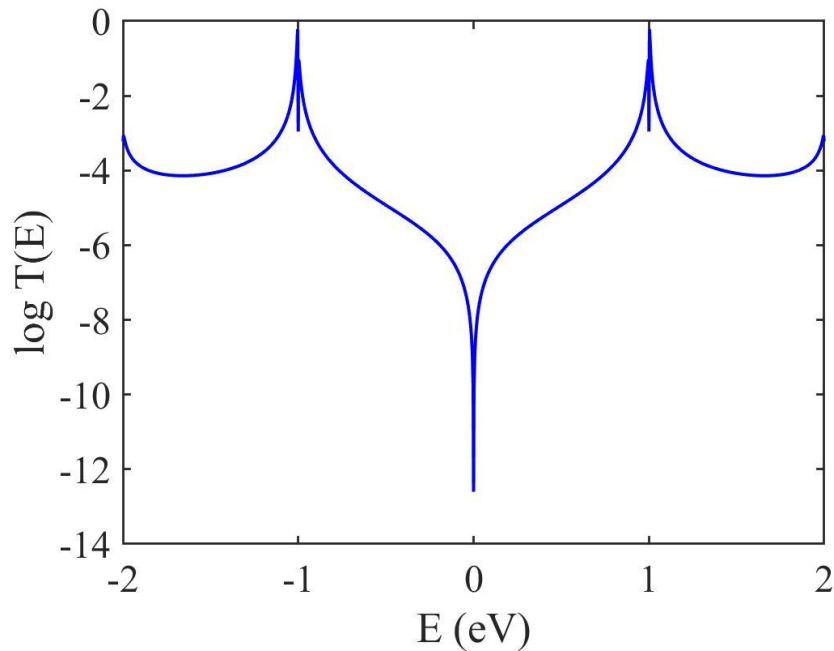


**Figure 3.11.** The transmission coefficients  $T(E)$  of the ring system demonstrate an anti-resonance: leading to steep slopes, where the appearance of two peaks rather than six peaks corresponding to six atoms are the degeneracies concerning their energy eigenvalues.

### 3.12 Green's Functions

Green's function of the scatterer emerged as a natural tool for solving the Schrödinger equation for a scatterer connected to two one-dimensional leads. The relationship between Green's and wave functions opens the way to using efficient methods of solving scattering problems. Therefore, it is helpful to understand Green's functions by finding an analytic formula for a different structure. The following is similar to the route of computing quantum properties when finding the eigenstates or the eigenvalues in the first section and leads to expressions for Green's functions for these structures.<sup>1,26</sup>

Hence, the general definition of the Green's function  $G(E)$  belonging to a Hamiltonian  $H$  is:

$$(EI - H)G(E) = I \quad (3.77)$$

where  $I$  is the unit matrix, and the solution for this equation can be written as:

$$G(E) = (E - H)^{-1} \quad (3.78)$$

In what follows, this equation will be discussed when  $H$  is an infinite matrix corresponding to an open system; for example, describe Green's function  $G(E)$  of a doubly infinite linear chain.

### 3.12.1 Green's function of a doubly infinite linear chain

In general, the retarded Green's function described the response of a system at a point  $j$  due to a source  $p$  as shown in Figure 3.13.

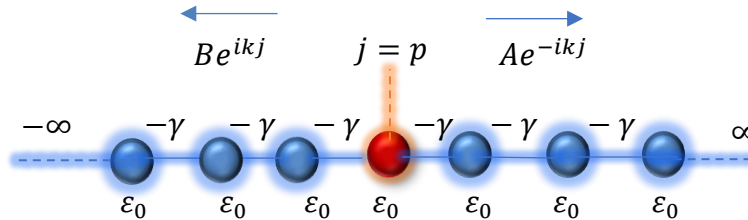


**Figure 3.12.** Tight-binding model of one-dimensional infinite chain with on-site energies  $\varepsilon_0$  and couplings  $-\gamma$ .

By highlighting the relationship between Green's functions and waverfunctions, the following notation:

$$G_{jp} = \psi_j^{(p)} \quad (3.79)$$

where  $G_{jp}$  is Green's matrix element belonging to the  $p^{th}$  column and  $j^{th}$  row,  $\psi_j^{(p)}$  is the amplitude of column vector  $\psi^{(p)}$  at site  $j$  and therefore can be written Eq.3.77 as

$$\sum_{l=-\infty}^{\infty} H_{jl} G_{lp}(E) = EG_{jp}(E) - \delta_{jp} \quad (3.80)$$

where  $\delta_{jp}$  is Kronecker delta satisfying  $\delta_{jp} = 1$  if  $j = p$  and  $\delta_{jp} = 0$  if  $j \neq p$ .

Substituting Eq.3.79 into Eq.3.80, yields:

$$\sum_{l=-\infty}^{\infty} H_{jl} \psi_l^{(p)} = E\psi_j^{(p)} - \delta_{jp} \quad (3.81)$$

This is almost identical to the Schrödinger equation, except for the presence of the Kronecker delta on the right-hand side, then Eq.3.81 can be written as:

$$\varepsilon_o \psi_j^{(p)} - \gamma\psi_{j-1}^{(p)} - \gamma\psi_{j+1}^{(p)} = E\psi_j^{(p)} - \delta_{jp} \quad (3.82)$$

Then the solution to Eq.3.82 is:

$$\psi_j^{(p)} = \phi_j = Ae^{ikj} \text{ for } j > p \quad (3.83)$$

$$\psi_j^{(p)} = f_j = Be^{-ikj} \text{ for } j < p \quad (3.84)$$

When  $j = p + 1$ , Eq. 3.82 and Eq. 3.83 yield

$$\varepsilon_o \phi_{p+1} - \gamma\psi_p^{(p)} - \gamma\phi_{p+2} = E\phi_{p+1} \quad (3.85)$$

Since  $\phi_j$  satisfies Eq.3.81 for all values of  $j$ , this yields

$$\varepsilon_o \phi_{p+1} - \gamma\phi_p - \phi_{p+2} = E\phi_{p+1} \quad (3.86)$$

Comparing equations Eq.3.85 and Eq.3.86 yields

$$\psi_p^{(p)} = \phi_p \quad (3.87)$$

The same procedure is used for  $j = p - 1$ , Hence

$$\psi_p^{(p)} = f_p \quad (3.88)$$

Therefore, Eq.3.87 and Eq.3.88 yield

$$\psi_p^{(p)} = \phi_p = f_p \quad (3.89)$$

$Ae^{ikp} = Be^{-ikp}$ , yields  $A = Ce^{-ikp}$  and  $B = Ce^{ikp}$ , therefore

$$\phi_j = Ce^{ik(j-p)} \text{ and } f_j = Ce^{-ik(j-p)} \quad (3.90)$$

To determine the value of the constant  $C$ , Eq.3.82 is satisfied for the case  $j = p$ , hence

$$C = \frac{1}{2i\gamma \sin k} = \frac{1}{i\hbar v(E)} \quad (3.91)$$

Where  $v(E)$  is the group velocity. Thus, the retarded Green's function, which the two outgoing waves from the source  $p$ , is is

$$G_{jp}(E) = \psi_j^{(p)} = \frac{e^{ik|j-p|}}{i\hbar v(E)} \quad (3.92)$$

Eq.3.92 is not the most general solution because the Schrödinger equation could be added to  $\psi_j^{(p)}$ .

Therefore, the most general solution is:

$$G_{jp}(E) = \psi_j^{(p)} = \frac{e^{ik|j-p|}}{i\hbar v(E)} + Ae^{ikj} + Be^{-ikj} \quad (3.93)$$

By choosing  $A = -\frac{e^{ik(j-p)}}{i\hbar v}$  and  $B = -\frac{e^{-ik(j-p)}}{i\hbar v}$ , the Green's function in this case is called advanced Green's function, which is the complex conjugate of the retarded Green's function.<sup>1,27</sup>

$$G_{jp}(E) = \psi_j^{(p)} = -\frac{e^{-ik(E)|j-p|}}{i\hbar v(E)} \quad (3.94)$$

### 3.13 Conclusion

This chapter studied electron transport in nanoscale structures by presenting a quantum transport theory involving the time independent Schrödinger equation to solve the eigenvalue problem for different one-dimensional crystalline models. The solutions have been presented in a tight-binding model (TBM) for investigating the common quantum properties of the Schrödinger wave equation, such as the eigenfunctions and eigenvalues of the Hamiltonian matrix. In addition, the definition of bond current between different sites in a quantum system using the time dependent Schrödinger equation has been explained. To illustrate the main ideas, an overview of the scattering theory introducing the simplest problem of a single impurity placed between doubly infinite chain one-dimensional has been illustrated to find the connection between the scattering matrix and the transport properties. The Landauer formula could estimate the electrical conductance through the scattering region connected to two electrodes. Hence, the Green's function formalism has calculated the transmission coefficient for different simple transport regimes and their generic transport features, such as Breit-Wigner resonances and anti-resonances.

### 3.14 Bibliography

1. Lambert, C. J. (2021). *Quantum Transport in Nanostructures and Molecules: An introduction to molecular electronics*. IOP Publishing.
2. Burke, K. (2012). Perspective on density functional theory. *The Journal of chemical physics*, 136(15), 150901.
3. Spiegelman, F., Tarrat, N., Cuny, J., Dontot, L., Posenitskiy, E., Martí, C., Simon, A., and Rapacioli, M. (2020). Density-functional tight-binding: Basic concepts and applications to molecules and clusters. *Advances in Physics: X*, 5(1), 1710252.
4. Sadeghi, H. (2016). *Theory of electron and phonon transport in nano and molecular quantum devices: design strategies for molecular electronics and thermoelectricity*. Lancaster University (United Kingdom).
5. Atkins, P. W., and Friedman, R. S. (2011). *Molecular quantum mechanics*. Oxford university press.
6. Rae, A. I. (2005). *Quantum physics: a beginner's guide*. Simon and Schuster.
7. Sutton, A. P. (1993). *Electronic Structure of Materials*. ProQuest Ebook Central.
8. Manrique, D. Z., Huang, C., Baghernejad, M., Zhao, X., Al-owaedi, O. A., Sadeghi, H., Kaliginedi, V., Hong, W., Gulcur, M., Wandlowski, T., Bryce, M. R., and Lambert, C. J. (2015). A quantum circuit rule for interference effects in single-molecule electrical junctions. *Nature Communications*, 6, 6389.
9. Chelikowsky, J. R. (2019). *Introductory Quantum Mechanics with MATLAB®: For Atoms, Molecules, Clusters, and Nanocrystals*. 224.
10. Brouwer, P. W. (1998). Scattering approach to parametric pumping. *Physical Review B*, 58(16), R10135–R10138.
11. Datta, S. (1997). *Electronic transport in mesoscopic systems*. Cambridge university press.
12. Fagas, G., Kozorezov, A. G., Lambert, C. J., Wigmore, J. K., Peacock, A., Poelaert, A., and Hartog, R. den. (1999). Lattice-dynamics of a Disordered solid-solid Interface. *Physical Review B*, 60(9), 6459–6464.
13. Wang, K. (2018). DNA-Based Single-Molecule Electronics: From Concept to Function. *Journal of Functional Biomaterials*, 9(1), 8.
14. Fisher, D. S., and Lee, P. A. (1981). Relation between conductivity and transmission matrix. *Physical Review B*, 23(12), 6851–6854.
15. Büttiker, M., Imry, Y., Landauer, R., and Pinhas, S. (1985). Generalized many-channel conductance formula with application to small rings. *Physical Review B*, 31(10), 6207–6215.

16. van Wees, B. J., van Houten, H., Beenakker, C. W. J., Williamson, J. G., Kouwenhoven, L. P., van der Marel, D., and Foxon, C. T. (1988). Quantized conductance of point contacts in a two-dimensional electron gas. *Physical Review Letters*, 60(9), 848–850.
17. Segal, D., Nitzan, A., and Hänggi, P. (2003). Thermal conductance through molecular wires. *The Journal of Chemical Physics*, 119(13), 6840–6855.
18. Famili, M. (2018). Theory of molecular scale thermoelectricity. Lancaster University (United Kingdom).
19. Hou, S. (2019). Theory of molecular-scale transport in nanojunctions. Lancaster University (United Kingdom).
20. Agrait, N., Yeyati, A. L., and van Ruitenbeek, J. M. (2003). Quantum properties of atomic-sized conductors. *Physics Reports*, 377(2–3), 81–279.
21. Büttiker, M. (1986). Four-Terminal Phase-Coherent Conductance. *Physical Review Letters*, 57(14), 1761–1764.
22. Rubio, G., Agrait, N., and Vieira, S. (1996). Atomic-Sized Metallic Contacts: Mechanical Properties and Electronic Transport. *Physical Review Letters*, 76(13), 2302–2305.
23. Lambert, C. J., and Liu, S.-X. (2018). A Magic Ratio Rule for Beginners: A Chemist’s Guide to Quantum Interference in Molecules. *Chemistry - A European Journal*, 24(17), 4193–4201.
24. Wu, Q. (2018). Theory of molecular-scale transport in graphene nanojunctions. Lancaster University (United Kingdom).
25. Lambert, C. J. (2012). Basic concepts of quantum interference and electron transport and in single-molecule electronics. *Chemical Society Reviews*, 18.
26. Sam-ang, P. (2018). Projector-based Electron Transport Calculations.
27. Odashima, M. M., Prado, B. G., and Vernek, E. (2016). Pedagogical introduction to equilibrium Green’s functions: Condensed matter examples with numerical implementations. *Revista Brasileira de Ensino de Física*, 39(1).

## Chapter 4

### Electronic structure investigation of Double N-Heterocyclic Carbene Anchors

The following research was carried out in collaboration with the experimental group led by Professor Zhong-Ning (State Key Laboratory of Structural Chemistry, Fujian Institute of Research on the Structure of Matter, Chinese Academy of Sciences), who synthesised the studied molecules and Professor Wenjing Hong (State Key Laboratory of Physical Chemistry of Solid Surfaces, College of Chemistry and Chemical Engineering, iChEM, Xiamen University), who conducted the experiments.

This chapter uses the theoretical tools outlined in chapters 2 and 3 to provide thorough theoretical investigations of a series of N-Heterocyclic carbenes complexes as precursors of double NHC-anchored single-molecule junctions (see Figure. 4.1). This study contains seven molecules involving monomer and dimer molecules. The monomers and dimers configurations use different anchor groups, including direct carbon contact (C), methyl sulphide (SMe), pyridyl (Py) and a five-membered ring. Since these molecules have several possible binding sites to gold electrodes, identifying their strongest-binding contact required two steps. First, I study the geometric electronic structures of the isolated molecules. Next, I introduced a gold tip and scanned it across the molecules to find the sites with the strongest binding energies. In chapter 5, this information

provides a starting point for computing the electrical conductances of molecules, when contacted to two gold electrodes.

#### 4.1 Motivation

The fabrication of highly conductive and stable molecular devices is critical for the future development of single-molecule electronics. N-Heterocyclic carbenes (NHCs) are commonly used as versatile ligands in transition metals due to their high stability and conductivity. NHC-anchored plays a significant role in developing new sensors, electronics, and nanomaterials. NHCs have proven to be particularly beneficial ligands on nanoscale particles and surfaces. Weidner et al. revealed in 2011 that NHCs could act as ligands on gold surfaces.<sup>1</sup> Crudden *et al.* demonstrated self-assembled monolayers (SAMs) of NHCs to be exceptionally stable under chemical and physical stress.<sup>2</sup> NHC–metal interactions have been described by McBreen and Nuckolls and their co-workers as potentially available replacements to thiols (–SH).<sup>3</sup> Although thiols are the most widely employed as ligands for gold surfaces, acting as an anchor for functional groups with beneficial properties primarily because of the strong covalent S–Au bond and the efficient electronic coupling associated with it, the lack of long-term thermal stability and low conductivity of the S–Au interface limit the applications needed for modern electronics. The NHC–Au linkage is relatively stable under ambient conditions that affect the S–Au connection.<sup>4</sup> However, the formation of molecular junctions with both NHC anchors remains challenging due to the high chemical reactivity of free carbene. Our joint experiment demonstrates a novel strategy to fabricate NHC-anchored molecular devices using a photo-induced transmetalation reaction of air-stable silver compounds. It reveals that double NHC-anchored, single-molecule junctions can be

fabricated, with high electrical conductance <sup>5</sup>, measured using scanning tunnelling microscope-based break junction (STM-BJ) technique and predicted using density functional theory (DFT).

## 4.2 Introduction

The construction of robust and highly conductive molecular junctions is crucial for the future development of single-molecule electronic devices. According to studies of single molecules trapped between two metallics, the type of anchor groups, the molecular length, the nature of spacers, and the electronic structures of the aromatic subunits are all factors that affect charge transfer via these molecular devices electrodes.<sup>6</sup> The most common fabrication techniques are two-terminal junctions in electrode-molecule-electrode, with either a single molecule or a self-assembled monolayer (SAM) as the active component. Hence, one of the typical approaches for measuring single-molecule conductance is to place a pair of electrodes on a solid substrate and then use appropriate anchoring groups to connect the molecule to the electrodes.<sup>7</sup> Controlling charge transport in molecular junctions is an efficient molecular design approach that involves changing the anchoring group that connects the molecule to the metal—the anchoring group act as yet another electron-donating or accepting substituent. When assembling molecules into an actual junction, the choice of anchoring chemistry has a strong influence on the coupling strength between the metal and the electrodes, which significantly impacts the device's chemical stability and its charge transport properties.<sup>8,9</sup> Thiol (–SH), pyridine (–Py), and amine (–NH<sub>2</sub>) moieties are the most widely used anchoring groups in charge transport studies of single-molecule junctions because of their stable binding to metals (often gold electrodes) and good electrical coupling in nanoscale junctions with contact to leads. In addition, a thioether (–SMe) anchor group was also

employed as strong Au–S interactions.<sup>10,11</sup> It has been demonstrated that molecular junctions constructed using covalent Au–C  $\sigma$ -bonds of ethynyls as anchor groups coupled to gold electrodes show strong electronic coupling between molecules and gold electrodes, leading to reasonably high charge transport. However, there are only limited covalent Au–C bonding approaches to coupling molecular backbones to electrodes. To form highly conductive Au–C contacts, the strong  $\sigma$ -bonds of N-heterocyclic carbene (NHC) ligands allow the creation of strong carbon-metal  $\sigma$ -bonds when they coordinate with transition metals.<sup>12,13</sup>

One of the two terminals of a single molecule conducting wire was recently replaced by NHC<sup>5</sup> and showed higher conductance than non-covalent anchors. Since NHCs couple to gold electrodes via covalent Au–C  $\sigma$ -bonds, the fabrication of single-molecule junctions with both NHCs anchors could lead to high conductance; however, this possibility remains unexplored high chemical reactivity of free carbene. It is found that molecular junctions with NHCs as anchor groups possess high conductances. Density-functional-theory calculations show that these high values are due to strong Au–C bonds, which fix the dibenzofulvene in the nanogap and provide strong coupling with gold electrodes.<sup>14,15</sup> For this study, I shall compute the wave function and two types of binding energy to examine the electronic properties of the monomer and dimer molecules of N-heterocyclic carbene (NHC) groups using the DFT code SIESTA<sup>16</sup> and Gollum<sup>17</sup> transport code by employing a theoretical model described in chapters 2 and 3, respectively.

### 4.3 Studied Molecules

In order to measure the molecular electronic properties placed between two gold electrodes, it is vital to use a reliable source of electronic and structural data. The utilisation of density functional

theory calculations DFT, as mentioned in chapter 2, contributed to collecting information about these properties regarding the ground-state density. The optimum geometries and ground state Hamiltonian of each studied structure were self-consistently calculated using the DFT code SIESTA, which employs Troullier-Martins pseudopotentials<sup>18</sup> to account for the core electrons and a local atomic-orbital basis set to construct the valence states. To study the optimum geometries and ground state Hamiltonian of each structure of the isolated molecules were obtained by relaxing the molecules until all forces on the atoms were less than 0.01 eV/Å, as shown in Figure 4.1. A double-zeta polarisation basis set, norm-conserving pseudopotentials, an energy cut-off of 250 Rydbergs defining the real space grid were used. The local density approximation (LDA) with Ceperley-Alder (CA) parameterisation was chosen as the exchange-correlation functional. I also computed results using GGA with the Perdew-Burke-Ernzerhof parameterisation (PBE)<sup>19</sup> and found that the resulting electronic properties were comparable with those obtained using LDA.

Figures 4.1 and 4.2 below illustrate the studied structures with the same dibenzofulvene backbone and different anchor groups, wherein Figure 4.1 represents the monomer molecules **R-biNHC** and **biNHC**, and **N2F** with pristine pyridine (2Py) anchor groups, while **o-S2F** and **p-S2F** with pristine methyl sulphide (2SMe) anchor groups, respectively.

On the other hand, Figure 4.2 represents dimer molecules including **2Ag-2biNHC** and **2Au-2biNHC** with a bridging atoms such as silver (Ag) and gold (Au) with two **biNHC** molecules respectively. All these molecules were slightly twisted after relaxation, as shown in Figure 4.1.

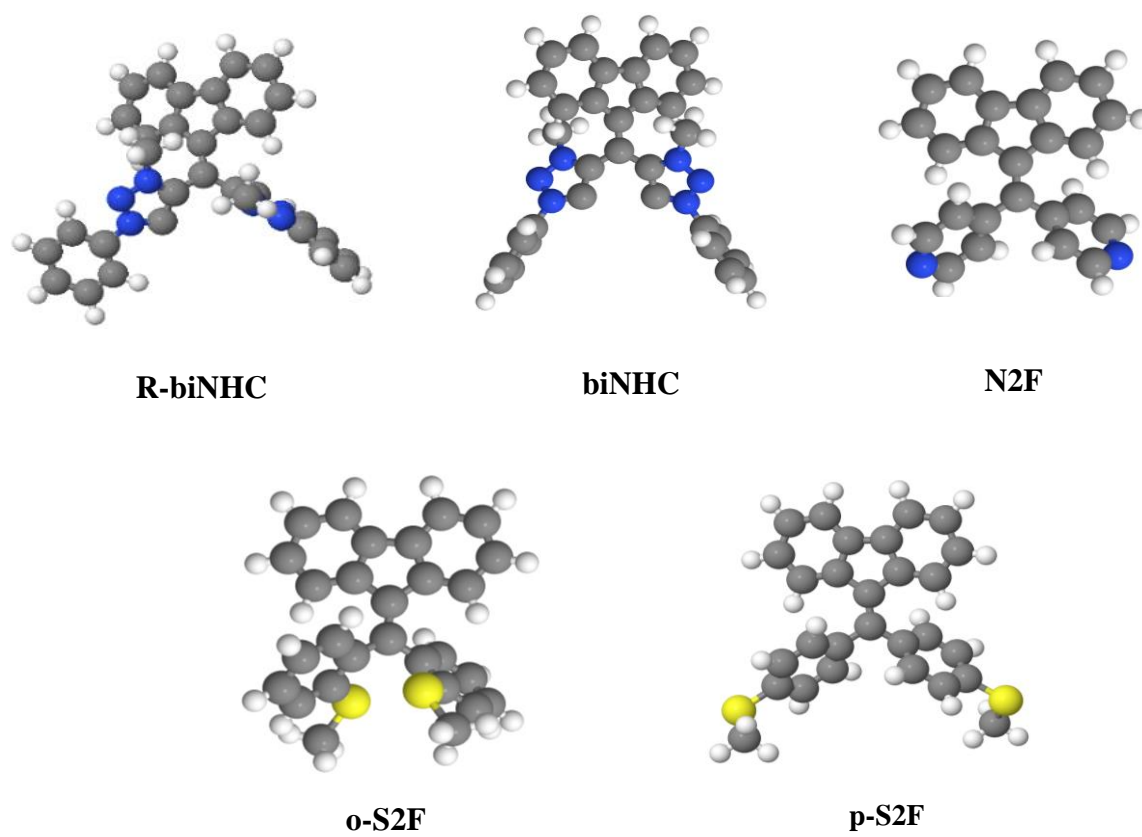


**Figure 4.1.** Fully relaxed isolated molecules. **Top panel.** Monomer molecules including **R-biNHC**, **biNHC** and **N2F** with pristine pyridyl anchor groups (2Py). **Lower panel.** Monomer molecules including **o-S2F** and **p-S2F** with pristine thioether anchor group (2SMe). Key: C = dark grey, H = white, N = blue, S = light yellow.

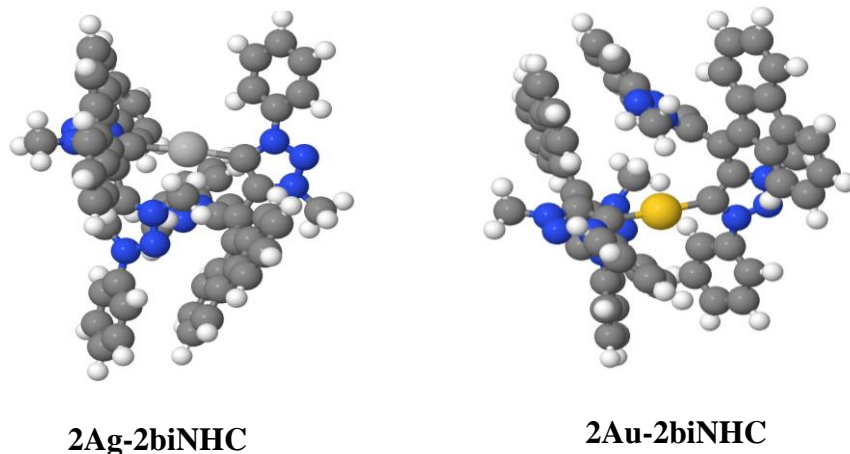


**Figure 4.2.** Fully relaxed isolated molecules. Dimer molecules including **2Ag-2biNHC** and **2Au-2biNHC** with bridging atoms such as Ag and Au respectively Key: C = dark grey, H = white, Ag = light grey and Au = dark yellow.

#### 4.4 Frontier orbitals of the molecules

This section will address the wavefunction of the seven compounds (see Figures 4.1 and 4.2) as orbitals of isolated molecules. Frontier orbitals HOMO (Highest occupied molecular orbitals) and LUMO (lowest unoccupied orbitals), which are the levels around Fermi energy and whose wave function is primarily focused on the molecule, maybe the most common participants in the transport. The methods of the orbital visualisation of wavefunction outlined in chapter 2 were used to obtain more knowledge of the electronic properties of the studied structures. The frontier orbital of these molecules is shown in Figures 4.3-4.9, where the highest occupied molecular orbitals (HOMO), lowest unoccupied orbitals (LUMO), HOMO-1 and LUM+1, along with their energies, are presented. The red and blue colours correspond to the regions in the space of positive and

negative orbital amplitude. The plots below show iso-surfaces of the HOMO, LUMO, HOMO-1 and LUMO+1 of isolated monomer and dimer molecules.

- Monomer case:

### 1. R-biNHC

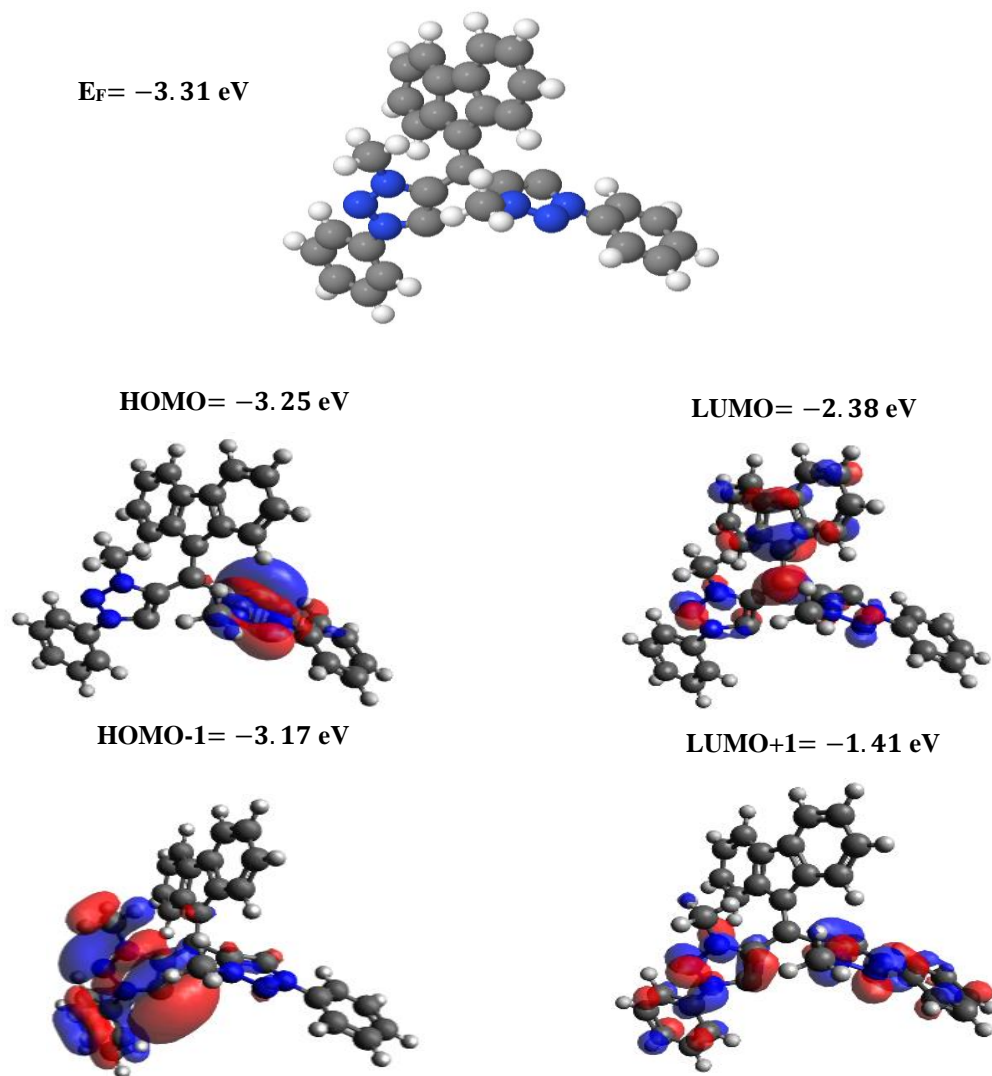


**Figure 4.3.** Wave function plot of R-biNHC. **Top panel:** Fully optimised geometry of R-biNHC. **Lower panel:** HOMO, LUMO, HOMO-1 and LUMO+1 plots of R-biNHC molecule along with their energies (monomer case).

## 2. biNHC

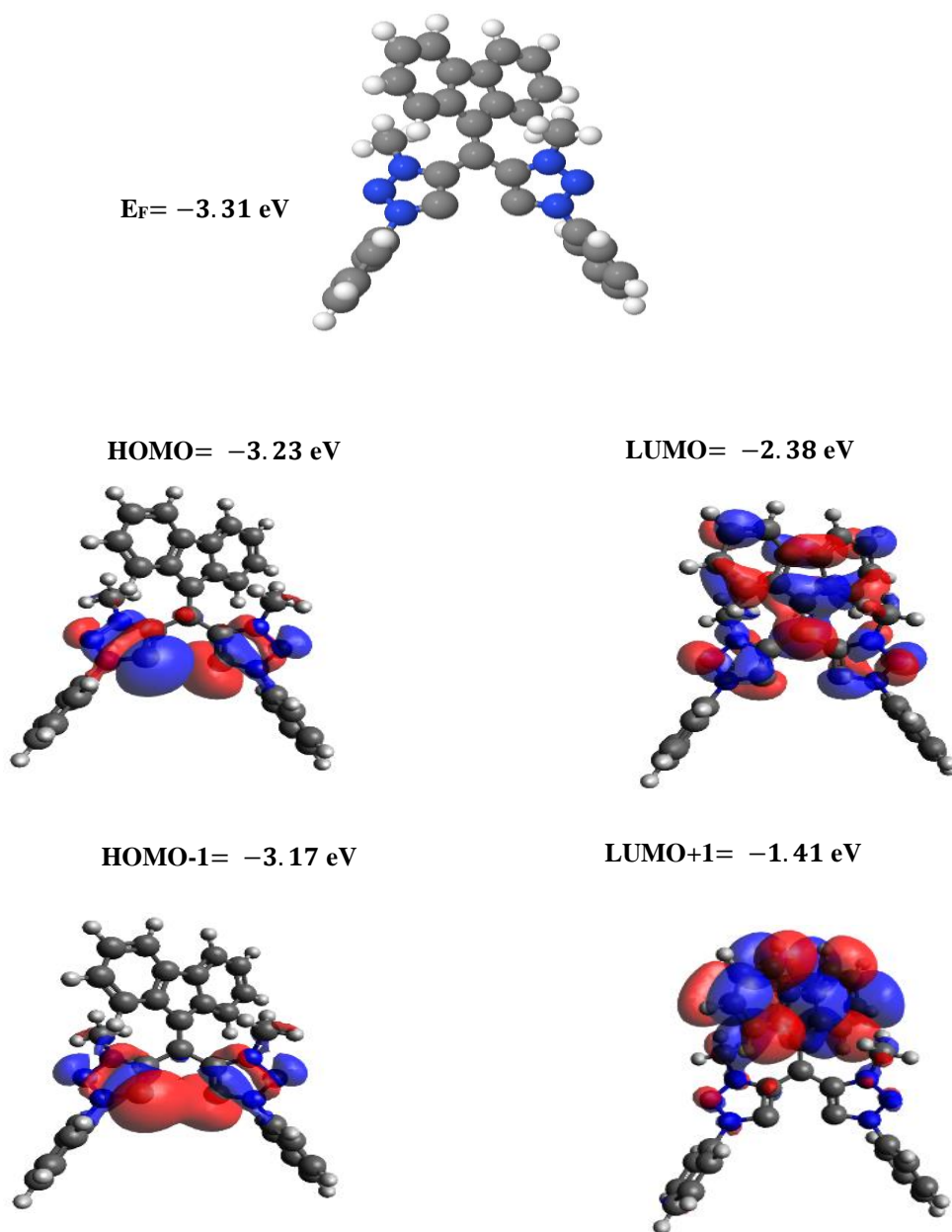


**Figure 4.4.** Wave function plot of **biNHC**. **Top panel:** Fully optimised geometry of **biNHC**. **Lower panel:** HOMO, LUMO, HOMO-1 and LUMO+1 plots of **biNHC** molecule along with their energies (monomer case).

### 3. N<sub>2</sub>F

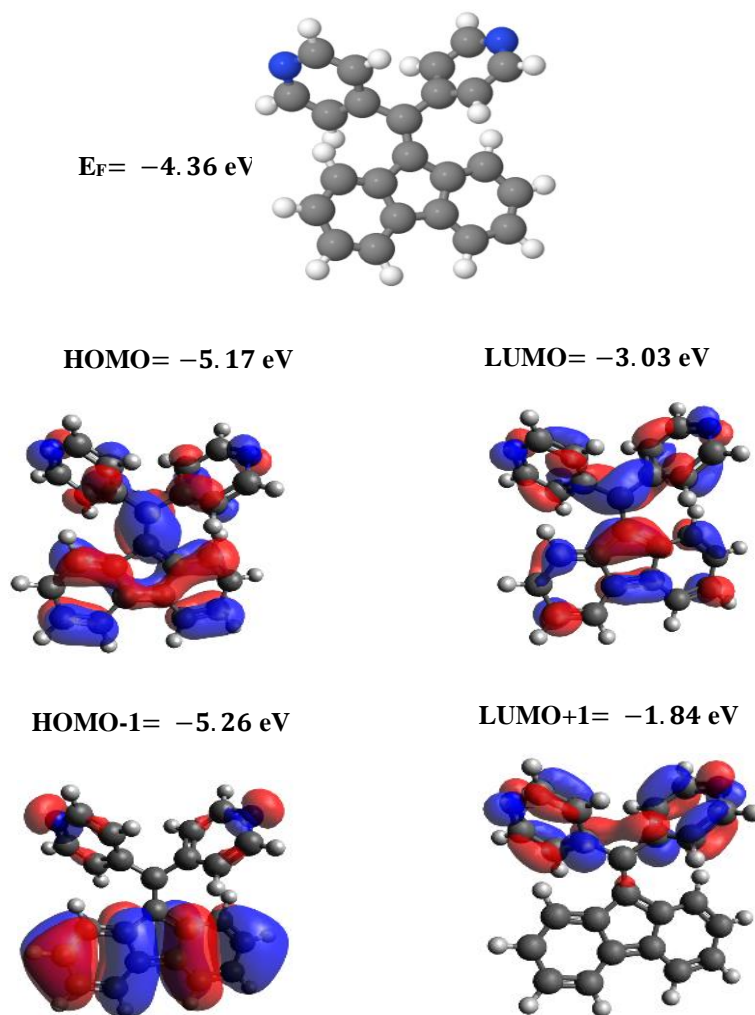


**Figure 4.5.** Wave function plot of N<sub>2</sub>F. **Top panel:** Fully optimised geometry of N<sub>2</sub>F. **Lower panel:** HOMO, LUMO, HOMO-1 and LUMO+1 plots of N<sub>2</sub>F molecule along with their energies (monomer case).

#### 4. o-S2F

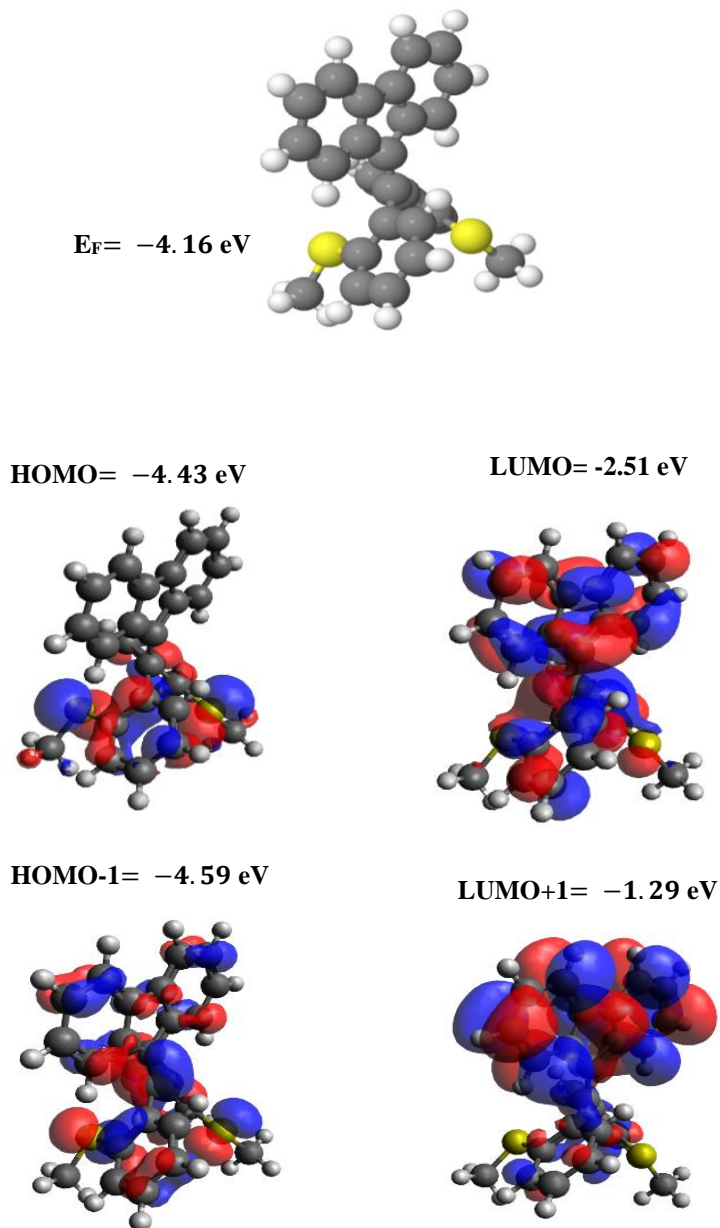


**Figure 4.6.** Wave function plot of o-S2F. **Top panel:** Fully optimised geometry of o-S2F. **Lower panel:** HOMO, LUMO, HOMO-1 and LUMO+1 plots of o-S2F molecule along with their energies (monomer case).

## 5. p-S2F

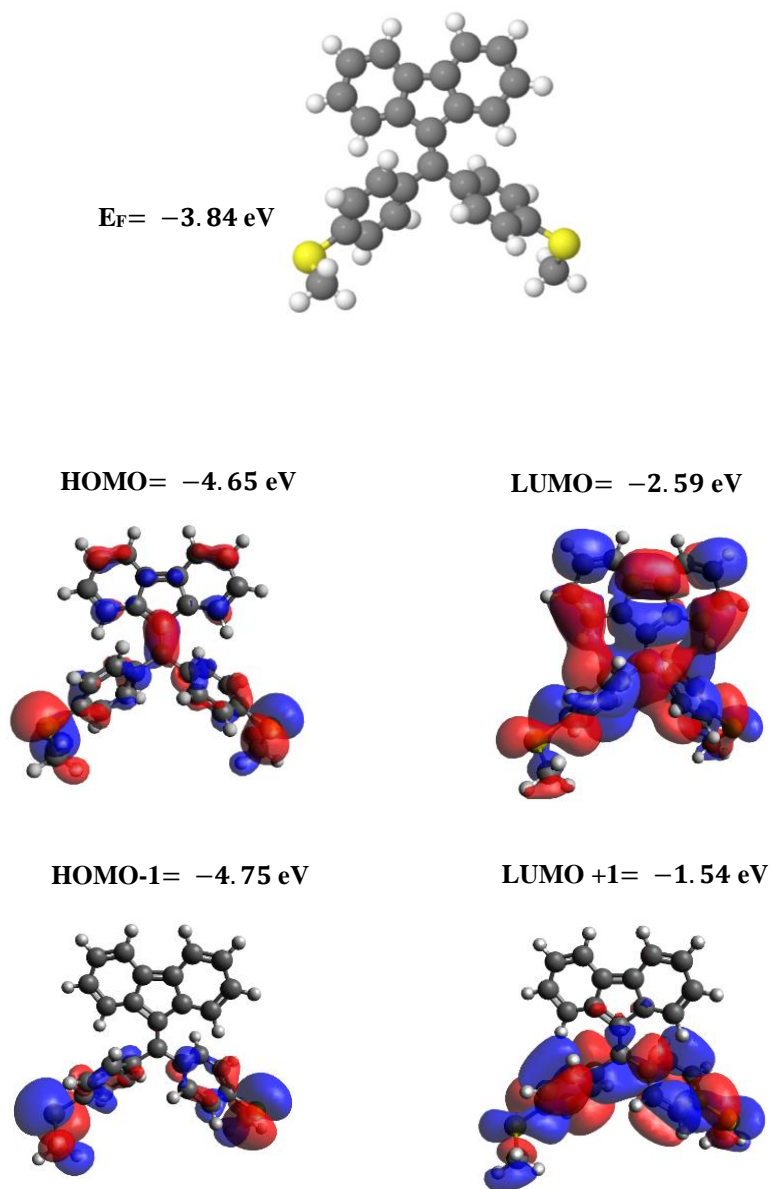


**Figure 4.7.** Wave function plot of **p-S2F**. **Top panel:** Fully optimised geometry of **p-S2F**. **Lower panel:** HOMO, LUMO, HOMO-1 and LUMO+1 plots of **p-S2F** molecule along with their energies (monomer case).

- Dimer case:

## 6. 2Ag-2biNHC

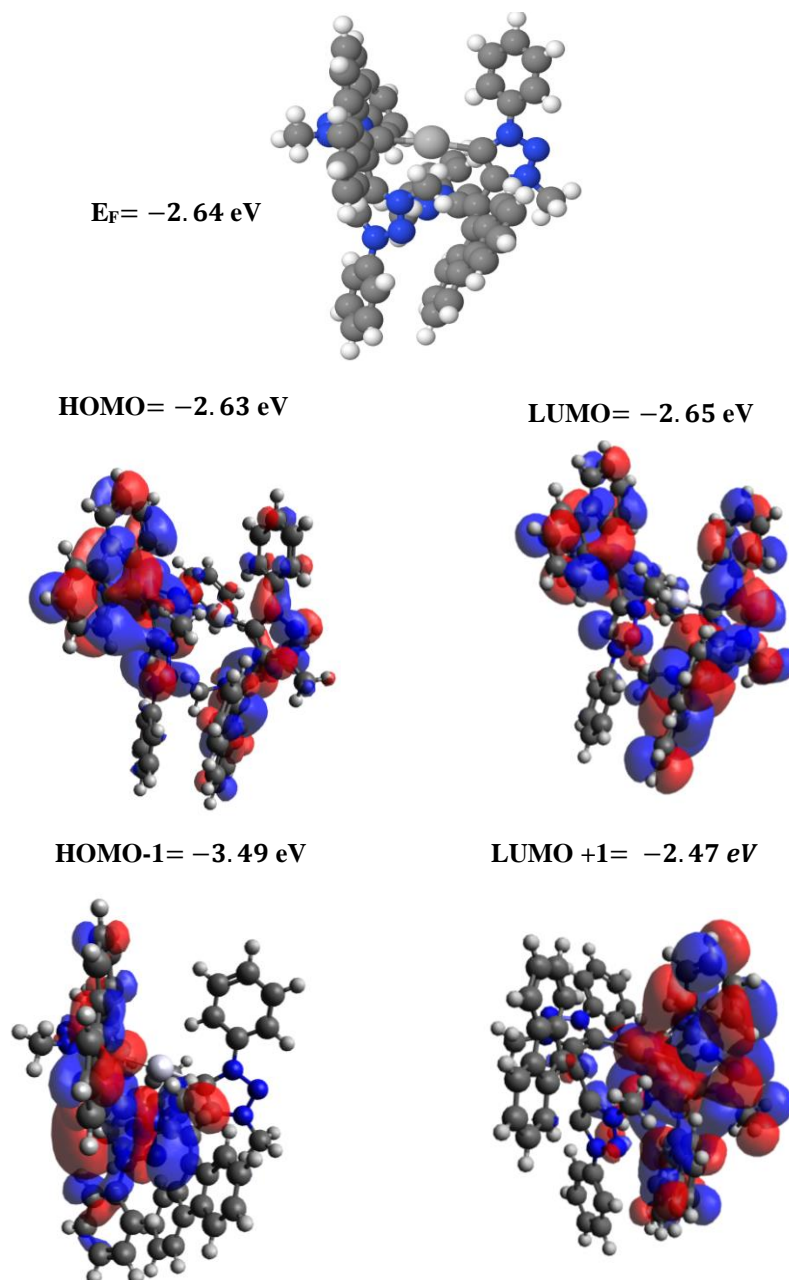


**Figure 4.8.** Wave function plot of 2Ag-2biNHC. **Top panel:** Fully optimised geometry of 2Ag-2biNHC. **Lower panel:** HOMO, LUMO, HOMO-1 and LUMO+1 plot of 2Ag-2biNHC molecule along with their energies (dimer case).

## 7. 2Au-2biNHC

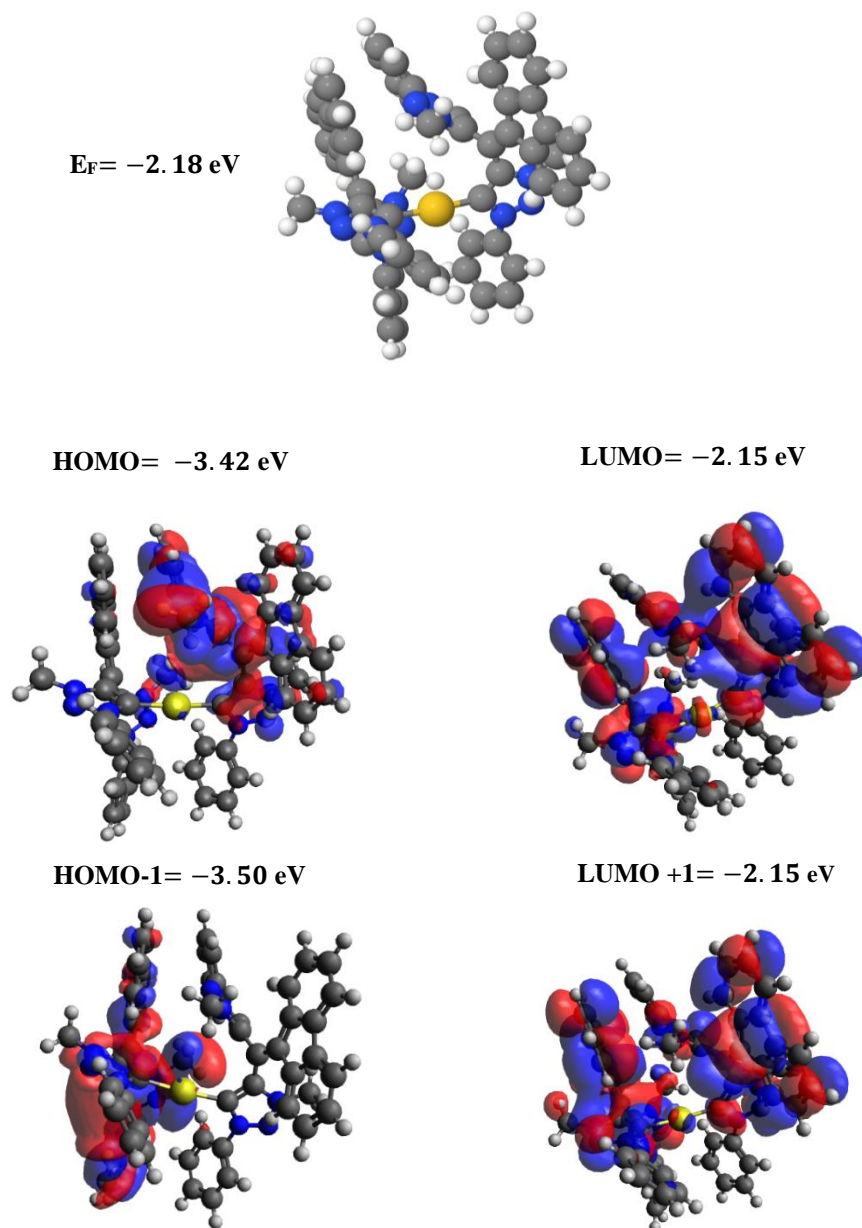


**Figure 4.9.** Wave function plot of 2Au-2biNHC. **Top panel:** Fully optimised geometry of 2Au-2biNHC. **Lower panel:** HOMO, LUMO, HOMO-1 and LUMO+1 plots of 2Au-2biNHC molecule along with their energies (dimer case).

## 4.5 Binding energy on a gold substrate

In section 2.5.3 (chapter two), the counterpoise method was described, which removes basis set superposition errors (BSSE)<sup>20</sup>, through the DFT calculations to compute the distance between two parts of the system or referred to as binding energy between two configurations. To calculate the optimum binding distance between the molecule and Au (111) surfaces, or the binding distance  $\mathbf{d}$ , which is defined as the distance between the gold surface and the anchor group, consider compound **2** (biNHC molecule see Figures 4.1) is defined as an entity  $A$  and the gold electrode as entity  $B$ . The ground state energy of the total system is calculated using SIESTA<sup>16</sup> and is denoted  $E_{AB}^{AB}$  for  $A$  and  $B$ . The energy of each entity is then calculated on a fixed basis, which is achieved using ghost atoms in SIESTA. Hence, the energy of the individual **1** in the presence of the fixed basis is defined as  $E_A^{AB}$  and for the gold as  $E_B^{AB}$ . The binding energy is then calculated using the following equation:

$$B.E = \Delta E(AB) = E_{AB}^{AB} - E_A^{AB} - E_B^{AB} \quad (4.1)$$

The optimized geometry of the isolated monomer and dimer molecules was obtained in the prior studied molecules section to model the electrode geometry. Then their geometry is bound to a gold electrode via the most favourable site or based on the anchor groups. By considering the nature of the binding depending on the gold surface structure, I calculated the binding to Au pyramid on a surface with the anchor atom binding at a ‘top’ site and then varied the binding distance  $\mathbf{d}$ . In the following section, the binding energies are calculated to find the optimum distance between the Au electrode and anchor groups for each configuration (see Figures 4.1 and 4.2) and then only investigate those who possess the highest binding energies employing two different techniques involving: 3-D and 1-D binding energy simulations.

### 4.5.1 3-D binding energy simulations

To find the optimum distance between the Au electrode and the anchor group for each of the seven studied molecules involving monomer and dimer molecules, I need to search mainly for all the potential strong binding energies between the Au and anchor groups.

In this section, as the targeted molecules could have more than one potential location (i.e., atom/atoms) to act as an anchor group then the whole backbone of the molecule requires to be scanned searching for possible anchors points. Therefore, I first examined the effect of varying the positions of the Au tip by placing the tip at different positions around the molecular backbone. Second, for every single location, the molecule's binding energy ( $B.E$ ) (see section 4.4) was calculated using the counterpoise method. Finally, I plotted all the possible positions of varying the gold tip as a function of the number of binding locations (number of steps). Consequently, the strongest binding energy values are signified as the most favourable positions (i.e., anchor groups).

Figure 4.10 below illustrates the 3-D binding energy method; it shows the Au tip placed at 300 different positions around compound **3** (**N2F** molecule) to find the most favourable positions.

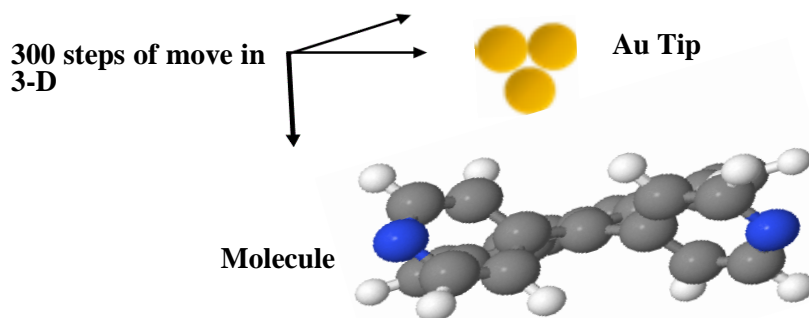


**Figure 4.10.** Sampling of the Au tip position around the molecular backbone searching for the strongest binding locations, (an example).

The binding energy (i.e., the difference in total energy with the Au tip at different positions) was calculated foremost for three molecules including compounds **1**, **2** or **4** and **5** (**R-biNHC** and **biNHC** or **o-S2F** and **p-S2F**) as these molecules have the same potential anchor groups and then computed secondly for compound **3** (**N2F** molecule). In each case, the binding energy (*B. E*) was calculated to find the preferred position which provides stable junctions for conductance studies. The first step in this process is to find the most favourable positions and then obtain the favourable binding energy between the Au electrode and the molecule. For compounds **1** and **2** (**R-biNHC** and **biNHC** molecules), these two molecules have the same molecular structures. As a result, I shall investigate only the three-dimensional binding energy of compound **2** (**biNHC** molecule), on the Au substrate.

To obtain the most favourable binding positions of gold electrodes to compound **2** (**biNHC** molecule see Figures 4.1), the molecule was scanned by placing the Au tip in 350 positions around the molecule. Figure 4.11 shows many bindings of the Au tip at different positions on compound **2** (**biNHC** molecule). Clearly, the strongest binding occurs at positions 80, 90 and 250. The binding energy for 80 and 90 positions is each approximately equal to 1.6 eV, while for 250 it is about 0.2 eV (red arrows). Positions 80, 90 correspond to Au-C bond, while the weaker 250 position corresponds to the case where the tip binds to the five-membered ring as shown in the top panel of Figure 4.11. These binding energies show that the Au-C bond is more than eight times stronger than the Au-five-membered ring bond. These preferred binding sites are also common features of **R-biNHC**, **2Au-2biNHC** and **2Ag-2biNHC**.

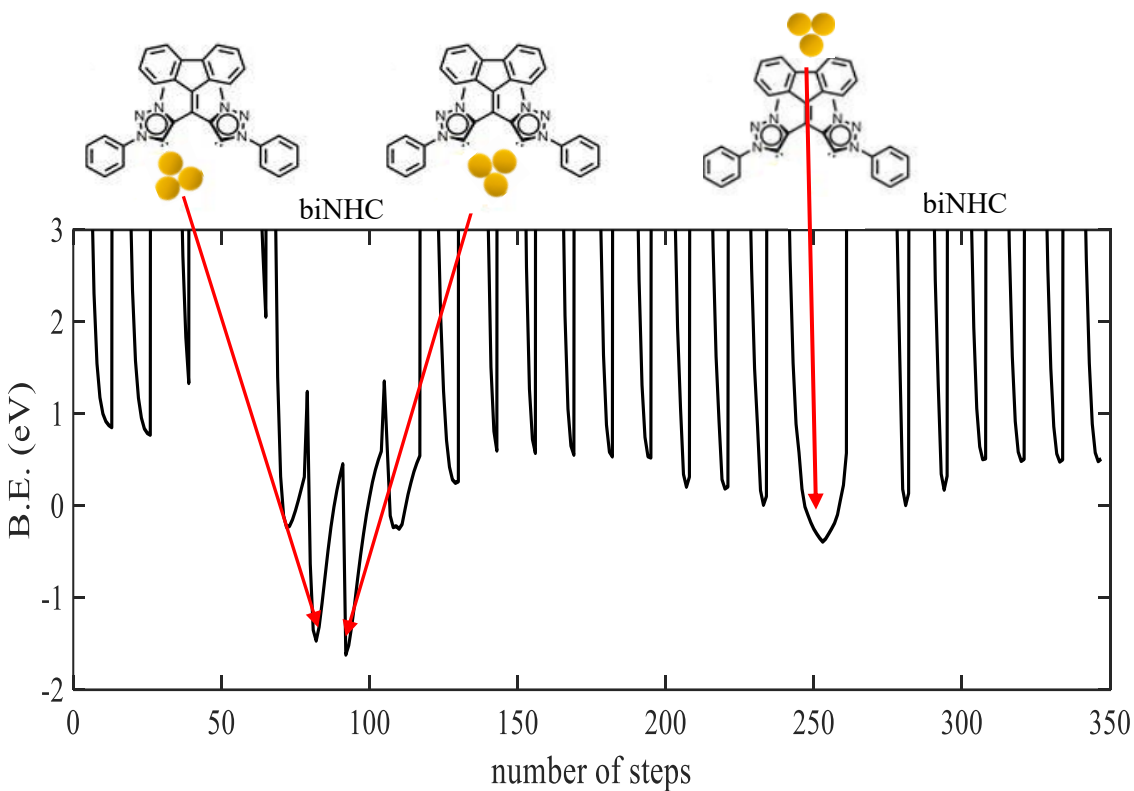


**Figure 4.11. Top panel:** Compound **2** (biNHC molecule) configuration at the Au-tip interface for three different positions: Au-C and Au-five-membered ring. **Lower panel:** 3-D binding energy plot as a function of Au-tip at 350 positions. 80 and 90 sites possess the stronger binding energy of Au-C bond, at approximately 1.6 eV. The 250 site possesses weaker binding energy of Au-five-membered ring bond, at approximately 0.2 eV.

The second scan finds the strongest bindings of compound **4** or **5** (**o-S2F** or **p-S2F** molecule), to the Au tip. These molecules have the same molecular structure and anchor group (i.e., SME). Consequently, I shall investigate the three-dimensional binding energy of compound **5** (**p-S2F** molecule), only as shown in Figure 4.12. This molecule has been scanned by the Au tip again in 350 locations. Figure 4.12 demonstrates that there are three strong binding energies in the energy

spectrum, labelled 125, 225 and 310, correspond to Au-SMe bonds and Au-five-membered-ring bonds. Furthermore, it also shows that the binding energy of the Au-SMe is stronger than the Au-to-five-membered ring bond (0.3 and 0.2 eV respectively, red arrows).

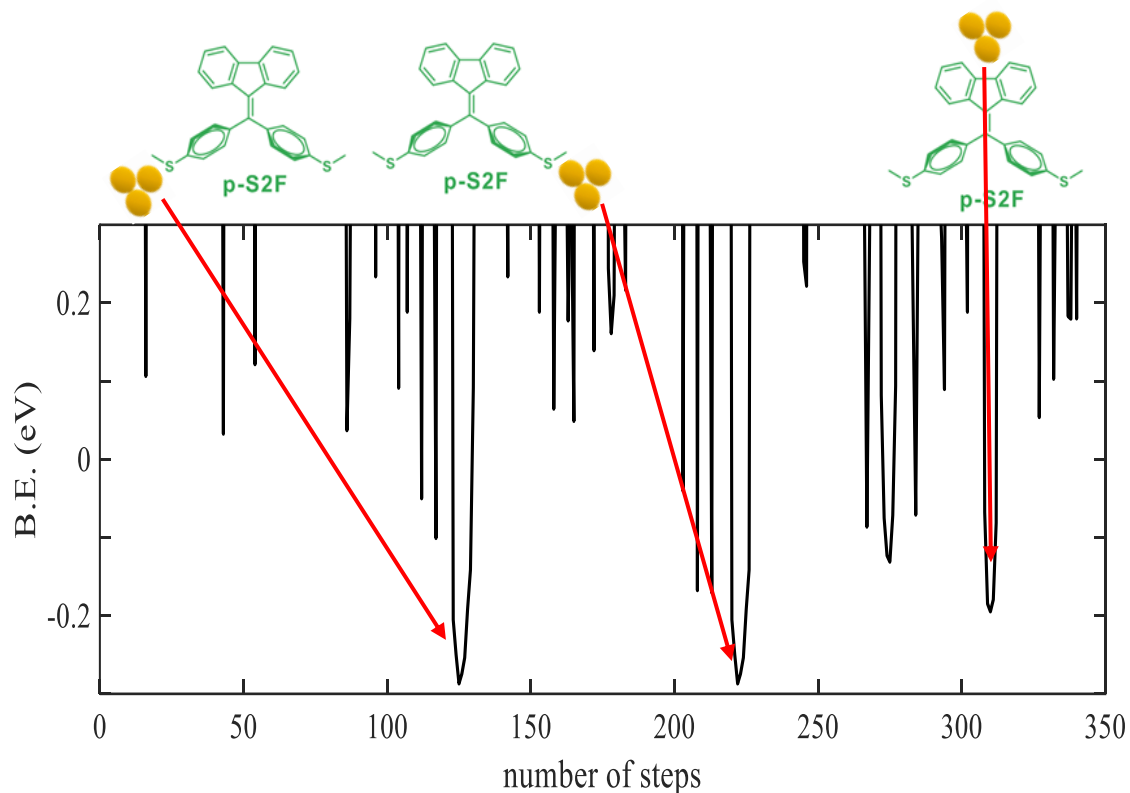


**Figure 4.12. Top panel:** Compound **5** (**p-S2F** molecule) configuration at the Au-tip interface for three different positions: Au-SMe and Au-five-membered ring. **Lower panel:** 3-D binding energy plots as a function of Au-tip at 350 positions. 125 and 225 sites possess stronger binding energy of Au-SMe bond, at approximately 0.3 eV. The 310 site possesses weaker binding energy of Au-five-membered ring bond, at approximately 0.2 eV.

The above approach (3-D scan simulations) has been repeated for compound **3** (**N2F** molecule). Figure 4.13 proves that the Au-N bond has the strongest dips in the energy spectrum. In this case,

compound **3** (**N2F** molecule) has been scanned by the Au tip in 300 different locations. Figure 4.13 illustrates many binding energies at different positions. However, the three strongest bonds are approximately 50, 190 and 270 sites, and these locations correspond to the bounds of Au-N and Au-five-membered rings. The dips demonstrate that the binding energy of Au-N is almost twice as strong the Au-five-membered ring, where the binding energies are found to be 0.5 and 0.2 eV, respectively.

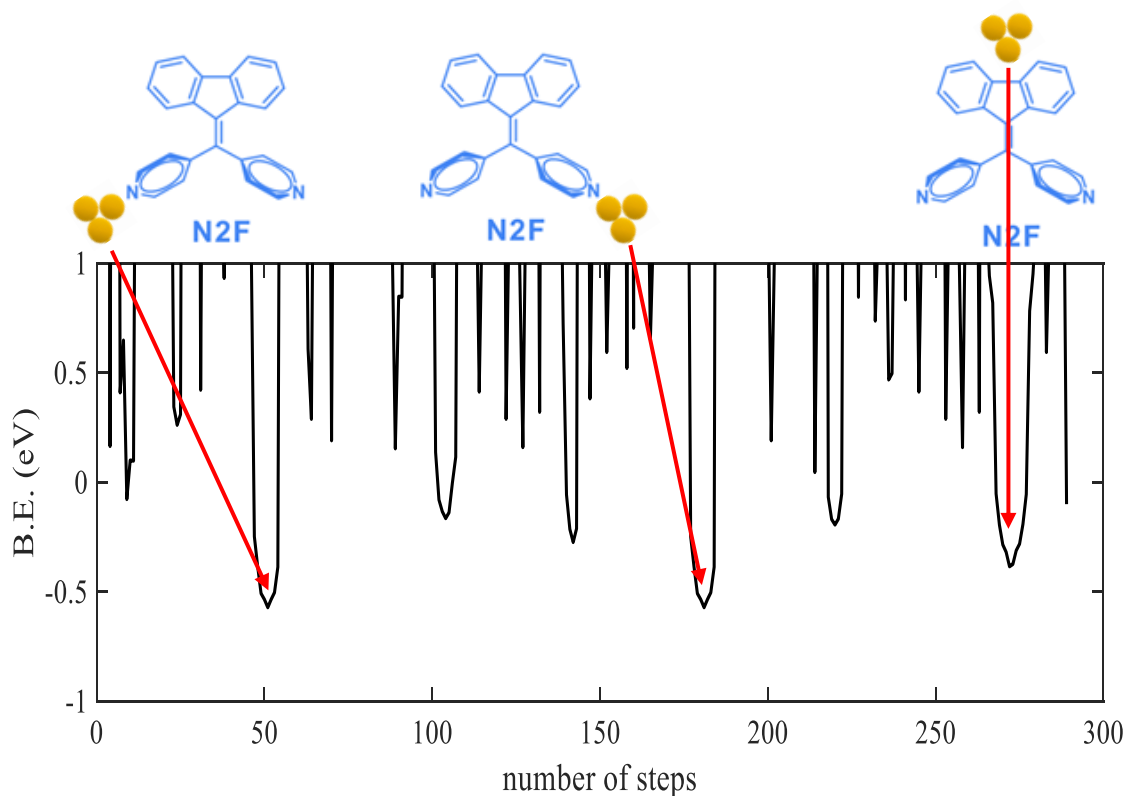


**Figure 4.13.** **Top panel:** Compound **3** (**N2F** molecule) configuration at the Au-tip interface for three different positions: Au-N and Au-five-membered ring. **Lower panel:** 3-D binding energy plots as a function of Au-tip at 300 positions. The 50 and 190 sites possess stronger binding energy of Au-N bond, at approximately 0.5 eV. The 270 site possesses weaker binding energy of Au-five-membered ring bond, at approximately 0.2 eV.

### 4.5.2 1-D binding energy simulations

After determining the three strongest binding locations in the energy spectrum for each molecule. The three locations (i.e., the minimum of the binding energy curve), correspond to either direct-C (Au-C), or pyridyl (Au-N) or methyl sulphide (Au-SMe), or Au-five-membered ring of the studied molecules. The next step is to determine the most favourable separation distances between the Au-tip and the anchor group (location), for this purpose I shall use 1-D scanning simulations. The binding distance  $d$  is defined as the distance between the gold surface and the anchor group (i.e., carbon/nitrogen/sulphide/5-membered ring). Here, by using the 1-D scan method four separation distances are found corresponding to Au-C, Au-N, Au-SMe and Au-five-membered ring. Figure 4.14 elucidates the separation distance between Au and the covalent bond to be approximately 2.3 Å with a binding energy of 1.6 eV. Similarly, the separation distance between Au and SMe group is found to be 2.7 Å with energy of roughly 0.3 eV as shown in Figure 4.15. 1-D energy scan results of methyl sulphides and direct contact (Figures 4.14 and 4.15), strong.<sup>21,22</sup>

Furthermore, the separation distance between Au and N is found to be 2.2 Å with minimum energy of roughly 0.5 eV as shown in Figure 4.16, which is consistent with literature studies.<sup>23,24</sup> Finally, the separation distance between Au and the five-membered ring is found to be 3.6 Å with minimum energy of roughly 0.2 eV as shown in Figure 4.17.

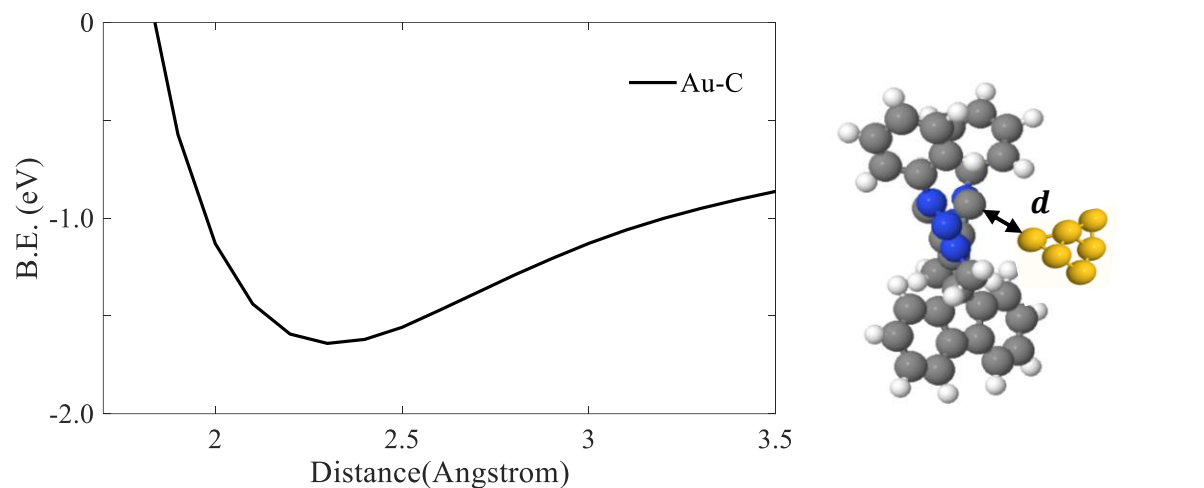


**Figure 4.14. Right panel:** Molecule configuration at the Au lead interface, compound **2** (biNHC molecule), a carbon atom linked to Au electrode. **Left panel:** An example of binding energy plot as a function of distance  $d$ . This distance is found to 2.3 Å, at approximately 1.6 eV.

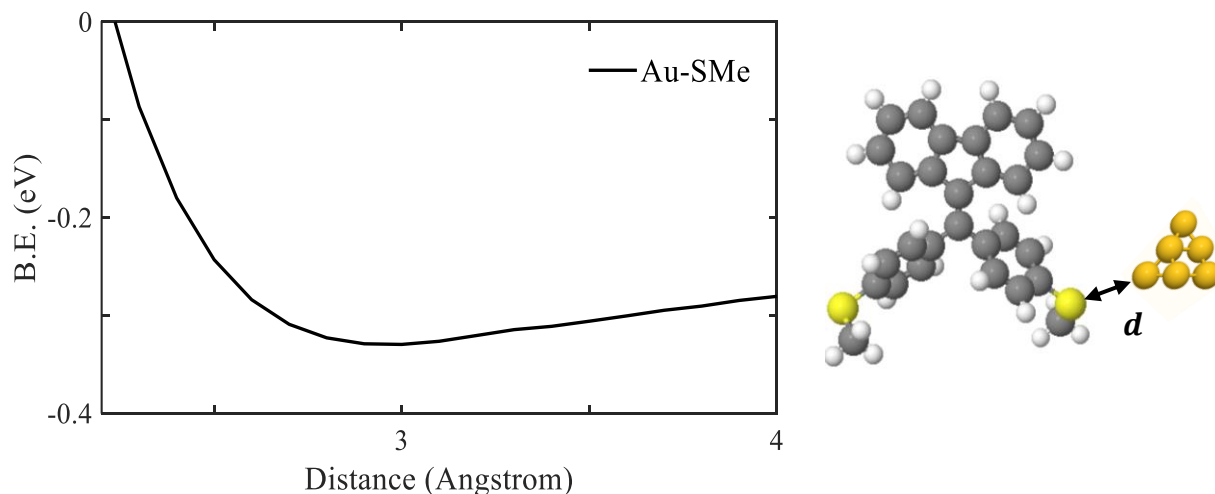


**Figure 4.15. Right panel:** Molecule configuration at the Au lead interface, compound **5** (p-S2F molecule), a sulphide (SMe) linked to Au electrode. **Left panel:** An example of binding energy plot as a function of distance  $d$ . This distance is found to 2.7 Å, at approximately 0.3 eV.

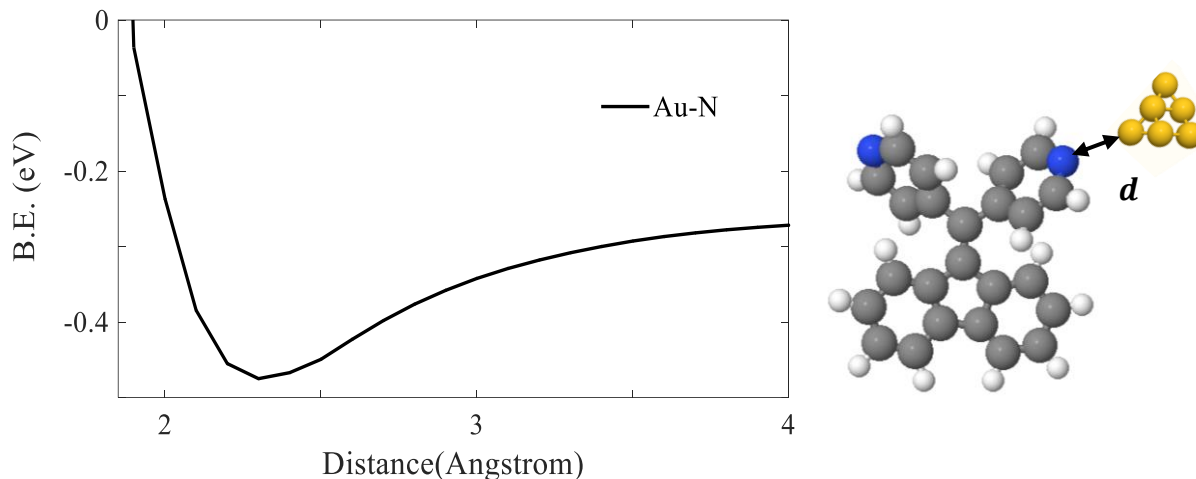


**Figure 4.16. Right panel:** Molecule configuration at the Au lead interface, compound **3** (N2F molecule), a Py linked to Au electrode. **Left panel:** An example of binding energy plot as a function of distance  $d$ . This distance is found to 2.2 Å, at approximately 0.5 eV.

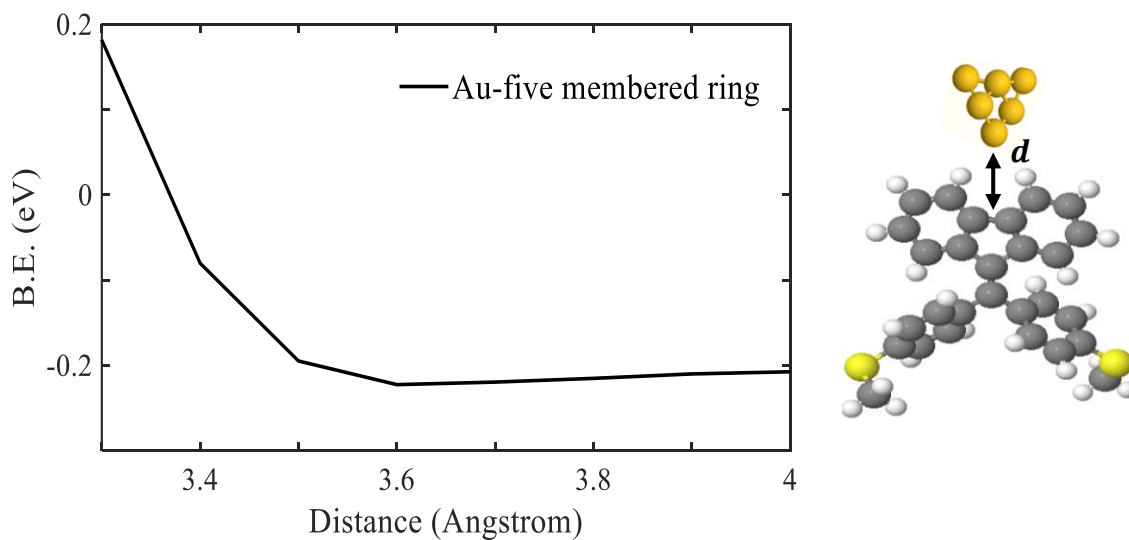


**Figure 4.17. Right panel:** Molecule configuration at the Au lead interface, compound **5** (p-S2F molecule), a five-membered ring linked to Au electrode. **Left panel:** An example of binding energy plot as a function of distance  $d$ . This distance is found to 3.6 Å, at approximately 0.2 eV.

The 3-D scanning simulations established the three strongest binding energy locations in the energy spectrum that correlated to direct-C (Carbon atom), pyridyl (Nitrogen atom), methyl sulphide (SMe group), and five-membered ring of the studied structures as shown in Figures 4.11 - 4.13. Consequently, determining the optimum separation distance and binding energy values for each molecule became achievable via 1-D scanning simulations as shown in Figures 4.14 - 4.17. Table 4.1 represents the optimum separation distance and the values of binding energy of 3-D/1-D results of the studied structures of the monomer molecules such as compounds **1**, **2**, **3**, **4** and **5** (**R-biNHC**, **biNHC**, **N2F**, **o-S2F** and **p-S2F** molecules). Thus, their binding energy values from 3-D/1-D scanning simulation are identical.

**Table 4.1.** Summarises the optimum separation distance  $d$  and the binding energy ( $B.E$ ) of 3-D/1-D scanning simulations of the studied molecules.

Contact	$B.E$ (eV)	$B.E$ (eV)	$d$ (Å)
	3-D	1-D	
Au-C	1.6	1.6	2.3
Au-N	0.5	0.5	2.2
Au-SMe	0.3	0.3	2.7
Au-five-membered ring	0.2	0.2	3.6

The binding energy between the electrode and studied molecules plays a crucial role in keeping an approximate distance between the anchor group and the closest gold atom. In addition to the substantive changes in transport depending on the structural detail, such as the molecular

conformation in the junction, very large differences in the single-molecule conductance follow from simple bonding considerations. A critical insight of early molecular transport examinations is the anchor group determines the dominant orbital of conductance and even to modify the dominant transport mechanism. Then, it can be attributed to the greater charge transferred due to the stronger binding energy ( $B. E$ ). A deep understanding of these details will guide the design of molecular electronic devices and improve their performances.<sup>11,24,25</sup>

## 4.6 Conclusion

In this chapter, the electronic properties of the isolated molecules were modelled using density-functional theory. The monomer and dimer molecules have several possible binding sites, and therefore the process of identifying them was divided into two stages. First, I scanned the whole molecule in 3-D with a gold tip to find the strongest-binding contact points. 3-D binding energy simulations examined the three strongest binding energy locations with a gold tip correlated to direct-C (Carbon atom), pyridyl (Nitrogen atom), methyl sulphide (SMe group), and five-membered rings. The second stage of the binding-energy simulations determined the optimum separation distance between the electrodes and the different anchor groups and their binding energy value after finding the most favourable location for each molecule (1-D binding energy simulations). In addition, the binding energy values between the gold electrodes and the different anchor groups calculated by the 3-D/1-D binding energy simulation were excellent agreement. These binding-energy simulations identified different binding scenarios for forming molecular junctions, which will be used in chapter 5, in order to study their transport properties.

## 4.7 Bibliography

1. Wang, G., Rühling, A., Amirjalayer, S., Knor, M., Ernst, J. B., Richter, C., Gao, H.-J., Timmer, A., Gao, H.-Y., Doltsinis, N. L., Glorius, F., and Fuchs, H. (2017). Ballbot-type motion of N-heterocyclic carbenes on gold surfaces. *Nature Chemistry*, 9(2), 152–156.
2. Nguyen, D. T., Freitag, M., Körsgen, M., Lamping, S., Rühling, A., Schäfer, A. H., Siekman, M. H., Arlinghaus, H. F., van der Wiel, W. G., Glorius, F., and Ravoo, B. J. (2018). Versatile Micropatterns of N-Heterocyclic Carbenes on Gold Surfaces: Increased Thermal and Pattern Stability with Enhanced Conductivity. *Angewandte Chemie International Edition*, 57(35), 11465–11469.
3. Crudden, C. M., Horton, J. H., Ebralidze, I. I., Zenkina, O. V., McLean, A. B., Drevniok, B., She, Z., Kraatz, H.-B., Mosey, N. J., Seki, T., Keske, E. C., Leake, J. D., Rousina-Webb, A., and Wu, G. (2014). Ultra stable self-assembled monolayers of N-heterocyclic carbenes on gold. *Nature Chemistry*, 6(5), 409–414.
4. Sun, N., Zhang, S., Simon, F., Steiner, A. M., Schubert, J., Du, Y., Qiao, Z., Fery, A., and Lissel, F. (2021). Poly(3-hexylthiophene)s Functionalized with N-Heterocyclic Carbenes as Robust and Conductive Ligands for the Stabilization of Gold Nanoparticles. *Angewandte Chemie International Edition*, 60(8), 3912–3917.
5. Doud, E. A., Inkpen, M. S., Lovat, G., Montes, E., Paley, D. W., Steigerwald, M. L., Vázquez, H., Venkataraman, L., and Roy, X. (2018). In Situ Formation of N-Heterocyclic Carbene-Bound Single-Molecule Junctions. *Journal of the American Chemical Society*, 140(28), 8944–8949.
6. Alanazy, A., Leary, E., Kobatake, T., Sangtarash, S., González, M. T., Jiang, H.-W., Bollinger, G. R., Agrait, N., Sadeghi, H., Grace, I., Higgins, S. J., Anderson, H. L., Nichols, R. J., and Lambert, C. J. (2019). Cross-conjugation increases the conductance of meta -connected fluorenones. *Nanoscale*, 11(29), 13720–13724.
7. Chen, F., Hihath, J., Huang, Z., Li, X., and Tao, N. J. (2007). Measurement of Single-Molecule Conductance. *Annual Review of Physical Chemistry*, 58(1), 535–564.
8. Obersteiner, V., Egger, D. A., and Zojer, E. (2015). Impact of Anchoring Groups on Ballistic Transport: Single Molecule vs Monolayer Junctions. *The Journal of Physical Chemistry C*, 119(36), 21198–21208.
9. Herrero, L., Ismael, A., Martín, S., Milan, D. C., Serrano, J. L., Nichols, R. J., Lambert, C., and Cea, P. (2019). Single molecule vs. Large area design of molecular electronic devices incorporating an efficient 2-aminepyridine double anchoring group. *Nanoscale*, 11(34), 15871–15880.
10. Gulcur, M. (2012). The Synthesis and Transport Properties of Conjugated Molecular Wires (Doctoral dissertation, Durham University).

11. O'Driscoll, L. J., and Bryce, M. R. (2021). A review of oligo(arylene ethynylene) derivatives in molecular junctions. *Nanoscale*, 13(24), 10668–10711.
12. Schuster, O., Yang, L., Raubenheimer, H. G., and Albrecht, M. (2009). Beyond Conventional N-Heterocyclic Carbenes: Abnormal, Remote, and Other Classes of NHC Ligands with Reduced Heteroatom Stabilization. *Chemical Reviews*, 109(8), 3445–3478.
13. Ye, J., Al-Jobory, A., Zhang, Q.-C., Cao, W., Alshehab, A., Qu, K., Alotaibi, T., Chen, H., Liu, J., Ismael, A. K., Chen, Z.-N., Lambert, C. J., and Hong, W. (2022). Highly insulating alkane rings with destructive  $\sigma$ -interference. *Science China Chemistry*, 65(9), 1822–1828.
14. Cui, X. D., Primak, A., Zarate, X., Tomfohr, J., Sankey, O. F., Moore, A. L., Moore, T. A., Gust, D., Harris, G., and Lindsay, S. M. (2001). Reproducible Measurement of Single-Molecule Conductivity. *Science*, 294(5542), 571–574.
15. Xu, B., and Tao, N. J. (2003). Measurement of Single-Molecule Resistance by Repeated Formation of Molecular Junctions. *Science*, 301(5637), 1221–1223.
16. Soler, J. M., Artacho, E., Gale, J. D., García, A., Junquera, J., Ordejón, P., and Sánchez-Portal, D. (2002). The SIESTA method for ab initio order-N materials simulation. *Journal of Physics: Condensed Matter*, 14(11), 2745.
17. Ferrer, J., Lambert, C. J., García-Suárez, V. M., Manrique, D. Z., Visontai, D., Oroszlany, L., Rodríguez-Ferradás, R., Grace, I., Bailey, S. W. D., Gillemot, K., Sadeghi, H., and Algharagholy, L. A. (2014). GOLLUM: A next-generation simulation tool for electron, thermal and spin transport. *New Journal of Physics*, 16(9), 093029.
18. Troullier, N., and Martins, J. L. (1991). Efficient pseudopotentials for plane-wave calculations. II. Operators for fast iterative diagonalization. *Physical Review B*, 43(11), 8861–8869.
19. Stampfl, C., and Van de Walle, C. G. (1999). Density-functional calculations for III-V nitrides using the local-density approximation and the generalized gradient approximation. *Physical Review B*, 59(8), 5521–5535.
20. Kobko, N., and Dannenberg, J. J. (2001). Effect of Basis Set Superposition Error (BSSE) upon ab Initio Calculations of Organic Transition States. *The Journal of Physical Chemistry A*, 105(10), 1944–1950.
21. Ismael, A. K., and Lambert, C. J. (2019). Single-molecule conductance oscillations in alkane rings. *Journal of Materials Chemistry C*, 7(22), 6578–6581.
22. Naher, M., Milan, D. C., Al-Owaedi, O. A., Planje, I. J., Bock, S., Hurtado-Gallego, J., Bastante, P., Abd Dawood, Z. M., Rincón-García, L., Rubio-Bollinger, G., Higgins, S. J., Agraït, N., Lambert, C. J., Nichols, R. J., and Low, P. J. (2021). Molecular Structure–(Thermo)electric Property Relationships in Single-Molecule Junctions and Comparisons with Single- and Multiple-Parameter Models. *Journal of the American Chemical Society*, 143(10), 3817–3829.

23. O'Driscoll, L. J., Wang, X., Jay, M., Batsanov, A. S., Sadeghi, H., Lambert, C. J., Robinson, B. J., and Bryce, M. R. (2020). Carbazole-Based Tetrapodal Anchor Groups for Gold Surfaces: Synthesis and Conductance Properties. *Angewandte Chemie International Edition*, 59(2), 882–889.
24. Liu, Z., Ding, S.-Y., Chen, Z.-B., Wang, X., Tian, J.-H., Anema, J. R., Zhou, X.-S., Wu, D.-Y., Mao, B.-W., Xu, X., Ren, B., and Tian, Z.-Q. (2011). Revealing the molecular structure of single-molecule junctions in different conductance states by fishing-mode tip-enhanced Raman spectroscopy. *Nature Communications*, 2(1), 305.
25. Herrer, I. L., Ismael, A. K., Milán, D. C., Vezzoli, A., Martín, S., González-Orive, A., Grace, I., Lambert, C., Serrano, J. L., Nichols, R. J., and Cea, P. (2018). Unconventional Single-Molecule Conductance Behavior for a New Heterocyclic Anchoring Group: Pyrazolyl. *The Journal of Physical Chemistry Letters*, 9(18), 5364–5372.

## Chapter 5

### Highly Conductive Single-molecule Junctions with Double N-Heterocyclic Carbene Anchors

This work was a collaboration between the group of Prof. Zhong-Ning (State Key Laboratory of Structural Chemistry, Fujian Institute of Research on the Structure of Matter, Chinese Academy of Sciences), who synthesised the studied molecules, and the group of Prof. Wenjing Hong (State Key Laboratory of Physical Chemistry of Solid Surfaces, College of Chemistry and Chemical Engineering, iChEM, Xiamen University), who conducted the experiments. Theoretical work was carried out at Lancaster University.

#### 5.1 Introduction

This chapter builds upon the results of chapter 4, which investigated the electronic properties of monomer and dimer of N-Heterocyclic Carbenes. The present chapter aims to calculate their electrical conductances, which are obtained by evaluating the transmission coefficient  $T(E)$  at the Fermi energy. Based on the results of their binding geometry for each component using the 1-D and 3-D energy scan simulations in chapter 4 (see Figures 4.11-4.17), the gold-molecule binding configurations can adopt different binding scenarios. In what follows, after determining the optimum separation distance  $d$  for each component using binding energy simulations, the fully DFT optimised structures (the relaxed geometry of each isolated molecule, see Figures 4.1 and

4.2) are attached to Au electrodes then the studied molecule is again fully optimised employing SIESTA code <sup>1</sup> to build a gold-molecule-gold junction. These optimised systems were then used to calculate the transmission coefficient  $T(E)$  for the monomer junction of each compound **1**, **2**, **3**, **4** and **5** (**R-biNHC**, **biNHC**, **N2F**, **o-S2F** and **p-S2F**), while the spin polarised transport calculations are needed in the dimer junction of each compound **6** and **7** (**2Ag-2biNHC** and **2Au-2biNHC**, due to the metal ions (i.e., Ag and Au).

At the end of this work, I compare experimental measurements with my theoretical transport properties. This comparison will include not only their electrical conductances, but also the degree of level broadening. The latter is obtained theoretically from the widths of transmission resonances for all monomers and dimers of NHC-anchored molecular junctions. These electric properties of the seven different types of NHC molecular junctions were modelled using a combination of density functional theory and quantum transport theory described in chapters 2 and 3, respectively.

## 5.2 Transmission coefficient $T(E)$

The transmission coefficient curves  $T(E)$ , will be obtained using the Gollum transport code <sup>2</sup> which utilises the Green's function scattering approach <sup>3</sup> combined with density functional theory to compute transport properties of a wide variety of nanostructures by employing theoretical models described in chapter 3. Once  $T(E)$  is computed, I can calculate the zero-bias electrical conductance  $G$  using the Landauer formula (see section 3.9, in chapter 3). The transmission coefficients  $T(E)$  were calculated for the studied structures of monomer and dimer molecules based on the 1-D and 3-D energy scan results (three strongest binding energies), shown in chapter 4 (see Figures. 4.11- 4.13). Although the LUMO resonance is predicted to be pinned near the Fermi

Level ( $E - E_F^{DFT} = 0 \text{ eV}$ ) of the electrodes for these seven junctions, previous comparisons between theory and experiment<sup>4-6</sup> suggest that better agreement is obtained when the Fermi level is taken closer to the mid-gap. The absolute position of the electrodes' Fermi level cannot be predicted, since it depends on the electrodes' local geometry and the surrounding nano-environment, which change frequently during a real STM-BJ experimental measurement. Therefore, molecular conductance cannot be precisely measured, but information about it can be deduced from the behaviour of  $T(E)$  curve within the HOMO-LUMO gap, where  $E_F$  is most commonly seen.<sup>7,8</sup> However, in the current study, the DFT-predicted Fermi level ( $E - E_F^{DFT} = 0 \text{ eV}$ ) yields a good agreement with STM measurements, as we will see in section 5.4 (Theory versus experiment). In addition, the pinning of the LUMO resonance close to the Fermi energy accounts for the different conductance values for NHC-anchored single-molecule junctions, which are in reasonable agreement with earlier experimental and theoretical results.<sup>6,9,10</sup>

In the following transport calculations of the monomer and dimer molecules in Au junctions, I examined three binding scenarios based on the 1-D and 3-D energy scanning results. The transmission coefficient curves  $T(E)$  were calculated for the monomer molecules firstly in three scenarios: **A**, **B**, and **C** and then dimer molecules secondly as follows:

### 5.2.1 Transport calculations of monomers

1-D and 3-D scan simulations exhibited the most three energetically favourable locations and binding distances between the Au electrode and the end group of the studied molecules as shown in chapter 4 (see Figures 4.11-4.17). The transmission coefficient  $T(E)$  for the corresponding three

dips (minimum energy), is going to be calculated and presented in three scenarios **A**, **B**, and **C**.

Table 5.1 illustrates the three scenarios.

**Table 5.1.** Summarises the three scenarios **A**, **B**, and **C** and the bond nature based on the three strongest binding energies for compounds **1**, **2**, **3**, **4** and **5** (**R-biNHC**, **biNHC**, **N2F**, **o-S2F** and **p-S2F**), and describe their symmetric/ asymmetric structures.

Scenario	Bond nature	Compound	Symmetric/ Asymmetric
<b>A</b>	Both contacts : Au-C, Au-N and Au-SMe	<b>biNHC/R-biNHC</b> , <b>N2F</b> and <b>S2F/p-S2F</b>	symmetric
<b>B</b>	Top contact: Au-five-membered ring. Bottom contact : Au-C, Au-N and Au-SMe	<b>biNHC/R-biNHC</b> , <b>N2F</b> and <b>o-S2F/p-S2F</b>	asymmetric
<b>C</b>	90 degrees between the two contacts. 6 nitrogen atoms (Au-N), and Au-C	<b>biNHC/R-biNHC</b> and <b>N2F, o-S2F/p-S2F</b>	asymmetric

I shall begin with scenario **A**, where the contacts (electrodes), attach to the same anchor group. The Au tips bind to a carbon atom directly to form a direct-C contact (Au-C), while in the pyridyl case the contact is via the N atom (Au-N). Similarly, with the methyl sulphide group, it happens via the S atom (Au-SMe). It should be note that scenario's **A** junctions are symmetric (i.e., electrodes connect to the same anchor groups). However, the case is different in scenario **B**, which

means the two electrodes do not attach to the same anchor group (i.e., asymmetric systems). The top Au contact attaches to the five-membered ring for all the monomer molecules, whereas the bottom contact binds to either C or N or SMe atom/s. For scenario **C**, there is 90 degrees between the two contacts for all the studied molecules which connect to the same position between gold leads and different anchors (symmetric structures), all these details are shown in Table 5.1. To have insight view about the 3 scenarios, I shall discuss them in more details/Figures in the next section.

## 5.2.2 Transport according to the three scenarios

### Scenario A:

Figure 5.1 shows schematic illustrations of the monomer molecules in Au junctions for scenario A. This scenario corresponds to the strongest binding between the molecule and electrodes, as shown in chapter 4 (see Figures 4.11-4.13). Figure 4.14 exhibits that compounds **1** and **2** (**R-biNHC** and **biNHC**), both bind to Au contact via a carbon atom (Au-C) with a separation distance of 2.3 Å, while compound **3** (**N2F**), binds via a pyridyl anchor (Au-N) with a separation distance of 2.2 Å (see Figure 4.16), and for compounds **4** and **5** (**o-S2F** and **p-S2F**), Au binds to a thioether group (Au-SMe), with the distance 2.7 Å (see Figure 4.15), these details also summarise in Table 4.1.

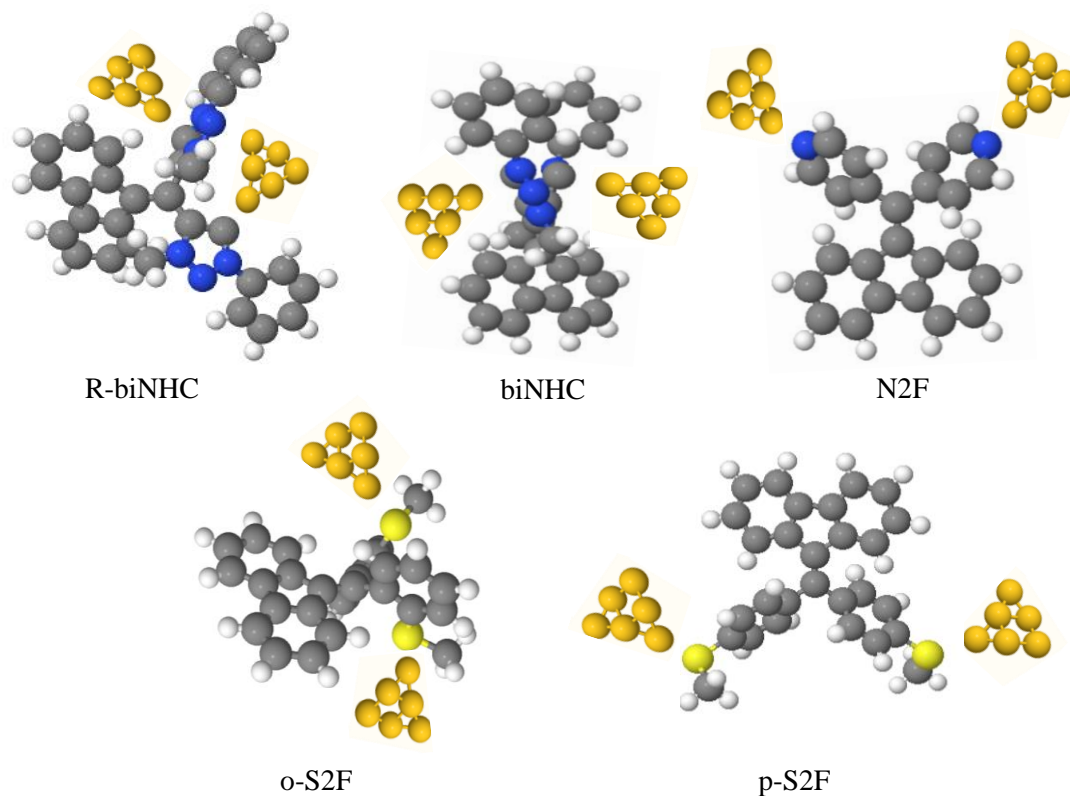


**Figure 5.1.** Schematic illustrations of the monomer molecules in Au junctions for Scenario A, in which the Au tips connect to the molecules as follows: compounds **1** and **2** (**R-biNHC** and **biNHC**) connect via Au-C bonds, compound **3** (**N2F**) connects via Au-N bonds, compounds **4** and **5** (**o-S2F** and **p-S2F**) connect via Au-SMe bonds.

Figure 5.2 shows the transmission coefficients  $T(E)$  as a function of energy for scenario A monomer molecules. These curves demonstrate that the transport here is a LUMO-dominated at the DFT-predicted Fermi energy ( $E - E_F^{DFT} = 0$  eV). The transmission coefficient  $T(E)$  curve calculates based on the bond nature that shown in Table 5.1, where diverse curves of the different colours correspond to different molecular junction of scenario A, as illustrated in Figure 5.2. One

would expect a LUMO-dominated transport for compounds **3**, **4** and **5** (**N2F**, **o-S2F** and **p-S2F**) due to the presence of the pyridyl and methyl sulphide anchor, respectively. However, it seems in the case of compounds **1** and **2** (**R-biNHC** and **biNHC**), the junctions still show a LUMO dominated transport and they terminated with carbon atom (direct-C) to Au.

It is worth noting the conductance depends on the magnitude of the transmission coefficients  $T(E_F)$ . Therefore, the conductance of the monomer molecules in Au junctions, which include compounds **1**, **2**, **3**, **4** and **5** (**R-biNHC**, **biNHC**, **N2F**, **o-S2F** and **p-S2F**), is calculated at the DFT-predicted Fermi energy ( $E - E_F^{DFT} = 0$  eV) to be  $10^{-1}G_0$ ,  $10^{-2}G_0$ ,  $10^{-4}G_0$ ,  $10^{-3}G_0$  and  $10^{-5}G_0$ , respectively. As a result, the compound **1** (**R-biNHC** molecule) has the highest conductance value for the covalent bond Au–C compared to other monomer molecules values in Au junctions for scenario **A**, such as the compound **5** (**p-S2F**) has the lowest conductance's molecule for the methyl sulphide (SMe) terminal group<sup>11</sup>. It can be attributed to that the binding energy of Au-C is stronger than that Py and SMe (see Table 4.1).<sup>7,12-15</sup>

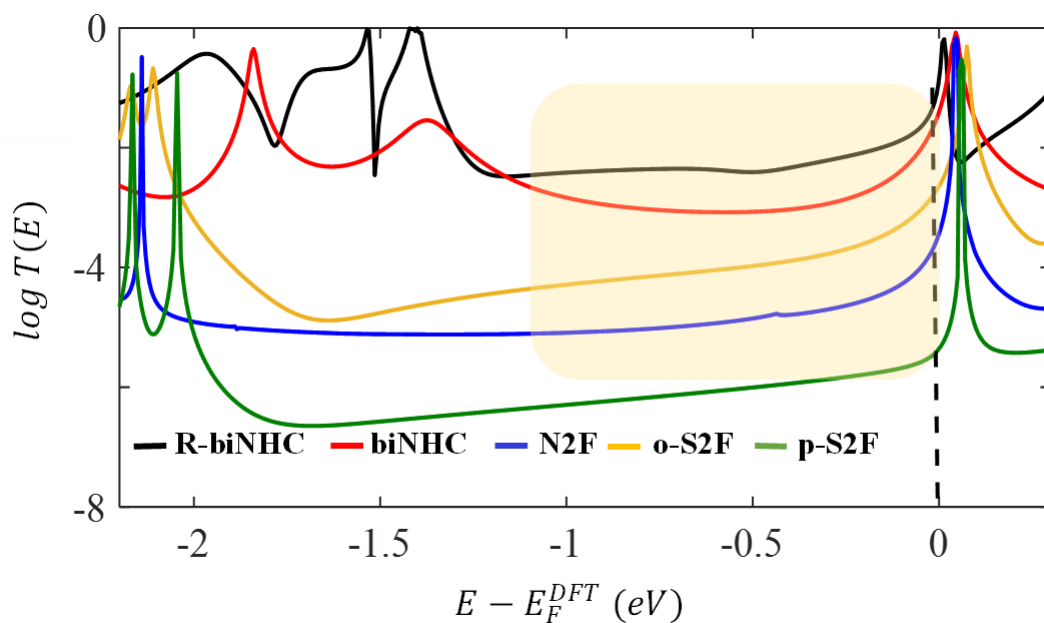


**Figure 5.2.** Transmission coefficients as a function of energy of the studied molecules in Au junctions for Scenario A. Zero bias transmission coefficients  $T(E)$  of compounds **1**, **2**, **3**, **4** and **5** (**R-biNHC**, **biNHC**, **N2F**, **o-S2F** and **p-S2F**) against electron energy  $E$ . The yellow rectangular box shows that a range of energy within the HOMO–LUMO gap.

### Scenario B:

This scenario corresponds to the second strongest binding as shown in chapter 4 (see Figures 4.11-4.13), where Au tip binds to (the five-membered ring) from one side end and in between the two anchors from the other end with separation distance of 3.6 Å for all monomer molecules in scenario **B** as shown in Tables 4.1 and 5.1. In this scenario the top contact is always to the five-membered ring for all molecules whereas the bottom contact is as follows for compounds **1** and **2** (**R-biNHC** and **biNHC**): between the two lower rings pointing towards two carbon atoms (Au-C), compound

**3 (N2F)**: between the two lower rings pointing towards the two pyridyl atoms (Au-N), compounds **4** and **5 (o-S2F and p-S2F)**: between the two lower rings pointing towards the two thioether atoms (Au-SMe) as illustrated in Figure 5.3.

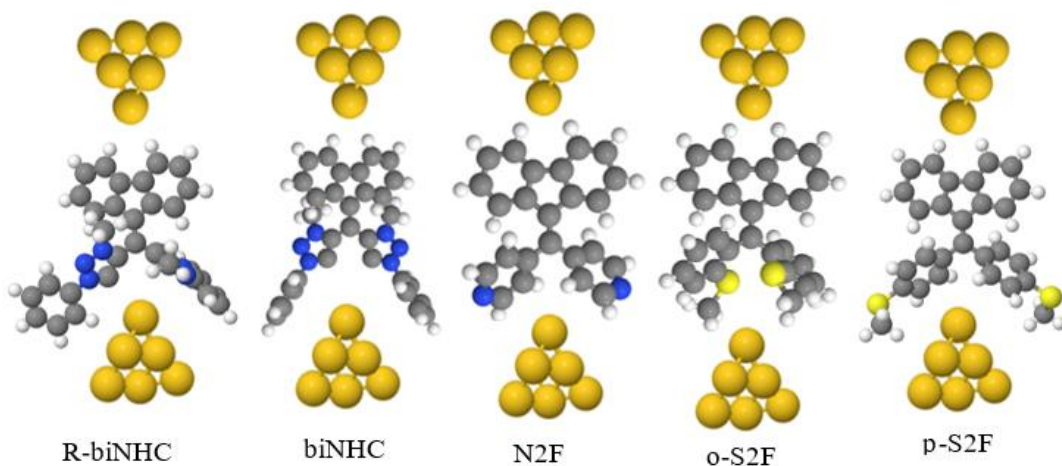


**Figure 5.3.** Schematic illustrations of the monomer molecules in Au junctions for Scenario **B**. It illustrates that the top contact is always to the five-membered ring for all molecules whereas the bottom contact as follows for compounds **1** and **2 (R-biNHC and biNHC)**: between the two lower rings pointing towards two carbon atoms (Au-C), compound **3 (N2F)**: between the two lower rings pointing towards the two pyridyl atoms (Au-N), compounds **4** and **5 (o-S2F and p-S2F)**: between the two lower rings pointing towards two thioether atoms (Au-SMe).

Figure 5.4 illustrates the transmission coefficients  $T(E)$  calculations as the energy of electron function for the monomer molecules in scenario **B**. These transport simulations show that this case is a LUMO-dominated level at the DFT-predicted Fermi energy ( $E - E_F^{DFT} = 0$  eV) (black dashed

line) for all these junctions of scenario **B**. The transmission coefficient  $T(E)$  curve calculates based on the binding energy type at the case of the five-membered ring bond as shown in Tables 4.1 and 5.1, where the different curves correspond to the Au junctions of scenario **B**, as illustrated in Figure 5.4. The magnitude of the transmission coefficients at the DFT-predicted Fermi energy ( $E - E_F^{DFT} = 0$  eV) is proportional to the conductance; hence, for compounds **1** and **2** (**R-biNHC** and **biNHC**) junctions have the higher conductance value, which is around  $10^{-1}G_0$  then compound **3**, **4** and **5** (**N2F**, **o-S2F**, and **p-S2F**) junctions of roughly  $10^{-2}G_0$ ,  $10^{-3}G_0$  and  $10^{-3}G_0$  respectively.

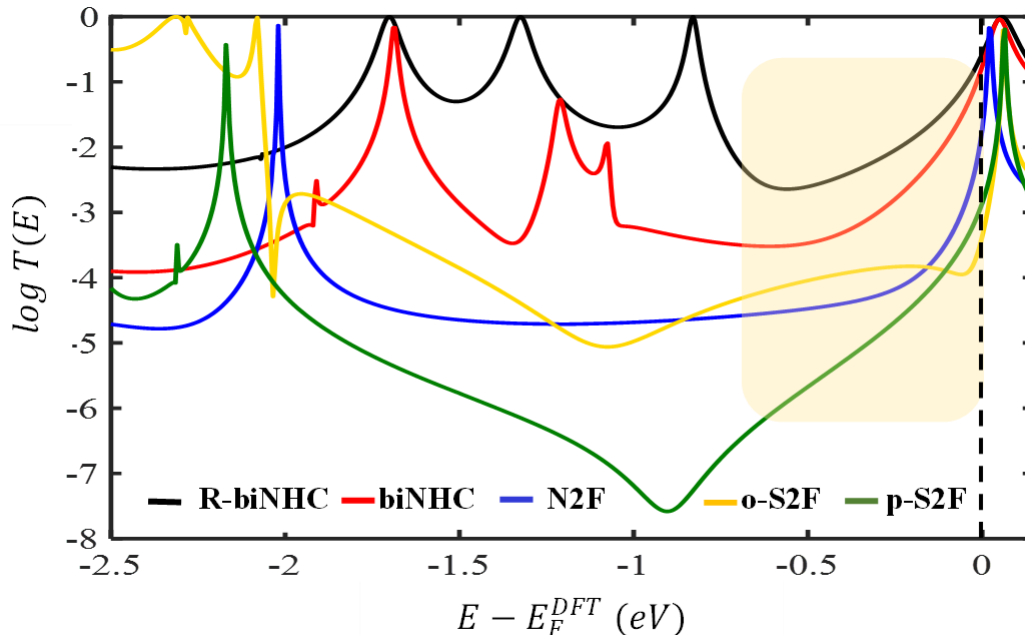


**Figure 5.4.** Transmission coefficients as a function of energy of the studied molecules in Au junctions for **Scenario B**. Zero bias transmission coefficients  $T(E)$  of as compounds **1**, **2**, **3**, **4** and **5** (**biNHC**, **R-biNHC**, **N2F**, **o-S2F** and **p-S2F**) against electron energy  $E$  in Au metallic junctions. The yellow rectangular box shows a wide range of energy within the HOMO–LUMO gap.

### Scenario C:

Figure 5.5 illustrates scenario **C**, which is corresponding to the weakest binding between the molecule and electrodes, as shown in chapter 4 (see Figures 4.11-4.13). There is 90 degrees between the two Au electrodes when they contact the molecule for all molecules studied in this scenario. For compounds **1** and **2** (**R-biNHC** and **biNHC** molecules), the contact points are the six nitrogen atoms (Au-N), while for compounds **3**, **4** and **5** (**N2F**, **o-S2F** and **p-S2F** molecules), the contact points are carbon atoms (Au-C), as shown in Table 5.1.

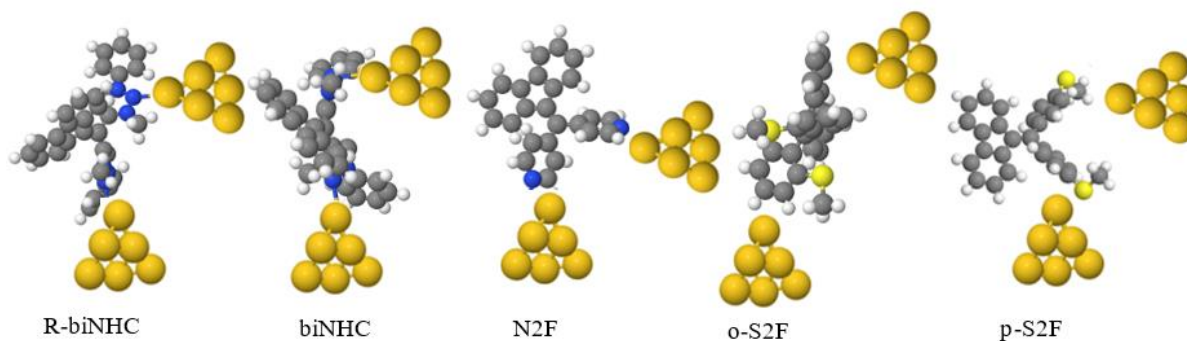


**Figure 5.5.** Schematic illustrations of the monomer molecules in Au junctions for Scenario **C**. It illustrates Au contact points to the anchor groups where is approximately 90 degrees between the two contact points and as follows for compounds **1** and **2** (**R-biNHC** and **biNHC**): Au-N, compound **3** (**N2F**): Au-C, compounds **4** and **5** (**o-S2F** and **p-S2F**):(Au-C).

Figure 5.6 illustrates the transmission coefficients  $T(E)$  as an energy of electron function for the monomer molecules in scenario **C**. The mechanism of charge transport through all these junctions of scenario **C** is a LUMO-based conduction mechanism at the DFT-predicted Fermi energy ( $E - E_F^{DFT} = 0$  eV) (black dashed line).

Hence, transmission coefficient  $T(E)$  curves calculate based on binding the energy type that shown in Tables 4.1 and 5.1. Again, at the DFT-predicted Fermi energy ( $E - E_F^{DFT} = 0$  eV), compound **1** (**R-biNHC**) possesses the highest conductance value which is roughly  $10^{-1.5}G_0$  while the conductance for compounds **2** and **4** (**biNHC** and **o-S2F**) (red and yellow), is slightly lower around  $10^{-2}G_0$ . Compounds **3** and **5** (**N2F** and **p-S2F**) (blue and green), have the lowest conductance around  $10^{-3}G_0$ .

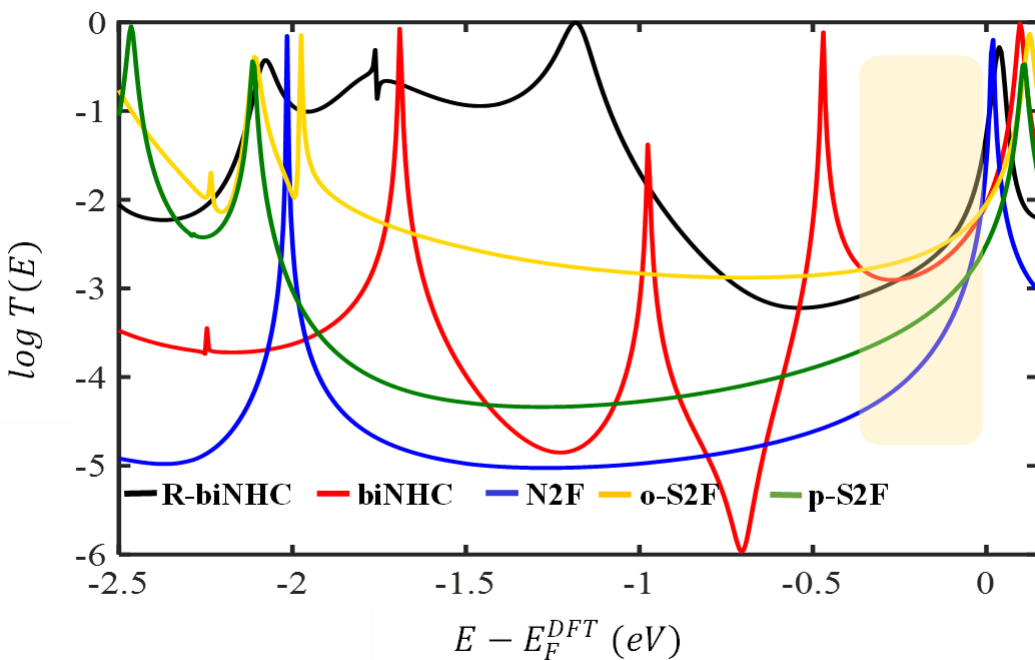


**Figure 5.6.** Transmission coefficients as a function of energy of the studied molecules in Au junctions for **Scenario C**. Zero bias transmission coefficients  $T(E)$  of compounds **1**, **2**, **3**, **4** and **5** (**R-biNHC**, **biNHC**, **N2F**, **o-S2F** and **p-S2F**) against electron energy  $E$  in Au metallic junctions. The yellow rectangular box shows that a range of energy within the HOMO–LUMO gap.

From all transmission curves in scenarios **A**, **B** and **C**, I find that scenario **A** is the energetically most favoured, because of its strong binding energy values and, therefore, may possess a high conductance. This is attributed to the most favourable positions relating to either different anchor groups or the other binding sites (i.e., Au-C or Au-five-membered ring), as shown in Tables 4.1 and 5.1. It is noteworthy that the order of the transmission coefficients for this scenario **C** does not follow those scenarios **A** and **B** and track the experimental order. Therefore, I do not consider this scenario further. The previous transmission curves  $T(E)$  calculated for the monomer molecules obtained using these two scenarios **A** and **B** for a wide range of Fermi energy window (indicated by yellow rectangular boxes in Figures 5.2 and 5.4) depends on the three strongest binding energies as shown in chapter 4 (see Figures 4.11- 4.13). Hence, my simulations predict that the conductance of the monomers follows the order of compounds **1**, **2**, **3**, **4** and **5** (**R-biNHC** > **biNHC** > **N2F** > **o-S2F** > **p-S2F**), in excellent agreement with the experimentally measured trend as we will see later.

### 5.2.3 Spin polarisation

To study the structure-property relation in these metallic-molecular junctions based on the electronic structure, spin-polarised calculations based on the density functional theory play a critical role.<sup>16</sup> Many useful approximations have been used in these calculations, such as the local density approximation (LDA), which depends locally on the spin densities, and the generalised gradient approximation (GGA), which also depends on the gradients of the spin densities. Besides the transport code Gollum, specifically designed for such spin-polarised calculations.<sup>17</sup> Therefore,

using spin-dependent density functional computing, molecules' geometric, electrical, magnetic properties are thoroughly investigated in the current research.

Since atoms often are magnetic, when an external magnetic field is supplied to an electronic system, the electron spin and the electronic orbital current are typically coupled.<sup>18</sup> In other words, spin effects are generally observed in electron-transfer processes in magnetic materials or systems containing heavy atoms that enable spin-orbit coupling. Alexandre reported a chemical route to spintronics devices in which efficiency and performance may be tuned by the appropriate choice of molecules and end groups.<sup>17</sup> Several spintronics investigations have briefed electrons' selective spin transmission through gold's self-assembled monolayers of double-stranded DNA or by sandwiching single dsDNA between two electrodes.<sup>19,20</sup> Using the Landauer-Büttiker formula and the Green's function technique, Gui-Fang discovered spin-dependent conductance and spin-polarisation. They demonstrated that dsDNA might act as a spin-filter for both spin-up and spin-down electrons. Furthermore, investigating the influences of electron-vibration interaction on the spin-selective transport in dsDNA and therefore enhancing the spin polarisation to bring a series of new spin-splitting transmission modes in the HOMO-LUMO gap.<sup>21</sup>

As a result, spin polarised transport calculations are needed in some special studied structures of this work containing metal atoms. In the following section, all the electron transmission coefficient  $T(E)$  are computed as the average spin-up and spin-down transmission coefficients.

## 5.2.4 Transport calculations of dimer molecules

As the dimer molecule compounds **6** and **7** (**2Ag-2biNHC** and **2Au-2biNHC**), which is a monomer or molecular complex formed by the joining of two identical molecules, is positively charged (cation) (i.e.,  $\text{Ag}^+$  or  $\text{Au}^+$ ), a negatively charged counterion (an ion with the opposite charge (anion) of another ion of the substance (cation.) is needed to keep the whole system neutral or maintain the electrical neutrality.<sup>22</sup> Here, this anion (trifluoromethanesulfonate) signified by ( $\text{OTf}^-$ ) or  $\text{CF}_3\text{SO}_3^-$  is employed as a counterion.<sup>23</sup> Figure.5.7 illustrates an example of a dimer molecule and a nearby counterion.

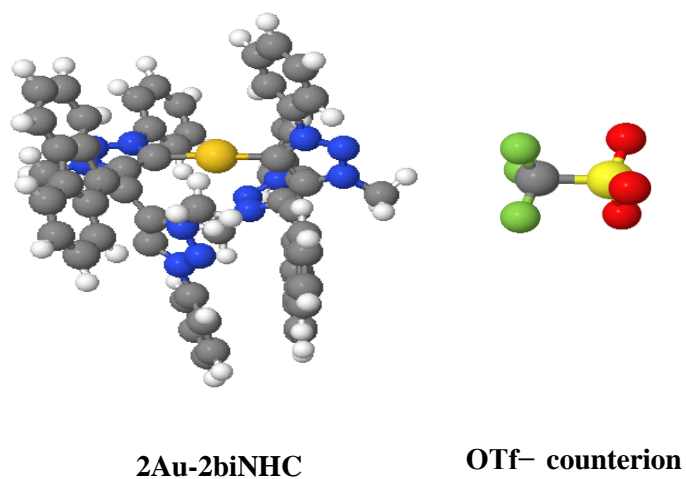


**Figure 5.7.** Examples of molecular geometries for the dimer. **Left panel:** an isolated dimer molecule compound **7** (**2Au-2biNHC**). **Right panel:** shows a counterion (i.e.,  $\text{OTf}^-$ ).

### 5.2.5 Spin-dependent transport calculations of dimer molecules

Since the dimer compounds **6** and **7** (**2Ag-2biNHC** and **2Au-2biNHC**) contain metal atoms, as shown in chapter 4 (see Figure 4.2), spin polarised transport calculations were carried out. It used the Gollum method to compute the spin-dependent transmission coefficients  $T(E)$  for electrons of energy  $E$  passing from the left gold electrode to the right electrode. In general, one expects the conductance to be dominated by resonant transport either through the HOMO or the LUMO state of the molecule. These reveal that the calculated transmission for spin-up ( $T_{up}(E)$ ) and spin-down ( $T_{down}(E)$ ) show that the LUMO resonance is split as expected due to the charge transfer from the metal atom to the rest of the molecule, which positions the resonance close to the Fermi energy ( $E - E_F^{DFT} = 0$  eV). The average spin-up and spin-down transmission coefficients as a function of energy is then given by  $\frac{T_{up}(E)+T_{down}(E)}{2}$ . Figures 5.8 and 5.9 show the average spin-polarised transmission coefficient results of the two dimers **2Au-2biNHC** and **2Ag-2biNHC**, respectively.

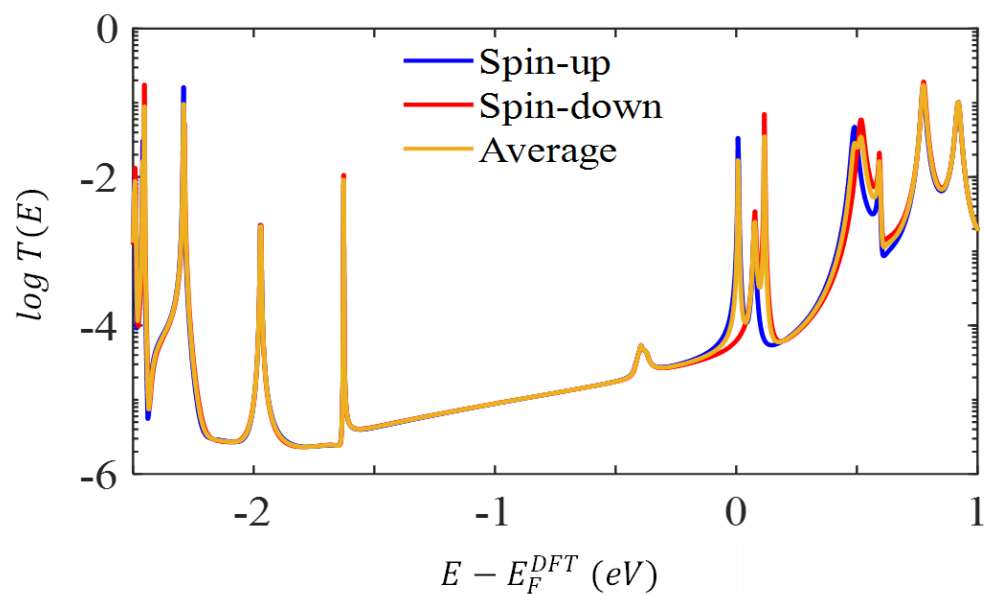


**Figure 5.8.** Spin-polarised transmission coefficients, spin-up ( $T_{up}(E)$ ), spin-down ( $T_{down}(E)$ ) and  $\frac{T_{up}(E)+T_{down}(E)}{2}$ , for the binding configuration of compound **7** (**2Au-2biNHC**) with the OTf<sup>-</sup> counterion. Three curves represent the spin-up, spin-down and the average of them: blue, red, and orange curves respectively.

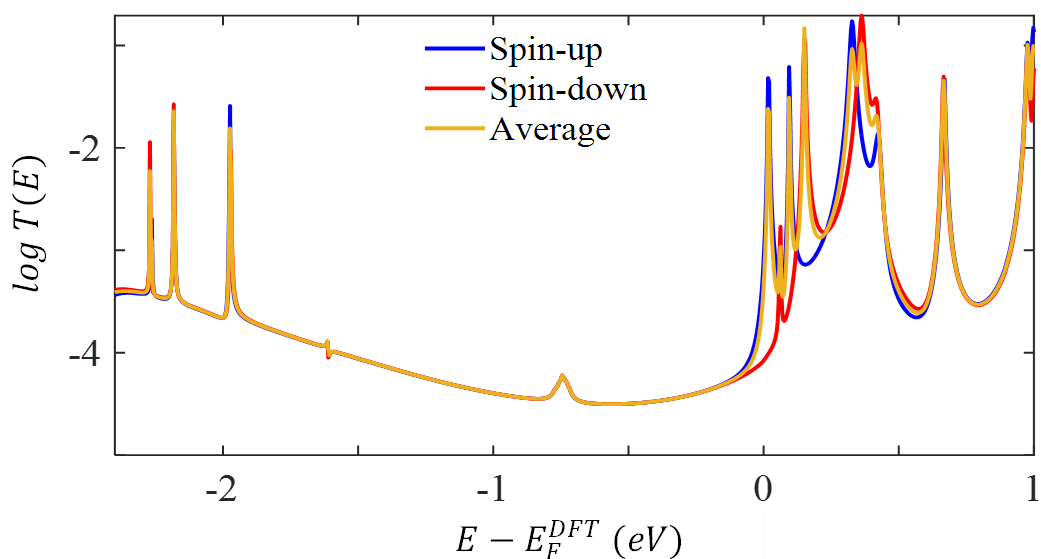


**Figure 5.9.** Spin-polarised transmission coefficients spin-up ( $T_{up}(E)$ ), spin-down ( $T_{down}(E)$ ) and  $\frac{T_{up}(E)+T_{down}(E)}{2}$ , for the binding configuration of compound **6** (**2Ag-2biNHC**) with the OTf<sup>-</sup> counterion. Three curves represent the spin-up, spin-down and the average of them: blue, red, and orange curves respectively.

### 5.2.6 Fluctuations of OTf<sup>-</sup> counterion

I examined the effect of varying the positions of OTf<sup>-</sup> counterion, by placing the OTf<sup>-</sup> counterion at 12 different positions around the dimer, as shown in Figure 5.10, and in each case computed the spin-polarised transmission coefficient  $T(E)$ . Figure 5.11 shows the average spin-polarised transmission coefficient  $T(E)$  as a function of energy for different orientations of OTf<sup>-</sup> with compound **7** (**2Au-2biNHC** dimer). Similarly, Figure 5.12 shows the average spin-polarised transmission coefficients of OTf<sup>-</sup> with compound **6** (**2Ag-2biNHC** dimer). Therefore, the average

spin-polarised transmission coefficient  $T(E)$  as a function of energy for fluctuations of OTf<sup>-</sup> counterion with compounds **6** and **7** (**2Ag-2biNHC** and **2Au-2biNHC**) are almost identical compared to those results in Figures 5.8 and 5.9.

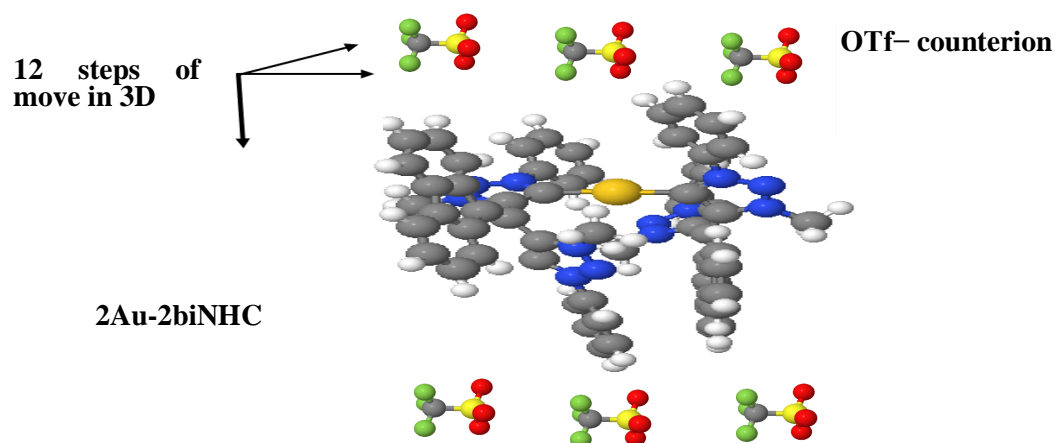


**Figure 5.10.** Sampling the OTf<sup>-</sup> counterion position around the dimer **2Au-2biNHC**. (For clarity the electrodes are not shown and only 6 positions are shown).

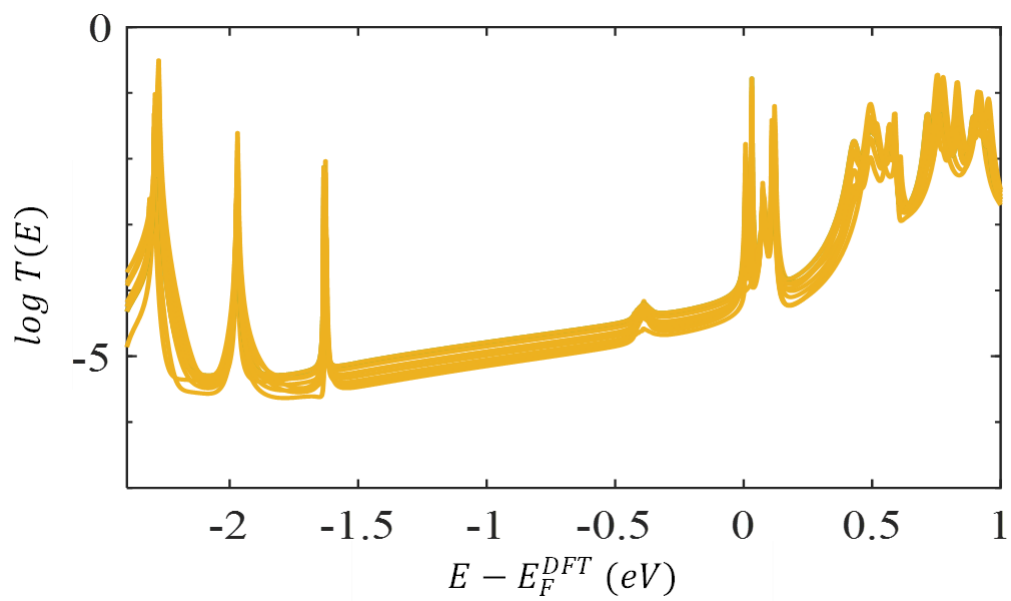


**Figure 5.11.** Orange curves show the average spin-polarised transmission coefficient  $T(E)$  as a function of energy for a selection of the 12 possible configurations of  $\text{OTf}^-$  counterion bound to compound **7** (**2Au-2biNHC** dimer).

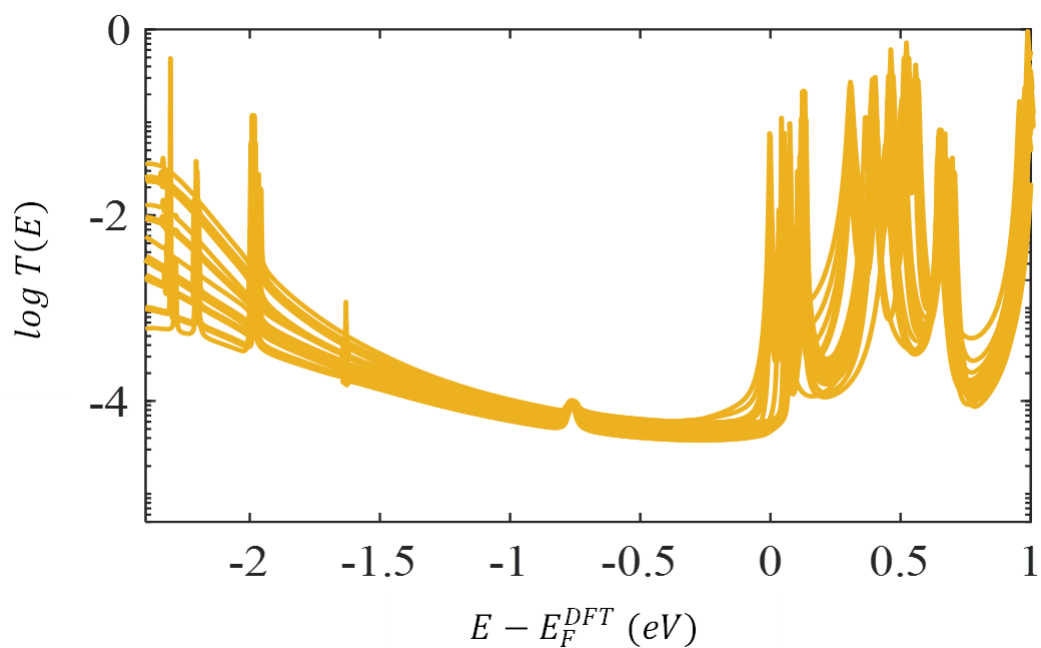


**Figure 5.12.** Orange curves show the average spin-polarised transmission coefficient  $T(E)$  as a function of energy for a selection of the 12 possible configurations of  $\text{OTf}^-$  counterion bound to compound **6** (**2Ag-2biNHC** dimer).

### 5.2.7 Comparison of transmission functions of monomers and dimers

In this section, I shall compare the average spin-polarised transmission coefficients  $T(E)$  as a function of the energy of the two dimers, compounds **6** and **7** (**2Ag-2biNHC** and **2Au-2biNHC**), with those in Figure 5.2 of the five monomers, compounds **1**, **2**, **3**, **4** and **5** (**R-biNHC**, **biNHC**, **N2F**, **o-S2F** and **p-S2F**) that shown in scenario **A**. The combined results are shown in Figure 5.13 which displays the room-temperature electrical conductance of the monomer and dimer molecules in Au junctions. This Figure exhibits a LUMO-dominated transport of the DFT-predicted Fermi

energy ( $E - E_F^{DFT} = 0$  eV). As a result, compound **1** (**R-biNHC** molecule) still has the highest conductance value compared to other monomer and dimer molecules. On the other hand, the conductance of compound **6** (dimer **2Ag-2biNHC**) is similar to that of compound **7** (dimer **2Au-2biNHC**) are around  $10^{-4.2} G_0$  and  $10^{-4.4} G_0$  at the DFT-predicted Fermi energy ( $E - E_F^{DFT} = 0$  eV) respectively. However, the conductance of monomer compound **2** (**biNHC**) is significantly higher than the dimer ones.

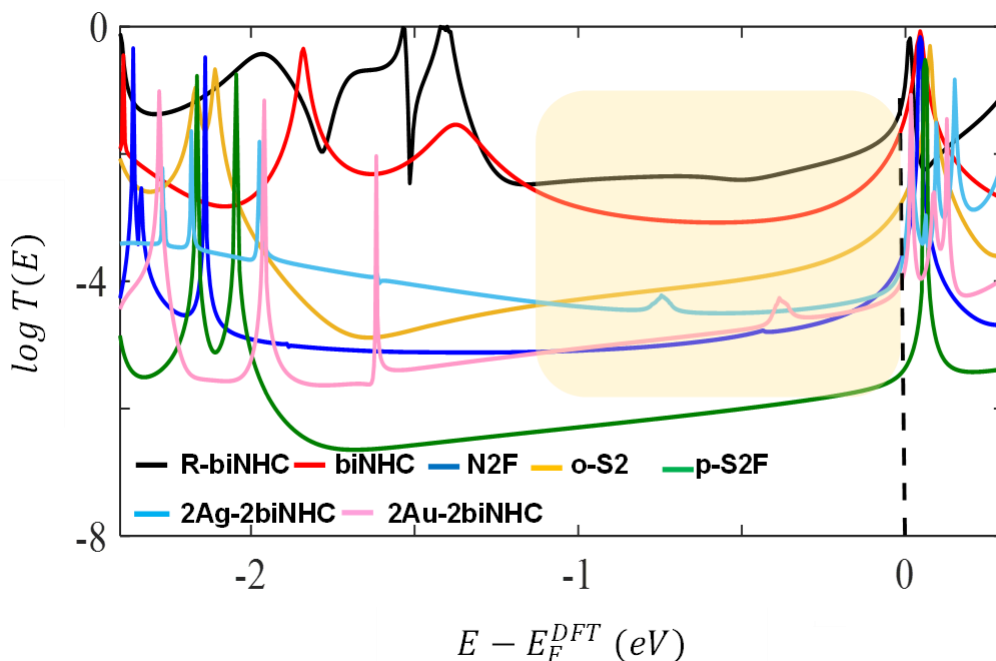


**Figure 5.13.** Transmission coefficients of the studied molecules in Au junctions. Zero bias transmission coefficients  $T(E)$  of compounds **1**, **2**, **3**, **4** and **5** (**biNHC**, **R-biNHC**, **N2F**, **o-S2F** and **p-S2F**) (as monomers), and compounds **6** and **7** (**2Ag-2biNHC** and **2Au-2biNHC**) (as dimers), against electron energy  $E$  in Au metallic junctions (scenario **A**).

### 5.3 Broadened molecular orbital of monomers and dimers

This section investigates the critical feature of the transmission curves  $T(E)$  related to the Breit-Wigner formula (BWF), which is reported as an analytical model applied to a three-level system using the tight-binding model in chapter 3 (section 3.11.1) Eq. 3.70, representing the on-resonance transmission for electrons of energy  $E$  passing from a one lead to another one via a molecule. In general, the Breit-Wigner formula could describe any individual peak of transmission  $T(E)$  curves if the energy  $E$  of the electron is close to an eigenenergy of the isolated molecule and if the spacing level  $\delta$  of the isolated molecule is larger than the width of the resonance called the broadening level ( $\Gamma = \Gamma_L + \Gamma_R$ ), due to the contact with the left and right electrodes.

Based on my calculations, the electron transport of the studied junctions is mainly LUMO-dominated. Herein, the transmission coefficient  $T(E)$  curves in scenario **A** are satisfied the Breit-Wigner resonances condition, which means the broadening level  $\Gamma = \Gamma_L + \Gamma_R$  on resonances (the width of the peak), is smaller than the energy spacing level (differences between the eigenenergy which shifted slightly by the real part of the self-energy due to the contacts).

Figure 5.14 illustrates an example of broadened molecular orbital for a monomer molecule such as compound **3** (**N2F**) against the electron energy  $E$ . Hence, if the case here is not symmetric ( $\Gamma_L \neq \Gamma_R$ ), then  $T(E)$  will possess a peak (resonances) located at energies close to the eigenenergy of the isolated molecule. Then the maximum value of the transmission coefficient is less than the unity. The half-maximum width of the peak ( $\Gamma_L + \Gamma_R$ ) that the molecular level obtains in virtue of the coupling to the electrodes can be used as a measure of the strength of the electrodes-molecule coupling. Since the left and right electrodes (source and drain) are gold, the level broadening ( $\Gamma = \Gamma_L + \Gamma_R$ ) is approximately independent of energy. This is a good approximation for the case of

gold, whose relatively local density of states is in the vicinity of the Fermi energy<sup>24,25</sup> as illustrated in Figure 5.14.

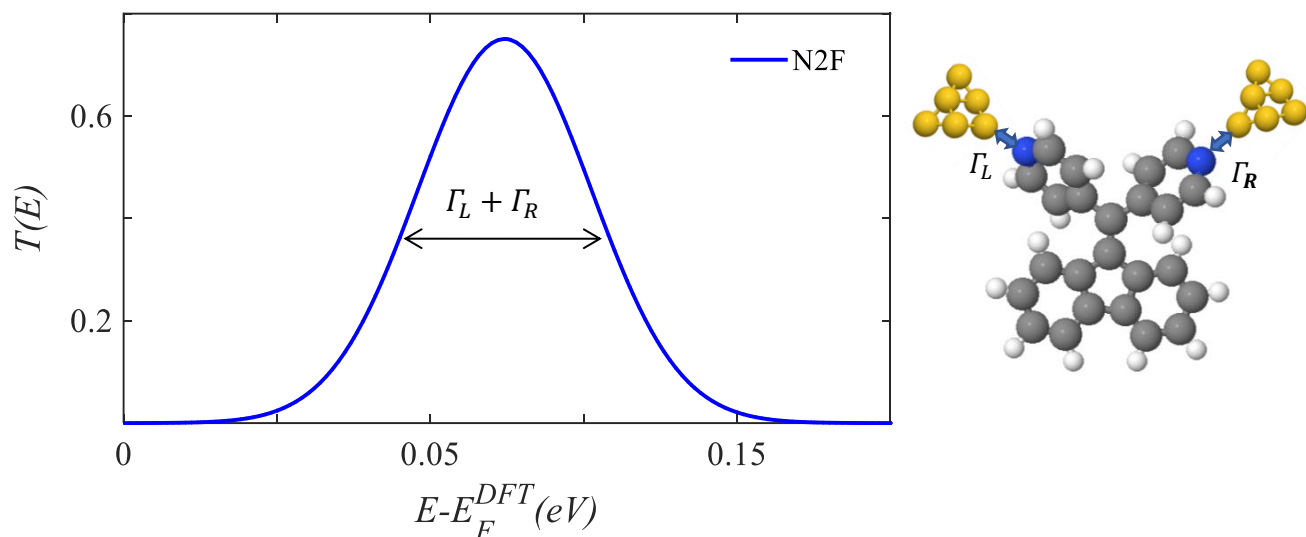


**Figure 5.14.** Example of broadened molecular orbital  $\Gamma = \Gamma_L + \Gamma_R$  value of compound **3** (N2F) against electron energy  $E$  in Au metallic junctions with respect to the DFT-predicted Fermi energy ( $E - E_F^{DFT} = 0$  eV).

Herein, I calculate the broadened molecular orbital values  $\Gamma = \Gamma_L + \Gamma_R$  for compounds **1**, **2**, **3**, **4** and **5** (**biNHC**, **R-biNHC**, **N2F**, **o-S2F** and **p-S2F**) (as monomers), and compounds **6** and **7** (**2Ag-2biNHC** and **2Au-2biNHC**) (as dimers), as shown in Figures 5.15 and 5.16, respectively. The most significant feature to observe is that, of the case depicted in Figure 5.14, transport is dominated by a single level, particularly the one closest to the gold Fermi level. Furthermore, in all those cases the, the transmission resonances near the DFT-predicted Fermi energy ( $E - E_F^{DFT} = 0$  eV) could be fitted using the Breit-Wigner formula Eq. 3.70 described in chapter 3. For symmetric

junctions in a specific energy window, which justifies the usage of the single-level model (a simple theoretical model, that assumes transport is phase coherent.<sup>24</sup> The broadened molecular orbital values  $\Gamma = \Gamma_L + \Gamma_R$  of the monomer and dimer were calculated and fitted as shown in Figures 5.15 and 5.16. In addition, Table 5.3 summarises the detail of this study, and it is worth mentioning that the theoretical broadened molecular orbitals tended to be slightly smaller than the experimental ones, as we will see in the comparison section.

### 5.3.1 Broadened molecular orbital of monomers

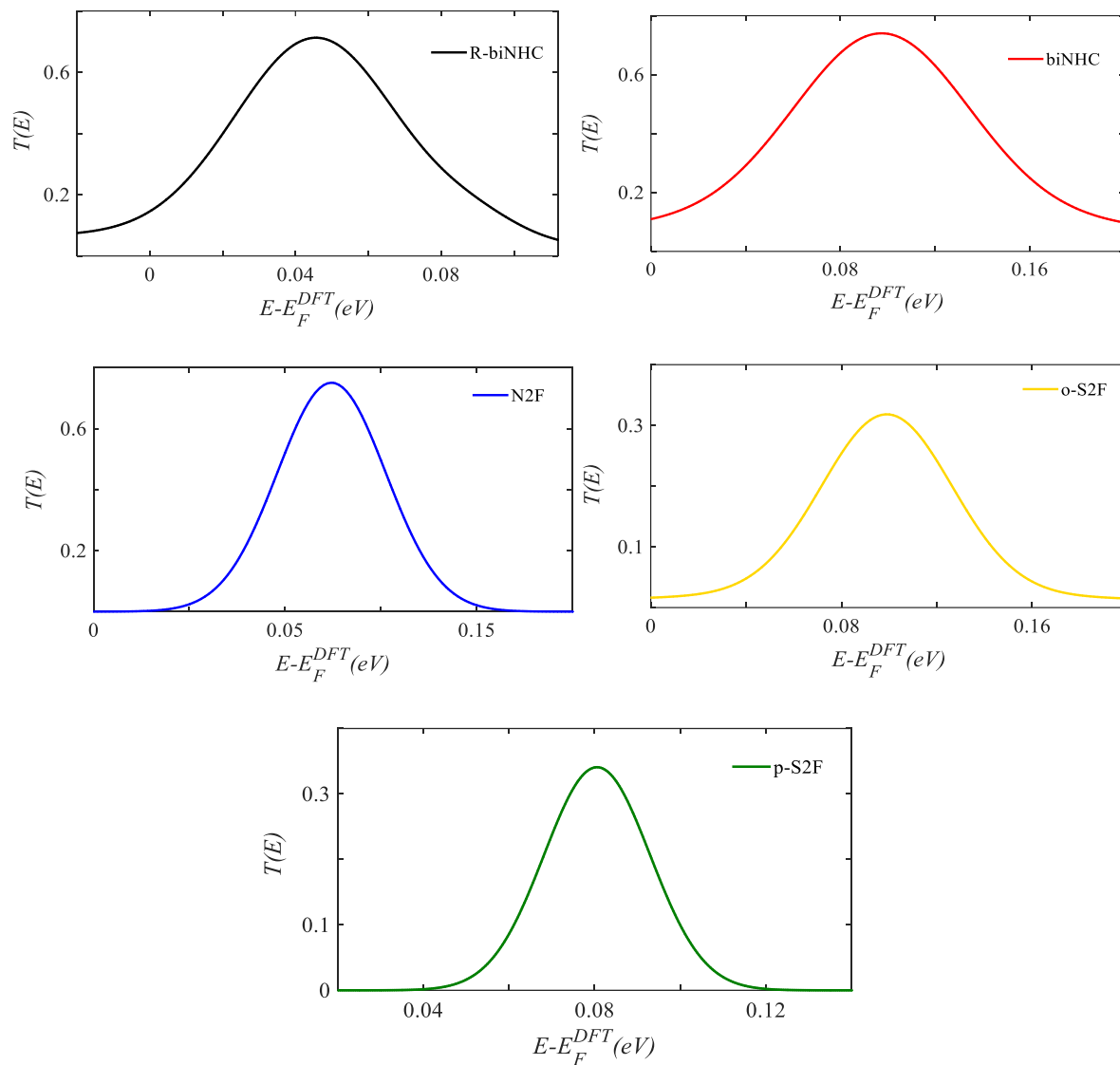


**Figure 5.15.** Broadened molecular orbital  $\Gamma = \Gamma_L + \Gamma_R$  values of compounds **1**, **2**, **3**, **4** and **5** (**R-biNHC**, **biNHC**, **N2F**, **o-S2F** and **p-S2F**) against electron energy  $E$  in Au metallic junctions (scenario **A**).

### 5.3.2 Broadened molecular orbital of dimers

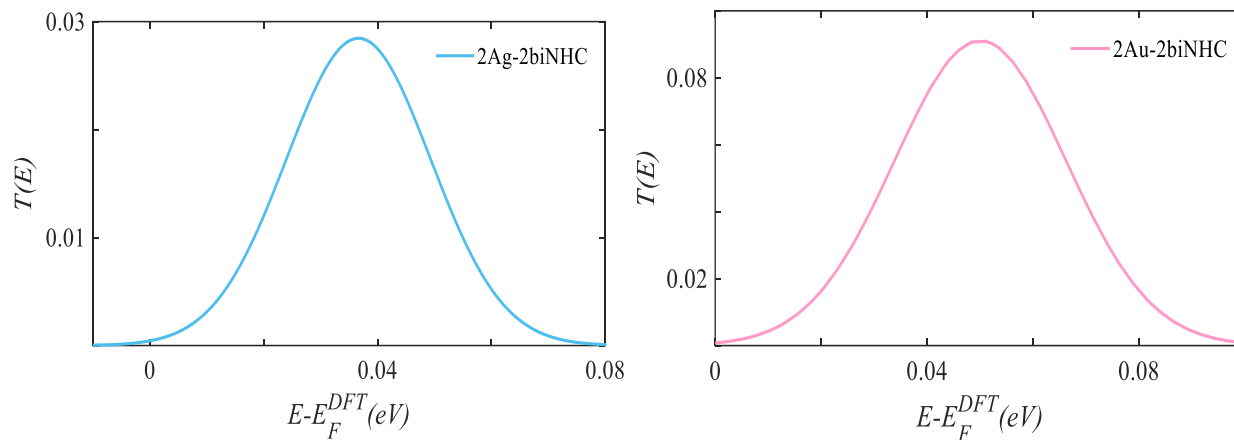


**Figure 5.16.** Broadened molecular orbital  $\Gamma = \Gamma_L + \Gamma_R$  values of compounds **6** and **7** (**2Ag-2biNHC** and **2Au-2biNHC**) against electron energy  $E$  in Au metallic junctions.

**Table 5.2.** Summarises the theoretical results for broadened molecular orbital values of coupling strength  $\Gamma = \Gamma_L + \Gamma_R$  for the monomer (scenario **A** ) and dimer junctions that shown in Figures 5.15 and 5.16.

<b>Compound</b>	<b><math>\Gamma</math> (eV)</b>
R-biNHC	0.013
biNHC	0.100
N2F	0.082
o-S2F	0.073
p-S2F	0.024
2Ag-2biNHC	0.014
2Au-2biNHC	0.010

This Table 5.2 summarises the theoretical results obtained the values of the electronic couplings between the molecule and the source and the drain electrodes  $\Gamma_L$  and  $\Gamma_R$  for the monomer and dimer junctions as shown in Figures 5.15 and 5.16.

## 5.4 Theory versus experiment

This chapter compares the theory and experiment of some electronic properties, including the broadened molecular orbitals and conductance  $G$  features of STM formed from NHC complexes-based molecules with different anchor groups.

The calculated room-temperature electrical conductance  $G$  (in units of quantum point conductance  $G_0 = \frac{2e^2}{h} = 77 \mu\text{ Siemens}$ ), corresponding to the magnitude of the transmission coefficients for the NHC-anchored molecular junctions series are shown in Figure 5.17 below. All results for conductance are obtained from the transmission curves evaluated at the DFT predicted Fermi energy, ( $E - E_F^{DFT} = 0\text{ eV}$ ). The DFT-predicted Fermi energy at zero sits close to the LUMO resonance in all monomer and dimer of NHC-anchored molecular junctions and therefore leads to high conductance values for the two scenarios **A** and **B** as in Figures 5.2 and 5.4 and that depends on the strongest binding energies as a result from 1-D and 3-D scan simulations as shown in chapter 4 (see Figures 4.11-4.13). As expected from experimental results, the conductance, of compounds **1** and **2** (**R-biNHC** and **biNHC**) are significantly higher than that of molecules with 2-pyridyls compound **3** (**N2F**) or 2-methylmercaptophenyls compound **4** (**o-S2F**) as anchoring groups. The conductance of 2-methylmercaptophenyls **5** (**p-S2F**) anchored molecules was even too low to be measured.<sup>26,27</sup> The compound **2** (**biNHC**) possessed a conductance three times higher than that of compound **4** (**o-S2F**). Experimental results also demonstrate that the conductance value of compounds **6** and **7** (**2Ag-2biNHC** and **2Au-2biNHC**) are  $10^{-3.82} G_0$  and  $10^{-4.24} G_0$  respectively, as shown in Figure 5.17.

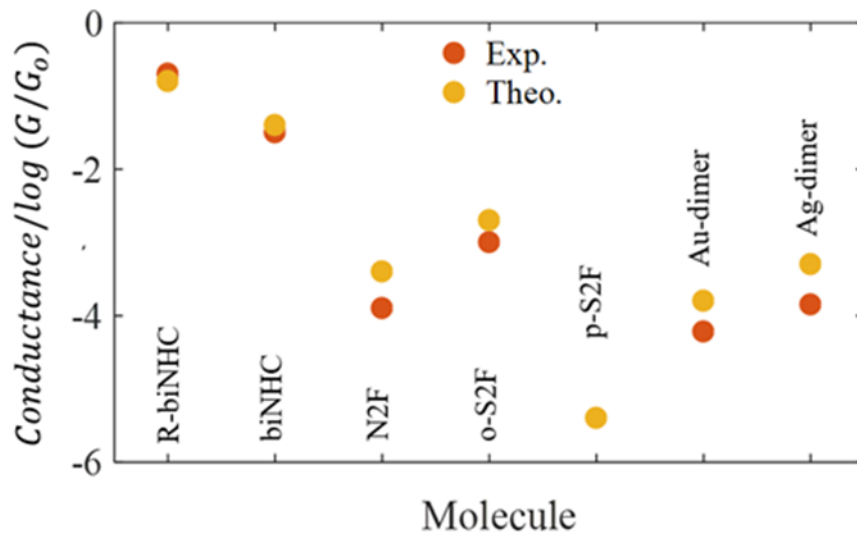


**Figure 5.17.** Comparison between experimental and theoretical conductance of the studied molecules: compounds **1**, **2**, **3**, **4** and **5** (**R-biNHC**, **biNHC**, **N2F**, **o-S2F** and **p-S2F**) (as monomers), and compounds **6** and **7** (**2Ag-2biNHC** and **2Au-2biNHC**) (as dimers) obtained at the DFT-predicted Fermi level ( $E - E_F^{DFT} = 0$  eV). Note: (The conductance of compound **5** (**p-S2F**) was undetectable experimentally).

Furthermore, The other property related to the broadened molecular orbitals values  $\Gamma = \Gamma_L + \Gamma_R$  of three monomer compounds **2**, **3** and **4** (**biNHC**, **N2F** and **o-S2F**). Experimentally broadened molecular orbitals indicate slight differences to the theoretical broadened molecular orbitals values as reported in Table 5.3. These results prove that the introduction of NHCs as anchor groups is a promising solution for the construction of highly conductive molecular junctions.

**Table 5.3.** A comparison Table of theoretical and experimental broadened molecular orbital  $\Gamma_{\text{Theo.}}$  and  $\Gamma_{\text{Exp.}}$  of monomer molecules. Note: (The broadened molecular orbital  $\Gamma$  of the compounds **2**, **3** and **4** (**biNHC**, **N2F** and **o-S2F**) was only measured experimentally).

Compound	$\Gamma_{\text{Theo.}}$ (eV)	$\Gamma_{\text{Exp.}}$ (eV)
biNHC	0.100	0.184±0.100
N2F	0.082	0.084±0.055
o-S2F	0.073	0.085±0.048

## 5.5 Conclusion

In this chapter, using a combination of experimental STM-based transport measurements and DFT-based transport calculations, I have discussed the transport properties of the NHC-anchored single-molecule junctions. The 1-D and 3-D binding-energy scan simulations in chapter 4 exhibited three binding scenarios, **A**, **B** and **C**, for forming different molecular junctions. Thus, for all transmission curves in scenarios **A**, **B** and **C**, I find that scenarios **A** is the most energetically favourable due to the stronger binding energy values. Due to these high binding energies, this scenario also exhibits a high conductance. This is attributed to the most-favourable position corresponding to either different anchor groups or binding sites (i.e., Au-C). The theoretical transport calculations proved the mechanism of charge transport through NHCs molecules is most likely a LUMO-based

conduction mechanism. In addition, **A** and **B** scenarios predict that the conductance of the monomers follows the order of compounds **1, 2, 3, 4** and **5** (**R-biNHC** > **biNHC** > **N2F** > **o-S2F** > **p-S2F**), which is in an excellent agreement with the experimentally measured trend.

On another side of this study, with the dimer molecules compounds **6** and **7** (**2Au-2biNHC** and **2Ag-2biNHC**), since they include Au and Ag metal atoms, spin polarisation simulations were carried out to determine their spin-polarised transmission coefficients. For the positively charged compounds **6** and **7** (dimers **2Ag-2biNHC** and **2Au-2biNHC**), OTf<sup>-</sup> was employed as a counterion to achieve overall charge neutrality and examined varying its different positions around the dimer and then the resulting in variation in the transmission curves. Furthermore, a combination of experiment investigation and DFT calculations revealed the theoretical broadened molecular orbitals of monomers and dimers tended to be slightly smaller than the experimental through NHC-anchored molecular junctions.

## 5.6 Bibliography

1. Soler, J. M., Artacho, E., Gale, J. D., García, A., Junquera, J., Ordejón, P., and Sánchez-Portal, D. (2002). The SIESTA method for ab initio order-N materials simulation. *Journal of Physics: Condensed Matter*, 14(11), 2745.
2. Ferrer, J., Lambert, C. J., García-Suárez, V. M., Manrique, D. Z., Visontai, D., Oroszlany, L., Rodríguez-Ferradás, R., Grace, I., Bailey, S. W. D., Gillemot, K., Sadeghi, H., and Algharagholy, L. A. (2014). GOLLUM: A next-generation simulation tool for electron, thermal and spin transport. *New Journal of Physics*, 16(9), 093029.
3. Datta, S. (1995). *Electronic Transport in Mesoscopic Systems* (1st ed.). Cambridge University Press.
4. Wang, X., Bennett, T. L. R., Ismael, A., Wilkinson, L. A., Hamill, J., White, A. J. P., Grace, I. M., Kolosov, O. V., Albrecht, T., Robinson, B. J., Long, N. J., Cohen, L. F., and Lambert, C. J. (2020). Scale-Up of Room-Temperature Constructive Quantum Interference from Single Molecules to Self-Assembled Molecular-Electronic Films. *Journal of the American Chemical Society*, 142(19), 8555–8560.
5. Ismael, A., Wang, X., Bennett, T. L. R., Wilkinson, L. A., Robinson, B. J., Long, N. J., Cohen, L. F., and Lambert, C. J. (2020). Tuning the thermoelectrical properties of anthracene-based self-assembled monolayers. *Chemical Science*, 11(26), 6836–6841.
6. Wang, X., Ismael, A., Almutlg, A., Alshammari, M., Al-Jobory, A., Alshehab, A., Bennett, T. L. R., Wilkinson, L. A., Cohen, L. F., Long, N. J., Robinson, B. J., and Lambert, C. (2021). Optimised power harvesting by controlling the pressure applied to molecular junctions. *Chemical Science*, 12(14), 5230–5235.
7. Naghibi, S., Ismael, A. K., Vezzoli, A., Al-Khaykane, M. K., Zheng, X., Grace, I. M., ... and Nichols, R. J. (2019). Synthetic control of quantum interference by regulating charge on a single atom in heteroaromatic molecular junctions. *The journal of physical chemistry letters*, 10(20), 6419-6424.
8. González, M. T., Ismael, A. K., García-Iglesias, M., Leary, E., Rubio-Bollinger, G., Grace, I., González-Rodríguez, D., Torres, T., Lambert, C. J., and Agraït, N. (2021). Interference Controls Conductance in Phthalocyanine Molecular Junctions. *The Journal of Physical Chemistry C*, 125(27), 15035–15043.
9. Doud, E. A., Inkpen, M. S., Lovat, G., Montes, E., Paley, D. W., Steigerwald, M. L., Vázquez, H., Venkataraman, L., and Roy, X. (2018). In Situ Formation of N-Heterocyclic Carbene-Bound Single-Molecule Junctions. *Journal of the American Chemical Society*, 140(28), 8944–8949.
10. Markin, A., Ismael, A. K., Davidson, R. J., Milan, D. C., Nichols, R. J., Higgins, S. J., ... and Beeby, A. (2020). Conductance Behavior of Tetraphenyl-Aza-BODIPYs. *The Journal of Physical Chemistry C*, 124(12), 6479-6485.

11. Gantenbein, M., Wang, L., Al-jobory, A. A., Ismael, A. K., Lambert, C. J., Hong, W., Bryce, M. R., and Link to external site, this link will open in a new window. (2017). Quantum interference and heteroaromaticity of para- and meta-linked bridged biphenyl units in single molecular conductance measurements. *Scientific Reports (Nature Publisher Group)*, 7, 1–9.
12. Ismael, A. K., and Lambert, C. J. (2019). Single-molecule conductance oscillations in alkane rings. *Journal of Materials Chemistry C*, 7(22), 6578-6581.
13. Naher, M., Milan, D. C., Al-Owaedi, O. A., Planje, I. J., Bock, S., Hurtado-Gallego, J., Bastante, P., Abd Dawood, Z. M., Rincón-García, L., Rubio-Bollinger, G., Higgins, S. J., Agraït, N., Lambert, C. J., Nichols, R. J., and Low, P. J. (2021). Molecular Structure–(Thermo)electric Property Relationships in Single-Molecule Junctions and Comparisons with Single- and Multiple-Parameter Models. *Journal of the American Chemical Society*, 143(10), 3817–3829.
14. Kim, Y., Pietsch, T., Erbe, A., Belzig, W., and Scheer, E. (2011). Benzenedithiol: A Broad-Range Single-Channel Molecular Conductor. *Nano Letters*, 11(9), 3734–3738.
15. Su, T. A., Neupane, M., Steigerwald, M. L., Venkataraman, L., and Nuckolls, C. (2016). Chemical principles of single-molecule electronics. *Nature Reviews Materials*, 1(3), 16002.
16. Mokrousov, Y., Bihlmayer, G., and Blügel, S. (2005). Full-potential linearized augmented plane-wave method for one-dimensional systems: Gold nanowire and iron monowires in a gold tube. *Physical Review B*, 72(4), 045402.
17. Rocha, A. R., García-suárez, V. M., Bailey, S. W., Lambert, C. J., Ferrer, J., and Sanvito, S. (2005). Towards molecular spintronics. *Nature Materials*, 4(4), 335–339.
18. Zeller, R. (2006). Spin-polarized dft calculations and magnetism. *Computational Nanoscience: Do It Yourself*, 31, 419-445..
19. Guo, A.-M., and Sun, Q. (2012). Enhanced spin-polarized transport through DNA double helix by gate voltage. *Physical Review B*, 86(3), 035424.
20. Göhler, B., Hamelbeck, V., Markus, T. Z., Kettner, M., Hanne, G. F., Vager, Z., Naaman, R., and Zacharias, H. (2011). Spin Selectivity in Electron Transmission Through Self-Assembled Monolayers of Double-Stranded DNA. *Science*, 331(6019), 894–897.
21. Du, G.-F., Fu, H.-H., and Wu, R. (2020). Vibration-enhanced spin-selective transport of electrons in the DNA double helix. *Physical Review B*, 102(3), 035431.
22. Bharti, R., Verma, M., Thakur, A., and Sharma, R. (2022). N-Heterocyclic Carbenes (NHCs): An Introduction. *Carbene*, 43.
23. Ciancaleoni, G., Belpassi, L., Zuccaccia, D., Tarantelli, F., and Belanzoni, P. (2015). Counterion Effect in the Reaction Mechanism of NHC Gold(I)-Catalyzed Alkoxylation of Alkynes: Computational Insight into Experiment. *ACS Catalysis*, 5(2), 803–814.

24. Zotti, L. A., Kirchner, T., Cuevas, J.-C., Pauly, F., Huhn, T., Scheer, E., and Erbe, A. (2010). Revealing the Role of Anchoring Groups in the Electrical Conduction Through Single-Molecule Junctions. *Small*, 6(14), 1529–1535.
25. Famili, M. (2018). Theory of molecular scale thermoelectricity. Lancaster University (United Kingdom).
26. Park, Y. S., Widawsky, J. R., Kamenetska, M., Steigerwald, M. L., Hybertsen, M. S., Nuckolls, C., and Venkataraman, L. (2009). Frustrated Rotations in Single-Molecule Junctions. *Journal of the American Chemical Society*, 131(31), 10820–10821.
27. Fu, Y., Chen, S., Kuzume, A., Rudnev, A., Huang, C., Kaliginedi, V., Baghernejad, M., Hong, W., Wandlowski, T., Decurtins, S., and Liu, S.-X. (2015). Exploitation of desilylation chemistry in tailor-made functionalization on diverse surfaces. *Nature Communications*, 6(1), 6403.

## Chapter 6

### Conclusions and Future Work

#### 6.1 Conclusions

This thesis focused on electron transport theory in molecular scale quantum devices and experimental modelling to study the electronic structure of various molecules as a new robust molecular design strategy for future applications, aiming to improve the efficiency of thermoelectric devices. To obtain an insight into the different physical properties of the studied molecules as building blocks to perform other device functions when connected to metal electrodes and build a nanoscale circuit, I investigated their electronic structures and electrical properties by using self-consistent density functional theory (DFT) as implemented in the SIESTA code, and Gollum's implementation of the Green's function method as discussed in Chapters 2 and 3 respectively.

In the fourth chapter, I studied several symmetric molecules to demonstrate a general principle for molecular-scale quantum transport, which opens up new material design and discovery routes. Various NHC complexes of double NHC-anchored single-molecule junctions were developed and produced. A combination of the density-functional theory method and experimental measurements was used to model the transport properties of the seven molecular junctions. I investigated the charge transport properties of the NHC-anchored molecular junctions starting with the electronic structure properties involving the wave function plots and the binding geometry. The monomer

compounds **1**, **2**, **3**, **4**, and **5** (**R-biNHC**, **biNHC**, **N2F**, **o-S2F**, and **p-S2F**) have multiple potential binding sites; accordingly, the procedure of determining them was divided into two steps. First, I used a gold tip to scan the entire molecule backbone in 3-D to allocate the strongest-binding contact spots (3-D binding energy simulations). After determining the most energetically favourable site for each molecule, the second stage of the binding-energy simulations is to determine the optimum separation distance between the electrodes and the various anchor groups and their binding energy value (1-D binding energy simulations).

In the fifth chapter, three scenarios, **A**, **B** and **C**, were suggested based on the most energetically favourable configurations (gold-molecule contact). Comparing theory against experiment, the theoretical suggested scenarios **A** and **B** proved to be in excellent agreement with the experimental measurements. For the positively charged dimers **2Au-2biNHC** and **2Ag-2biNHC**,  $\text{OTf}^-$  was employed as a counterion to achieve overall charge neutrality. Since they contain Au and Ag metal atoms, spin polarisation simulations were carried out to determine their spin-polarised transmission coefficients. Since the location of the  $\text{OTf}^-$  counterion is unknown, I examined the effect of varying its positions by placing the counterion at different positions around the dimer. Furthermore, the experimental and theoretical broadened molecular orbitals  $\Gamma$  showed a slight difference between the theory and experiment.

## 6.2 Future work

This thesis used theoretical methods and experimental measurements to predict the electrical properties of NHC-anchored molecules attached to gold leads. One may consider expanding these results in various directions for future work. For example, it is interesting to develop this research into other transport properties, such as the thermoelectrical properties and the stability of these configurations, such as the Seebeck coefficient or thermopower <sup>1-3</sup> (which is related to the slope of the transmission coefficient curve), for which more research into nanoscale and molecular-scale phonon transport is required.<sup>4,5</sup> Nevertheless, various strategies are needed to suppress the phonon transport part to reach the ultimate goal, high thermoelectric performance materials. This aim could be achieved by including a new design for a different types of electrodes, molecules, and surfaces to enhance the electron transport contribution in single-molecule junctions. Another interesting point is to explore the theoretical simulations when the gold electrodes are changed by other metals or different electrode materials for molecular electronics, such as superconducting electrodes at low temperatures <sup>6</sup>, involving platinum, palladium <sup>7,8</sup> and iron <sup>9</sup> or combinations of electrode materials.<sup>10</sup> Graphene possesses unique properties, that makes it a promising electrode material for molecular electronics in the future.<sup>11,12</sup> In the case of using graphene as an electrode, it is pivotal to design new anchor groups for attaching to graphene <sup>13</sup> that preserve coherent electron transport across the molecule-graphene interface.

### 6.3 Bibliography

1. Malen, J. A., Doak, P., Baheti, K., Tilley, T. D., Segalman, R. A., and Majumdar, A. (2009). Identifying the Length Dependence of Orbital Alignment and Contact Coupling in Molecular Heterojunctions. *Nano Letters*, 9(3), 1164–1169.
2. Tan, A., Balachandran, J., Sadat, S., Gavini, V., Dunietz, B. D., Jang, S.-Y., and Reddy, P. (2011). Effect of Length and Contact Chemistry on the Electronic Structure and Thermoelectric Properties of Molecular Junctions. *Journal of the American Chemical Society*, 133(23), 8838–8841.
3. Balachandran, J., Reddy, P., Dunietz, B. D., and Gavini, V. (2012). End-Group-Induced Charge Transfer in Molecular Junctions: Effect on Electronic-Structure and Thermopower. *The Journal of Physical Chemistry Letters*, 3(15), 1962–1967.
4. Fagas, G., Kozorezov, A. G., Lambert, C. J., Wigmore, J. K., Peacock, A., Poelaert, A., and den Hartog, R. (1999). Lattice dynamics of a disordered solid-solid interface. *Physical Review B*, 60(9), 6459–6464.
5. Kambili, A., Fagas, G., Fal’ko, V. I., and Lambert, C. J. (1999). Phonon-mediated thermal conductance of mesoscopic wires with rough edges. *Physical Review B*, 60(23), 15593–15596.
6. Hui, V. C., and Lambert, C. J. (1993). Andreev Scattering, Universal Conductance Fluctuations and Phase Periodic Transport. *Europhysics Letters (EPL)*, 23(3), 203–209.
7. Garcia-Suarez, V. M., Rocha, A. R., Bailey, S. W., Lambert, C. J., Sanvito, S., and Ferrer, J. (2005). Single channel conductance of H<sub>2</sub> molecules attached to platinum or palladium electrodes. *Physical Review B*, 72(4), 045437.
8. Smit, R. H. M., Noat, Y., Untiedt, C., Lang, N. D., van Hemert, M., and van Ruitenbeek, J. M. (2002). Measurement of the conductance of a hydrogen molecule. *Nature*, 419(6910), 906–909.
9. García-Suárez, V. M., Newman, C. M., Lambert, C. J., Pruneda, J. M., and Ferrer, J. (2004). Optimized basis sets for the collinear and non-collinear phases of iron. *Journal of Physics: Condensed Matter*, 16(30), 5453–5459.
10. Zólyomi, V., Ruzsnyák, Á., Kürti, J., and Lambert, C. J. (2010). First Principles Study of the Binding of 4d and 5d Transition Metals to Graphene. *The Journal of Physical Chemistry C*, 114(43), 18548–18552.
11. Lu, Y., Merchant, C. A., Drndić, M., and Johnson, A. T. C. (2011). In Situ Electronic Characterization of Graphene Nanoconstrictions Fabricated in a Transmission Electron Microscope. *Nano Letters*, 11(12), 5184–5188.

12. Barreiro, A., Börrnert, F., Rümmeli, M. H., Büchner, B., and Vandersypen, L. M. K. (2012). Graphene at High Bias: Cracking, Layer by Layer Sublimation, and Fusing. *Nano Letters*, 12(4), 1873–1878.
13. Bailey, S., Visontai, D., Lambert, C. J., Bryce, M. R., Frampton, H., and Chappell, D. (2014). A study of planar anchor groups for graphene-based single-molecule electronics. *The Journal of Chemical Physics*, 140(5), 054708.